Electronic structure and magnetic phase transition of hexagonal FeSe thin films studied by photoemission spectroscopy

S. Y. Tan,[1] C. H. P. Wen,[2] M. Xia,[2] J. Jiang,[2] Q. Song,[2] B. P. Xie,[2] X. C. Lai,[1] and D. L. Feng[2,*]

[1]*Science and Technology on Surface Physics and Chemistry Laboratory, Mianyang 621908, China*

[2]*Physics Department, Applied Surface Physics State Key Laboratory, and Advanced Materials Laboratory, Fudan University, Shanghai 200433, China*

(Received 4 July 2017; published 16 October 2017)

Hexagonal FeSe thin films were grown on $SrTiO_3$ substrates and the temperature and thickness dependence of their electronic structures were studied. The hexagonal FeSe is found to be metallic, with a Fermi surface consisting of six elliptical electron pockets. With decreased temperature, parts of the bands shift downward to high binding energy while some bands shift upward to E_F. The shifts of these bands begin around 300 K and saturate at low temperature, indicating a magnetic phase-transition temperature of about 300 K. With increased film thickness, the Fermi surface topology and band structure show no obvious change. Our paper reports the electronic structure of hexagonal FeSe, and shows that the possible magnetic transition is driven by large-scale electronic structure reconstruction.

DOI: 10.1103/PhysRevB.96.155124

I. INTRODUCTION

FeSe has the simplest chemical and crystal structure among all the Fe-based superconductors. The bulk FeSe superconductor has a superconducting transition temperature (Tc) of ~8 K and it can be dramatically enhanced to 37 K at high pressure [1,2]. Moreover, the discovery of high-temperature superconductivity in single unit-cell (UC) FeSe film grown on $SrTiO_3$ (STO) substrate has attracted extensive attention recently [3–9]. Whether for bulk or film materials, the superconductivity has been found to be extremely sensitive to stoichiometry in $Fe_{1+x}Se$. A superconducting β phase with tetragonal structure and a nonsuperconducting α phase with hexagonal structure are often found during sample growth with bulk or thin-film methods [10–12], which is strongly depending on the Fe/Se ratio and growth temperature. The superconducting phase of tetragonal FeSe has been studied extensively, but little is known about the hexagonal phase, especially its electronic structure.

Hexagonal structured FeSe (referred to as hexagonal FeSe hereafter) has been found to be magnetic [13,14] and received much attention for its potential application ranging from high-density data storage media [15,16], to spintronic devices [17], to anode material for lithium storage [18]. The magnetic and crystallographic properties of hexagonal FeSe strongly depend on the fabrication parameters, crystal structures, and chemical compositions. It is found, within the local-density approximation plus dynamical mean-field theory, that hexagonal FeSe resembles an orbital-selective insulating state [19]. However, hexagonal FeSe usually shows low resistivity in electric measurements with high carrier concentration just like metal [20]. Whether hexagonal FeSe has a metal or a semiconductor nature and the origin of its magnetism are still undetermined.

In this paper, we report an angle-resolved photoemission spectroscopy (ARPES) investigation of the low-energy electronic states of FeSe thin films grown on STO substrates. The hexagonal FeSe is found to be metallic, with a Fermi surface consisting of six elliptical electron pockets. The band structure of hexagonal FeSe shows abnormal temperature evolution behavior. With decreased temperature, parts of the bands shift downward to high binding energy while some bands shift upward to E_F. The shifts of these bands begin around 300 K and saturate at low temperature, indicating a magnetic phase-transition temperature of about 300 K. With increased film thickness, the Fermi surface topology and band structure show no obvious change except some minor quantum size effect or correlation effect.

II. EXPERIMENT

High-quality FeSe single-crystalline thin films were grown on the TiO_2 terminated and Nb-doped (001)-orientated single-crystal $SrTiO_3$ (0.5 wt %) (Shinkosha) substrate with the molecular-beam epitaxy (MBE) method following the previous reports [4,6]. It is reported [11] that NiAs-type hexagonal FeSe can be obtained on double-layer graphene formed on SiC grown at a low substrate temperature of 180 °C. At elevated substrate temperatures exceeding 420 °C, layer-by-layer growth of unstrained epitaxial films of tetragonal β-FeSe can be obtained. Hexagonal and tetragonal structured FeSe can also be grown on the tetragonal structured surface of $SrTiO_3$ (STO) depending on the substrate temperature. Superconducting tetragonal β-FeSe can be obtained at relatively high substrate temperature of 400–450 °C on TiO_2-terminated STO. When the substrate is kept at low temperature of about 300–350 °C, which is just the case of our experiment, we can get the hexagonal FeSe. The heterostructure of FeSe/STO is illustrated in Fig. 1(a), and the crystal structure of the obtained NiAs-type hexagonal FeSe film is shown in Fig. 1(b).

After growth, the film was directly transferred from the MBE chamber into the ARPES chamber with typical vacuum of 5×10^{-11} mbar. ARPES was conducted with 21.2 eV photons from a helium discharge lamp. A SCIENTA R4000 analyzer was used to record ARPES spectra with typical energy and angular resolutions of 10 meV and 0.2°, respectively. A freshly evaporated gold sample in electrical contact with the FeSe sample was served to calibrate E_F.

*dlfeng@fudan.edu.cn

 ©2017 American Physical Society

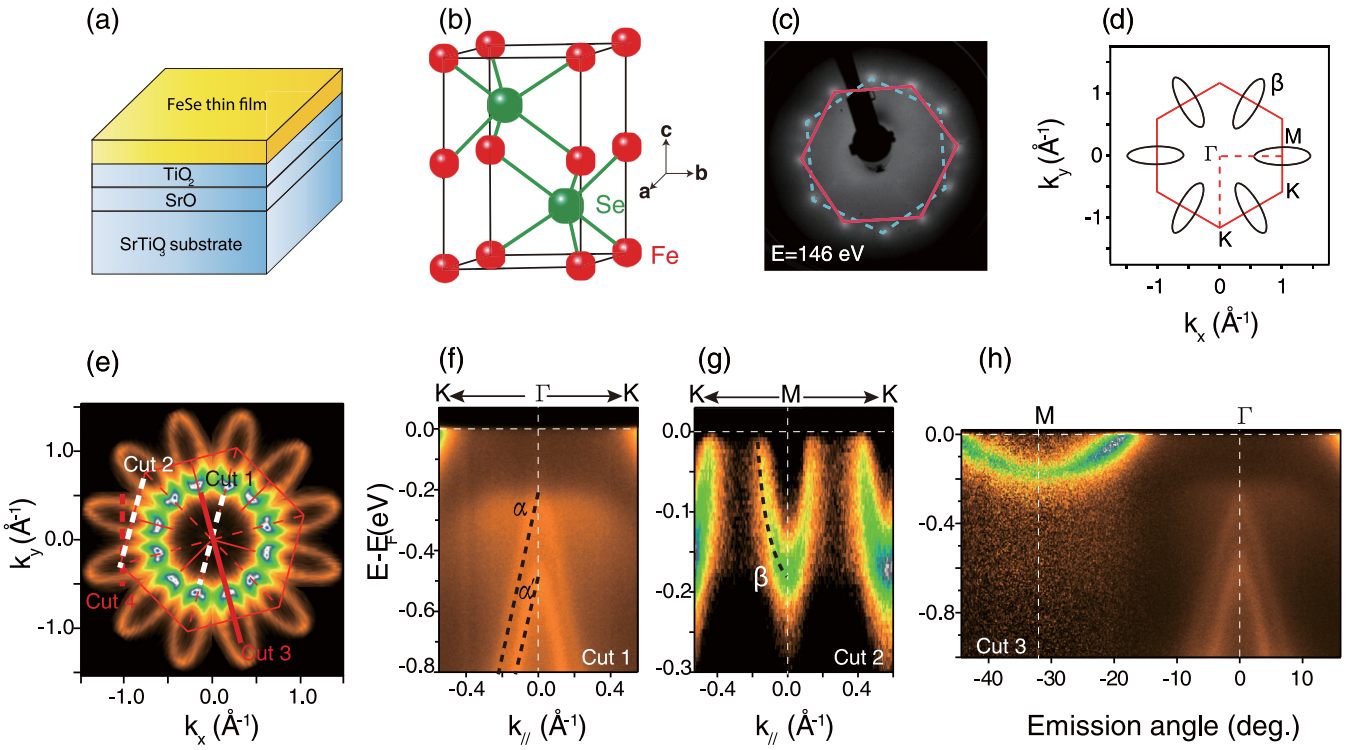

FIG. 1. Crystal and electronic structure of 1-UC hexagonal FeSe. (a) Schematic structure of the FeSe films on the STO substrate. (b) Hexagonal NiAs-type structure. (c) LEED pattern of 1-UC hexagonal FeSe thin film. (d) Fermi surface topology extract from (c) and (e). (e) Photoemission intensity map at E_F integrated over $[E_F - 10\,\text{meV}, E_F + 10\,\text{meV}]$. (f), (g) Photoemission intensity plots around Γ and M points, respectively. (h) Photoemission intensity plot along the Γ-M direction [cut 3 in (e)]. All the ARPES data were collected at 30 K.

III. RESULTS AND DISCUSSION

The electronic structure of 1-UC hexagonal FeSe thin film at 30 K is presented in Fig. 1. The photoemission intensity map is integrated over an $[E_F - 10\,\text{meV}, E_F + 10\,\text{meV}]$ window around the Fermi energy (E_F) as shown in Fig. 1(e). The observed Fermi surface consists of 12 elliptical electron pockets, which form a flowerlike pattern. The low-energy electron diffraction (LEED) pattern of hexagonal FeSe is shown in Fig. 1(c); two sets of sixfold symmetric diffraction pattern can be resolved, which indicate that two domain structures exist on the surface of hexagonal FeSe. Based on our ARPES and LEED data, the Fermi surface of single-domain hexagonal FeSe is extracted and drawn in Fig. 1(d), which contains only six elliptical electron pockets around each M point.

The low-energy band structure along the Γ-M direction is shown in Fig. 1(h). We can clearly observe an electronlike band (β) centered at the M point contributing to the elliptical pockets, whose band bottom is located at about E_F-0.6 eV [Fig. 1(g)]. Two nearly parallel holelike bands (α and α') can be seen below E_F at the Γ point [Fig. 1(f)], whose band top is located at E_F-0.2 eV and E_F-0.47 eV. The existence of only electron band crossing E_F shows that 1-UC hexagonal FeSe film is metallic with only electron Fermi pockets.

Hexagonal FeSe has always been found to be magnetic (ferrimagnetic or antiferromagnetic depending on the chemical compositions) [13,14]. The band structure of the magnetic materials often gets reconstructed across the magnetic transition [21–25]. To examine this, Fig. 2 presents the temperature dependence of the low-energy band structure of 1-UC hexagonal FeSe. The topologies of the electron (β) and hole (α and α') bands around Γ- and M points show no obvious change, but the positions of these bands shift with changed temperature. The band tops of α and α' gradually shift upward to E_F with decreasing temperature as shown in Fig. 2(a), while the band bottom of β gradually shifts downward to high binding energy as shown in Fig. 2(b).

We tracked the energy distribution curves (EDCs) at the center of α' and β bands to reveal the temperature-dependent band-structure evolution more precisely. The parallel α and α' bands show the same trend of energy shift with changing temperature; we only track the α' band with much higher intensity as representative. As shown in Fig. 2(c), the band top of α' locates at about E_F-0.47 eV at 30 K, which shifts downward with increasing temperature. The band top moved to about E_F-0.56 eV at 300 K and kept unchanged even as the temperature is further increased, which gives a max energy shift of 90 meV. For the β band, its band bottom locates at about E_F-0.16 eV at 30 K, which shifts upward with increasing temperature. The band bottom of β moved to about E_F-0.14 eV for 300 K and above temperature, which gives a max energy shift of 20 meV.

The temperature dependence of the Fermi surface and valence-band structure for 1-UC hexagonal FeSe are present in Fig. 3. The topology of the Fermi surface exhibits negligible change except some thermal broadening at high temperature, and there is no energy gap at the Fermi surface [Figs. 3(a1)

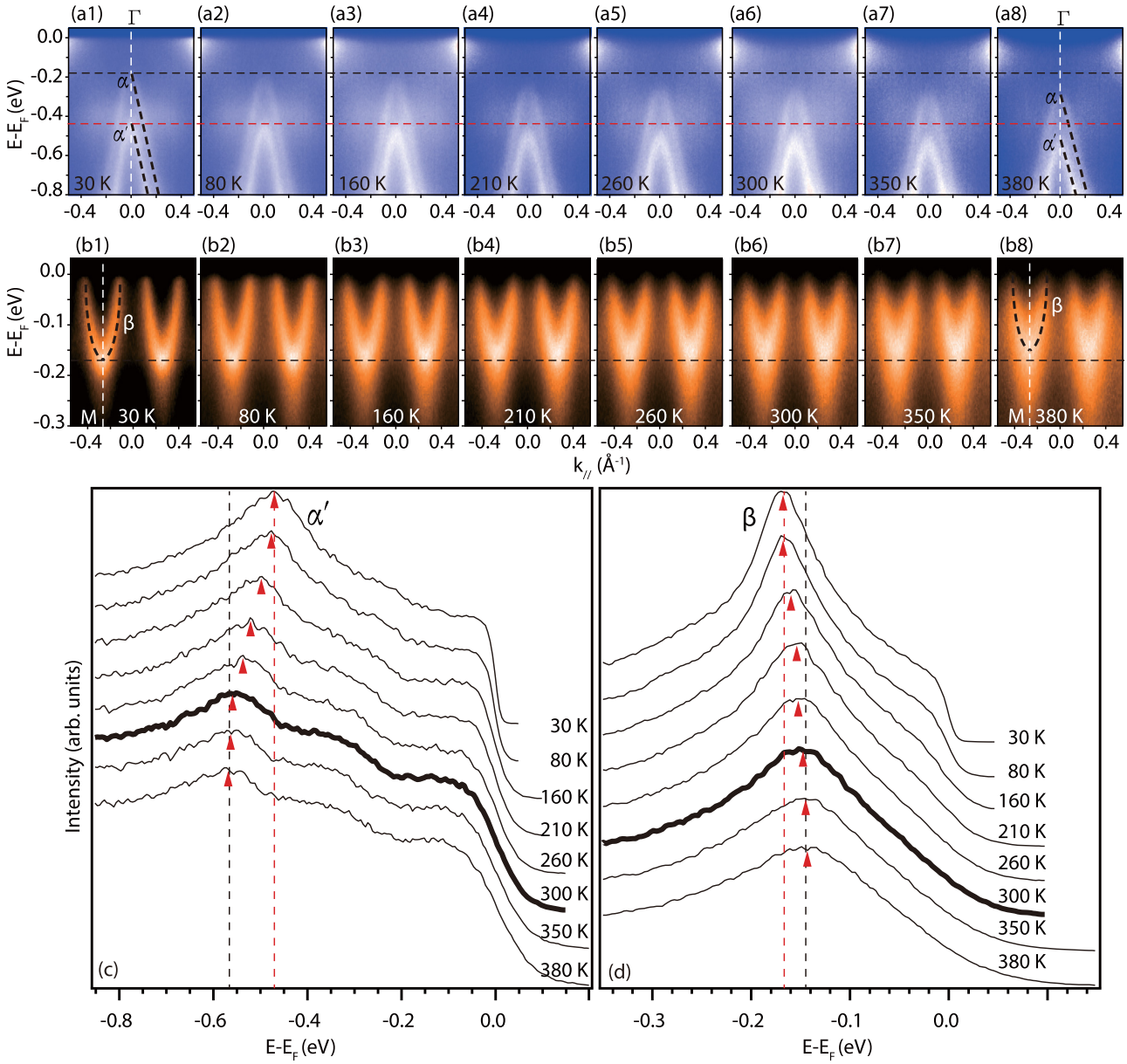

FIG. 2. Temperature dependence of the low-energy band structure for 1-UC hexagonal FeSe. (a1–a8) Temperature dependence of the band structure around the Γ point, [cut 1 in Fig. 1(e)]. (b1–b8) Temperature dependence of the band structure around the M point, [cut 4 in Fig. 1(e)]. (c) Temperature dependence of the EDCs at the Γ point; the peak position marked by the red triangle corresponds to the band top of α'. (d) Temperature dependence of the EDCs at the M point, the peak position marked by the red triangle correspond to the band bottom of β.

and 3(a2)]. To check if there are any other bands shifting with temperature except α/α' and β, we tracked the EDC around Γ and M points at various temperature as shown in Figs. 3(d) and 3(e). Interestingly, the η band at the Γ point shifts downward to high binding energy, while the ε band around the M point shifts upward to E_F with decreasing temperature. It is worth noticing that not all the bands shift with temperature; the characteristic peak at about E_F-2 eV stays unchanged at various temperatures [Fig. 3(d)]. To summarize, with decreased temperature, the max band shift is +90 and +80 meV upward for α/α' and ε, −20 and −15 meV downward for β and η. We note that the upward shifts are larger than the downward shifts with decreasing temperature, and it seems that the electronic energy is not reduced in the possible magnetic ground state. Presumably, the bands would shift toward higher binding energy to reduce energy, which is inconsistent with the actual situation; further studies are needed to fully understand this issue.

The Fermi surface and band structure of tetragonal FeSe thin films have been found to change dramatically with different thickness [6,9]. It is natural to ask whether the electronic structure of hexagonal FeSe has a similar thickness dependence. The electronic structure of 1-, 2-, and 6-UC hexagonal FeSe are shown in Fig. 4. Due to the mismatch of the lattice symmetry between hexagonal FeSe and tetragonal STO substrate, the sample quality become worse and worse with increased film thickness, and clear band dispersion cannot be detected in thick thin films. The obtained Fermi surface

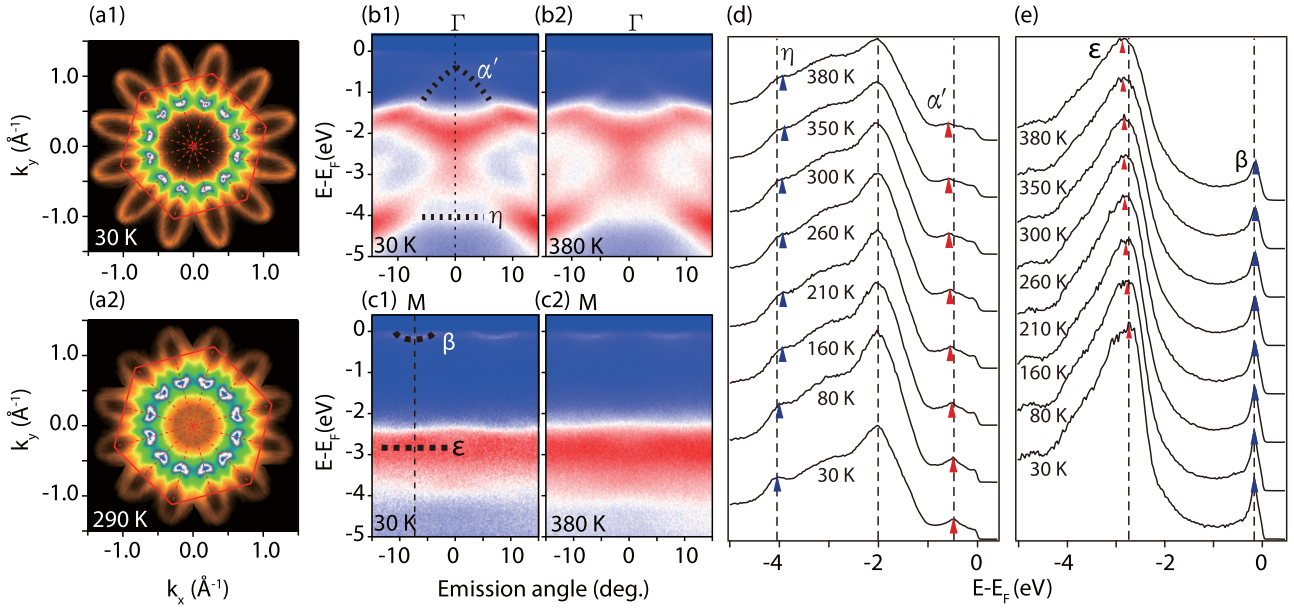

FIG. 3. Temperature dependence of the Fermi surface and valence-band structure for 1-UC hexagonal FeSe. (a1), (a2) Photoemission intensity map at 30 and 290 K, respectively. (b1), (b2) Photoemission intensity plots around the Γ point at 30 and 380 K, respectively. (c1), (c2) Photoemission intensity plots around the M point at 30 and 380 K, respectively. (d) Temperature dependence of the EDCs at Γ point; the red triangle marks the band top of α' and the blue triangle marks the band position of η. (e) Temperature dependence of the EDCs at the M point; the blue triangle marks the band bottom of β and the red triangle marks the band position of ε.

topology and valence-band structure show no dramatic change for different film thickness. However, subtle changes of some typical bands still exist in the valence-band structure around the Γ point. The positions of μ- and ν bands shift with changing film thickness, as marked and shown in Figs. 4(d)–4(f). The band bottom of ν shifts downward with increasing film thickness, while the μ band shifts upward as shown in Fig. 4(g). The intrinsic nature of this thickness-dependent band shift is

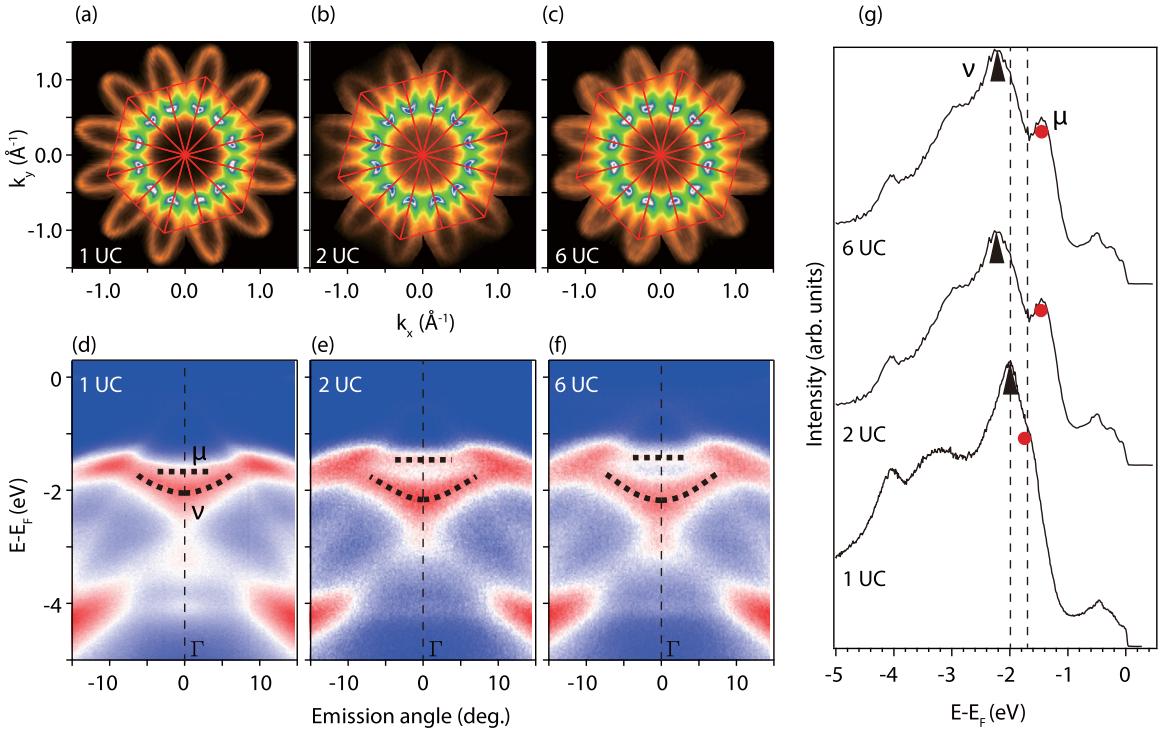

FIG. 4. Thickness dependence of the Fermi surface and valence-band structure for hexagonal FeSe at 30 K. (a)–(c) Photoemission intensity map of 1-, 2-, and 6-UC hexagonal FeSe, respectively. (d)–(f) Photoemission intensity plots around the Γ point of 1-, 2-, and 6-UC hexagonal FeSe, respectively. (g) Thickness dependence of the EDCs at the Γ point; the black triangle marks the band bottom of ν and the red circle marks the band position of μ.

not clear by now, which may be associated with the quantum size effect [26,27] or the reduced correlation with increased film thickness.

IV. DISCUSSION AND CONCLUSION

As the tetragonal and hexagonal phases of FeSe always intertwine with each other, it is difficult to prepare pure hexagonal phase of FeSe, which prevents the understanding of its electronic structure and magnetic properties. Using MBE method, we have successfully prepared pure phase of hexagonal structured FeSe and made it possible to study its electronic structure.

Considering the complex phase diagram of hexagonal FeSe, the primary task is to confirm which phase our thin-film sample is. McQueen *et al.* [10] reported two hexagonal phases in their paper: namely, alpha-$Fe_{1+x}Se$ (Fe excess phase) and gamma-Fe_7Se_8 (Se excess phase). Considering our thin-film fabrication process, the Se flux was kept 20 times greater than Fe by co-deposition during growth; it is unlikely that excess Fe can survive under such Se-rich condition (thus the Fe excess alpha-$Fe_{1+x}Se$ phase can be excluded). The low growth/annealing temperature used in our study should lead to a bit Se excess phase, which is named $FeSe_{1+x}$ in our paper [11].

According to the magnetic phase diagram [14] of hexagonal $FeSe_{1+x}$ reported by Terzieff and Komarek, hexagonal NiAs-type $FeSe_{1+x}$ exhibits both antiferromagnetism and ferrimagnetism depending on composition. $FeSe_{1+x}$ shows antiferromagnetism with compositions of $0.02 \leqslant x \leqslant 0.10$ (50.5 to 52.5 at % Se), ferrimagnetism is observed at compositions near $0.10 \leqslant x \leqslant 0.36$ (52.5 to 61.0 at % Se), and both the Néel and Curie temperatures vary with composition. Although the precise composition and the specific magnetic structure of our thin-film samples cannot be determined due to the lack of *in situ* characterization method, we can still study its magnetic properties by temperature-dependent electronic structure measurement, as the band structure for magnetic materials often gets reconstructed across their magnetic transition.

Indeed, we found that the electronic structure of our $FeSe_{1+x}$ film gets reconstructed when the temperature is varied, and the transition temperature is determined to be around 300 K. The band-shift behaviors observed in our hexagonal FeSe thin films are not exclusive to magnetic compounds. Similar band-shift behavior has been reported in $TaFe_{1.23}Te_3$, a spin-ladder compound with an antiferromagnetic ground state [28]. It is proposed that $TaFe_{1.23}Te_3$ is the second kind of novel quantum material in addition to the parent compounds of iron-based superconductors, whose antiferromagnetic transition directly correlates with the electronic structure reconstruction at high binding energies. The similar band-shift behaviors found in hexagonal FeSe and $TaFe_{1.23}Te_3$ give strong evidence that possible magnetic transition happens in $FeSe_{1+x}$ film. With a simple chemical and crystal structure, clear experimental band dispersion, the hexagonal $FeSe_{1+x}$ provides an excellent platform for experimental and theoretical study of the mechanism for magnetic transition in FeSe-related systems.

In summary, we report *in situ* angle-resolved photoemission spectroscopy study of hexagonal FeSe thin films. The hexagonal FeSe is found to be metallic, with a Fermi surface consisting of six elliptic electron pockets. With decreased temperature, parts of the bands shift downward to high binding energy while some bands shift upward to E_F. The shifts of these bands begin around 300 K, and saturate at low temperature, indicating a magnetic phase-transition temperature of about 300 K. With increased film thickness, the Fermi surface topology and band structure show no obvious change. Our paper shows that the possible magnetic transition in hexagonal FeSe is driven by electronic structure reconstruction, which is crucial to understand the origin of the magnetism in NiAs-type FeSe.

ACKNOWLEDGMENTS

We gratefully acknowledge helpful discussions with Prof. X. G. Gong, X. Dai, and Dr. H. Y. Cao. This work is supported by the Foundation of President of China Academy of Engineering Physics (Grant No. 201501037), and the National Science Instruments Major Project of China (Grant No. 2012YQ130125).

[1] F. C. Hsu, J. Y. Luo, K. W. Yeh, T. K. Chen, T. W. Huang, P. M. Wu, Y. C. Lee, Y. L. Huang, Y. Y. Chu, D. C. Yan, and M. K. Wu, Proc. Natl. Acad. Sci. USA **105**, 14262 (2008).

[2] S. Medvedev, T. M. McQueen, A. Troyan, T. Palasyuk, M. I. Eremets, R. J. Cava, S. Naghavi, F. Casper, V. Ksenofontov, G. Wortmann, and C. Felser, Nat. Mater. **8**, 630 (2009).

[3] D. Liu, W. Zhang, D. Mou, J. He, Y. B. Ou, Q. Y. Wang, Z. Li, L. Wang, L. Zhao, S. He, Y. Peng, X. Liu, C. Chen, L. Yu, G. Liu, X. Dong, J. Zhang, C. Chen, Z. Xu, J. Hu *et al.*, Nat. Commun. **3**, 931 (2012).

[4] Q.-Y. Wang, Z. Li, W.-H. Zhang, Z.-C. Zhang, J.-S. Zhang, W. Li, H. Ding, Y.-B. Ou, P. Deng, K. Chang, J. Wen, C.-L. Song, K. He, J.-F. Jia, S.-H. Ji, Y.-Y. Wang, L.-L. Wang, X. Chen, X.-C. Ma, and Q.-K. Xue, Chin. Phys. Lett. **29**, 037402 (2012).

[5] S. He, J. He, W. Zhang, L. Zhao, D. Liu, X. Liu, D. Mou, Y.-B. Ou, Q.-Y. Wang, Z. Li, L. Wang, Y. Peng, Y. Liu, C. Chen, L. Yu, G. Liu, X. Dong, J. Zhang, C. Chen, Z. Xu *et al.*, Nat. Mater. **12**, 605 (2013).

[6] S. Y. Tan, Y. Zhang, M. Xia, Z. R. Ye, F. Chen, X. Xie, R. Peng, D. F. Xu, Q. Fan, H. C. Xu, J. Juan, T. Zhang, X. C. Lai, T. Xiang, J. P. Hu, B. P. Xie, and D. L. Feng, Nat. Mater. **12**, 634 (2013).

[7] W. Zhang, Y. Sun, J. Zhang, F. Li, M. Guo, Y. Zhao, H. Zhang, J. Peng, Y. Xing, H. Wang, T. Fujita, A. Hirata, Z. Li, H. Ding, C. Tang, M. Wang, Q. Wang, K. He, S. Ji, X. Chen *et al.*, Chin. Phys. Lett. **31**, 017401 (2013).

[8] J. F. Ge, Z. L. Liu, C. Liu, C. L. Gao, D. Qian, Q. K. Xue, Y. Liu, and J. F. Jia, Nat. Mater. **14**, 285 (2014).

[9] J. J. Lee, F. T. Schmitt, R. G. Moore, S. Johnston, Y. T. Cui, W. Li, M. Yi, Z. K. Liu, M. Hashimoto, Y. Zhang, D. H. Lu, T. P. Devereaux, D. H. Lee, and Z. X. Shen, Nature (London) **515**, 245 (2014).

[10] T. M. McQueen, Q. Huang, V. Ksenofontov, C. Felser, Q. Xu, H. Zandbergen, Y. S. Hor, J. Allred, A. J. Williams, D. Qu, J. Checkelsky, N. P. Ong, and R. J. Cava, Phys. Rev. B **79**, 014522 (2009).

[11] C.-L. Song, Y.-L. Wang, Y.-P. Jiang, Z. Li, L. Wang, K. He, X. Chen, X.-C. Ma, and Q.-K. Xue, Phys. Rev. B **84**, 020503 (2011).

[12] L. Li, Z. R. Yang, Y. P. Sun, J. Y. Zhang, D. Z. Shen, and Y. H. Zhang, Supercond. Sci. Technol. **24**, 015010 (2011).

[13] T. Hirone, S. Maeda, and N. Tsuya, J. Phys. Soc. Jpn. **9**, 496 (1954).

[14] P. Terzieff and K. L. Komarek, Monatsh. Chem. **109**, 1037 (1978).

[15] G. Long, H. Zhang, D. Li, R. Sabirianov, Z. Zhang, and H. Zeng, Appl. Phys. Lett. **99**, 202103 (2011).

[16] J. Wang, H. Duan, X. Lin, V. Aguilar, A. Mosqueda, and G.-M. Zhao, J. Appl. Phys. **112**, 103905 (2012).

[17] X. J. Wu, Z. Z. Zhang, J. Y. Zhang, B. H. Li, Z. G. Ju, Y. M. Lu, B. S. Li, and D. Z. Shen, J. Appl. Phys. **103**, 113501 (2008).

[18] D. Wei, J. Liang, Y. Zhu, L. Hu, K. Zhang, J. Zhang, Z. Yuan, and Y. Qian, Electrochem. Commun. **38**, 124 (2014).

[19] L. Craco and S. Leoni, EPL **92**, 67003 (2010).

[20] Q. J. Feng, D. Z. Shen, J. Y. Zhang, B. S. Li, B. H. Li, Y. M. Lu, X. W. Fan, and H. W. Liang, Appl. Phys. Lett. **88**, 012505 (2006).

[21] A. Takayama, S. Souma, T. Sato, T. Arakane, and T. Takahashi, J. Phys. Soc. Jpn. **78**, 073702 (2009).

[22] L. X. Yang, Y. Zhang, H. W. Ou, J. F. Zhao, D. W. Shen, B. Zhou, J. Wei, F. Chen, M. Xu, C. He, Y. Chen, Z. D. Wang, X. F. Wang, T. Wu, G. Wu, X. H. Chen, M. Arita, K. Shimada, M. Taniguchi, Z. Y. Lu *et al.*, Phys. Rev. Lett. **102**, 107002 (2009).

[23] H. J. Noh, J. Jeong, B. Chang, D. Jeong, H. S. Moon, E. J. Cho, J. M. Ok, J. S. Kim, K. Kim, B. I. Min, H. K. Lee, J. Y. Kim, B. G. Park, H. D. Kim, and S. Lee, Sci. Rep. **4**, 3680 (2014).

[24] B. Kim, A. B. Andrews, J. L. Erskine, K. J. Kim, and B. N. Harmon, Phys. Rev. Lett. **68**, 1931 (1992).

[25] T. Takahashi, Y. Naitoh, T. Sato, T. Kamiyama, K. Yamada, H. Hiraka, Y. Endoh, M. Usuda, and N. Hamada, Phys. Rev. B **63**, 094415 (2001).

[26] Y. Guo, Y.-F. Zhang, X.-Y. Bao, T.-Z. Han, Z. Tang, L.-X. Zhang, W.-G. Zhu, E. G. Wang, Q. Niu, Z. Q. Qiu, J.-F. Jia, Z.-X. Zhao, and Q.-K. Xue, Science **306**, 1915 (2004).

[27] S. Qin, J. Kim, Q. Niu, and C.-K. Shih, Science **324**, 1314 (2009).

[28] M. Xu, L.-M. Wang, R. Peng, Q.-Q. Ge, F. Chen, Z.-R. Ye, Y. Zhang, S.-D. Chen, M. Xia, R.-H. Liu, M. Arita, K. Shimada, H. Namatame, M. Taniguchi, M. Matsunami, S. Kimura, M. Shi, X.-H. Chen, W.-G. Yin, W. Ku *et al.*, Chin. Phys. Lett. **32**, 027401 (2015).

PHYSICAL REVIEW B **93**, 121102(R) (2016)

Origin of the kink in the band dispersion of the ferromagnetic perovskite $SrRuO_3$: Electron-phonon coupling

H. F. Yang,[1,2] Z. T. Liu,[1,2] C. C. Fan,[1,2] Q. Yao,[1,3] P. Xiang,[1,2] K. L. Zhang,[1,2] M. Y. Li,[1,2] H. Li,[1,2] J. S. Liu,[1,2] D. W. Shen,[1,2,*] and M. H. Jiang[1]

[1]*State Key Laboratory of Functional Materials for Informatics, Shanghai Institute of Microsystem and Information Technology (SIMIT), Chinese Academy of Sciences, Shanghai 200050, China*

[2]*CAS-Shanghai Science Research Center, Shanghai 201203, China*

[3]*State Key Laboratory of Surface Physics, Department of Physics, and Advanced Materials Laboratory, Fudan University, Shanghai 200433, China*

(Received 24 January 2016; published 4 March 2016)

Perovskite $SrRuO_3$, a prototypical conductive ferromagnetic oxide, exhibits a kink in its band dispersion signaling the unusual electron dynamics therein. However, the origin of this kink remains elusive. By taking advantage of the combo of reactive molecular beam epitaxy and *in situ* angle-resolved photoemission spectroscopy, we systematically studied the evolution of the low-energy electronic structure of $SrRuO_3$ films with thickness thinning down to a nearly two-dimensional limit in a well-controlled way. The kink structure persists even in the four-unit-cell-thick film. Moreover, through quantitative self-energy analysis, we observed the negligible thickness dependence of the binding energy of the kink, which is in sharp contrast to the downward trend of the Curie temperature with reducing the film thickness. Together with previously reported transport and Raman studies, this finding suggests that the kink of perovskite $SrRuO_3$ should originate from the electron-phonon coupling rather than magnetic collective modes, and the in-plane phonons may play a dominant role. Considering such a kink structure of $SrRuO_3$ is similar to those of many other correlated oxides, we suggest the possible ubiquity of the coupling of electrons to oxygen-related phonons in correlated oxides.

DOI: 10.1103/PhysRevB.93.121102

I. INTRODUCTION

In correlated oxides, the delicate interplay of charge, spin, lattice, and orbital manifested by various collective excitations, gives rise to a wealth of fascinating quantum phenomena, such as metal-insulator transition [1], high-T_c superconductivity [2,3], colossal magnetoresistance [4], and multiferroics [5]. Among these compounds, perovskite $SrRuO_3$—a moderately correlated conductive ferromagnet [6–8]—has attained continuous interests. On the application side, it is widely utilized as conductive electrodes due to the good stability and structural compatibility with other correlated oxides [7]; meanwhile, it is explored to be a key integrant in fabricating oxide heterostructures/superlattices [9–17], which may contribute to new functionalities in electronics and spintronics [7]. From the viewpoint of fundamental studies, $SrRuO_3$ is a simple but profound model system to explore how many-body interactions determine the physical properties [18–22], and the underlying mechanism may provide a hint on novel physics of other correlated oxides including the unconventional superconductivity in Sr_2RuO_4 [23] and quantum criticality in $Sr_3Ru_2O_7$ [24].

For correlated oxides, a kink in the low-energy band dispersion reflects the unusual electron dynamics—the scattering rate of electrons has been altered within a narrow energy range—which usually implies the existence of pronounced coupling between electrons and various collective excitations [3,25–29]. Thus, the interpretation of the kink is of significance to understand the essential effects on physical properties of correlated systems. For example, there have been lasting and intense debates on whether the kinklike feature discovered in the dispersion of cuprate superconductors stems from spin fluctuations or lattice waves (phonons), which is intimately related with the fundamental understanding of the pairing mechanism of high-T_c superconductivity [3,28,29]. For $SrRuO_3$, previous studies have reported a kinklike feature in its band dispersion [18], which suggests remarkable renormalization of low-energy electrons by some collective modes. However, the details of which mode is most relevant have not been completely explored yet.

In this Rapid Communication, we took advantage of the reactive molecular beam epitaxy (MBE) to fabricate a series of high-quality $SrRuO_3$ thin films with well-controlled thickness. Through tuning the extra knob of dimensionality, we can effectively adjust the ferromagnetism and meanwhile keep the basic crystal structure of films, which is expected to result in the pronounced dichroism between the possible electron-phonon and electron-magnon interactions in films. Consequently, we performed a systematic *in situ* angle-resolved photoemission spectroscopy (ARPES) study of the kink structure to pin down which boson modes are most relevant. We found that the kink persists in a film as thin as four unit cells (uc). Through quantitative self-energy analysis, we found that, while the film thickness was progressively reduced, the kink energy remained around 62 meV below the Fermi level (E_F). This observation, together with reported thickness dependent Curie temperature (T_C) and Raman studies of phonons, suggests that the kink in $SrRuO_3$ originates from the strong electron-phonon coupling, and the collective magnetic excitations may have little contribution. By referring to other correlated oxides exhibiting similar kinklike structure, we

*dwshen@mail.sim.ac.cn

 ©2016 American Physical Society

infer that the electron-phonon coupling may be ubiquitous in correlated oxides.

II. EXPERIMENT

High-quality single crystalline $(001)_p$ (where p denotes pseudocubic indices) $SrRuO_3$ thin films with a spectrum of thicknesses were fabricated on $(001)_p$ $NdGaO_3$ substrates (without special treatment; mixed termination) using a reactive MBE system (DCA R450). The in-plane lattice constant of $(001)_p$ $NdGaO_3$ is 3.865 Å, which leads to a 1.65% compressive strain to the pseudocubic $SrRuO_3$ (3.93 Å). The shuttered growth mode was applied to synthesize films in the distilled ozone atmosphere of 1.0×10^{-6} Torr. During the growth, the temperature of substrates was kept at 600 °C according to the thermocouple behind the sample stage. Moreover, the overall growth rate and surface structure of thin films were monitored by *in situ* reflection high-energy electron diffraction (RHEED) during growth. Strontium (Sr) and ruthenium (Ru) were evaporated from a thermal Knudsen cell and an electron-beam evaporator with delicate feedback control of flux, respectively. The Sr and Ru fluxes were approximately 1.2×10^{13} atoms/(cm^2 s), which were checked before and after the deposition by a quartz crystal microbalance.

Figures 1(a1) and 1(a2) display the typical RHEED patterns of a 21-uc-thick $SrRuO_3$ epitaxial thin film taken along $[100]_p$ and $[110]_p$ azimuth directions, respectively. The remarkable shiny spots and visible Kikuchi lines reveal the fine surface with long-range ordered lattice structure. The amplitudes and periods of RHEED intensity oscillations of the [00] and [01] diffraction rods tend to be constant, indicating the layer-by-layer and stoichiometric growth of this film [30]. Note that each oscillation represents the growth of one layer of $SrRuO_3$, as depicted in Fig. 1(b). Consequently, closing/opening the Sr/Ru shutters according to the RHEED intensity curve can intentionally control the thickness of thin film. In this way, the thicknesses of all $SrRuO_3$ films in this work were well controlled. As shown in the inset of Fig. 1(c), the morphology of a typical four-uc-thick film measured by atomic force microscope illustrates a surface roughness of only 0.13 nm, which guarantees the well-controlled thickness of the ultrathin films and following ARPES measurements. The typical x-ray diffraction (XRD) of the $SrRuO_3$ film is shown in Fig. 1(c). The θ-2θ scan result is consistent with the growth of phase-pure $(001)_p$-oriented $SrRuO_3$. The clear Kiessig interface fringes indicate the sharp and smooth interfaces between the thin film and substrate. The scheme of the thickness control could be further confirmed by the explicit fitting of Keissig fringes in the XRD pattern [31]. For example, the best fit to the θ-2θ scan around the 002 diffraction peak [Fig. 1(d)] gives a thickness of 21 uc, which is in good agreement with that determined by counting RHEED oscillations.

After growth, the film was cooled down to 200 °C and then immediately transferred to the ARPES chamber within 5 min through a transfer chamber bridging the MBE and ARPES with a vacuum of around 1.0×10^{-10} Torr. In so doing, a clean sample surface is expected to be preserved [18]. Then ARPES measurements were performed with a Specs UVLS monochromatized helium discharging lamp (He Iα, 21.2 eV) and a VG Scienta R8000 analyzer under an ultrahigh vacuum

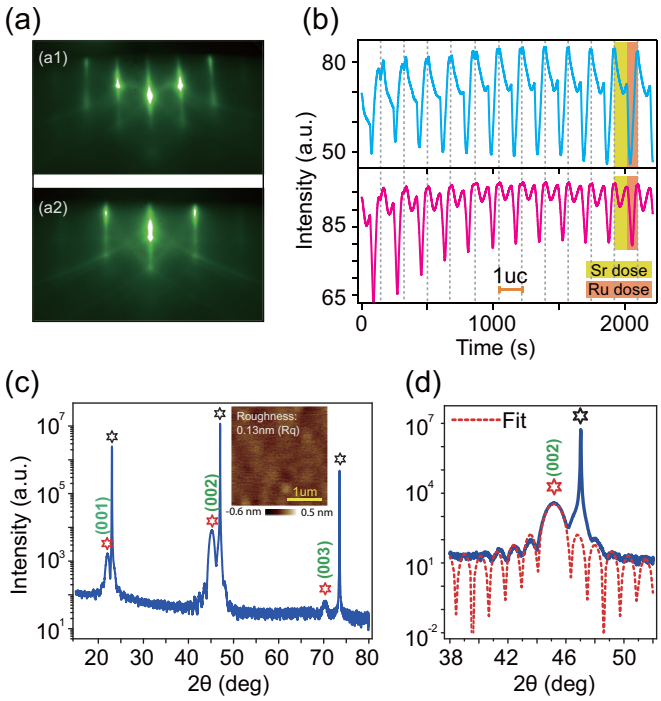

FIG. 1. MBE growth and characterization of $SrRuO_3$ thin films with well-controlled thicknesses. (a) Typical RHEED patterns of a 21-uc-thick $SrRuO_3$ epitaxial thin film. (a1) and (a2) are taken along $[100]_p$ and $[110]_p$ azimuth directions, respectively. (b) RHEED intensity curve: time dependence of the intensities of [00] and [01] diffraction spots in the $[100]_p$ RHEED pattern (a1). Each oscillation framed by two adjacent dotted lines represents the growth of 1 uc $SrRuO_3$ thin film. (c) The typical x-ray diffraction θ-2θ scan of a 21 uc $SrRuO_3$ thin film whose nominal thickness is determined by counting the number of RHEED oscillations. Red markers represent diffraction peaks of the film, while black ones represent those of the $NdGaO_3$ substrate. The inset shows the morphology of a typical four uc $SrRuO_3$ thin film measured by atomic force microscope, which gives a rather flat surface with a roughness of only 0.13 nm (Rq). (d) A close-up of the 002 diffraction peak of this 21 uc $SrRuO_3$ film, showing clear Keissig fringes. The red dotted line is the best fit to the data, which gives the thickness of 21 uc, in good agreement with the nominal thickness determined by counting the RHEED oscillations.

of 8.0×10^{-11} Torr. Thin films were measured at 14 K with an energy resolution of 10.5 meV and angle resolution of 0.3°. The E_F was referenced to that of a polycrystalline gold newly deposited and electrically connected to samples. We note that finite density of states near E_F persists in even two-uc-thick film, which is in line with the best $SrRuO_3$ films ever reported [19]. In order to avoid the photoemission charging effect due to the insulating behavior of the $NdGaO_3$ substrate, conducting silver paste was used to carefully cover edges of the substrate. In all cases, we experimentally conformed that no charging effect occurred through photon flux test. Also, no apparent signs of degradation were observed during measurements.

III. RESULTS AND DISCUSSIONS

Figure 2(a1) displays the band dispersion of one typical 14-uc-thick $SrRuO_3$ film along the (0,0)-(0,π) high-symmetry

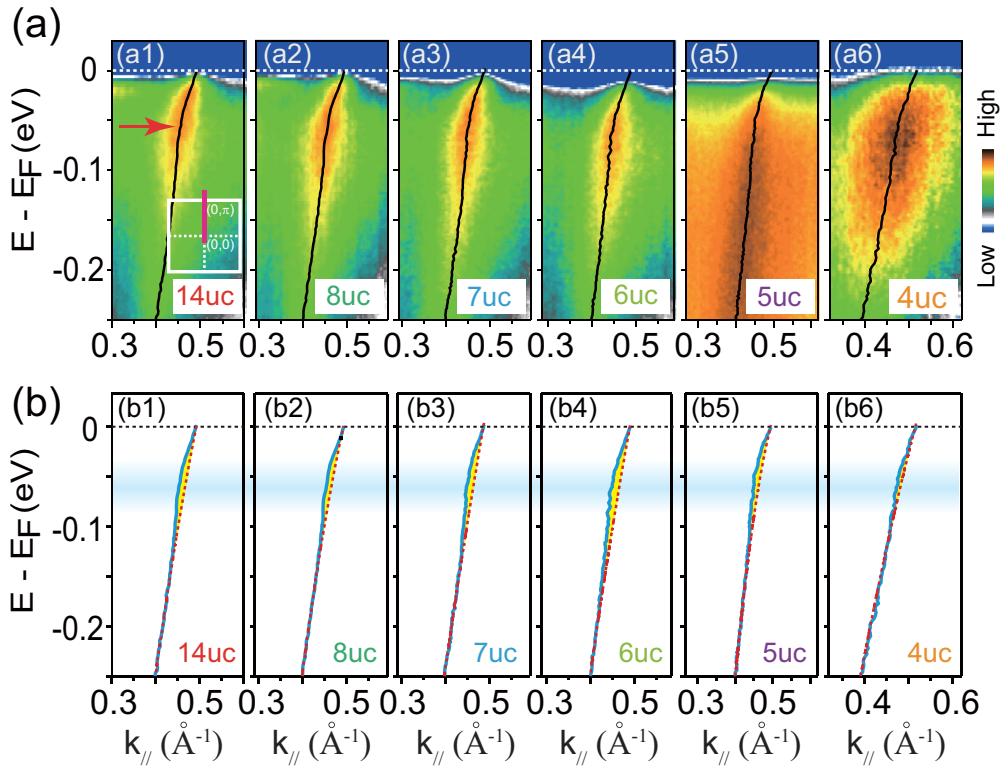

FIG. 2. The kink exists in all $SrRuO_3$ films down to four uc thick. (a) The photoemission intensity spectra of $SrRuO_3$ films with various thicknesses near E_F along the (0, 0)-(0,π) high-symmetry direction as shown by the inset of (a1). The black lines overlaid are extracted band dispersions obtained through fitting MDCs spaced by 3 meV with Lorentz functions. Red arrow in (a1) roughly marks the energy position of the kink. (b) Extracted band dispersions with bare bands obtained by polynomial fittings with an order of two as indicated by dotted red lines. The difference between the extracted band dispersion and the polynomial bare band is treated as the self-energy denoted by the yellow shadow. The kink structure is present in all films ranging from 14 to 4 uc.

direction (see the inset). Consistent with the previous report [18], the quasi-one-dimensional band β exhibits sharp quasiparticle peaks, indicating that the sample is indeed in the Fermi liquid regime. The overlaid black curve is the exacted dispersion by fitting momentum distribution curves (MDCs) with Lorentzian functions. It is evident that the slope of the dispersion near E_F is significantly smaller than that of the high-binding-energy part (−0.15 eV to −0.25 eV). Such an abrupt change of the slope is the key characteristic of the kink structure signaling significant electron-boson coupling [18,32,33]. As displayed in Figs. 2(a1)–2(a6), while the film thickness keeps decreasing, the kink structure persists in the dispersion of the band β, and can even be observed in a four-uc-thick film [Fig. 2(a6)], aside from the broader background and smaller slope of the high-binding-energy part partially due to the increasing electron correlations induced by reducing the dimensionality [34]. For films with less than four uc, the dispersion is too broad to extract the kink structure, while finite spectral weight near the E_F still remains in two-uc-thick films (not shown).

To identify such kink evolution with dimensionality in an accurate way, quantitative self-energy analysis was carried out [18,26]. Here the self-energy is handled in a practical way, which was proved to be effective in identifying the kink [18,26]. We first fitted the band β (specifically the high-binding-energy part) with a polynomial function with an order of two to approximately yield the bare band dispersion marked by red dotted lines in Figs. 2(b1)–2(b6); consequently, by subtracting the exacted band with the fitted bare band, we can obtain the the real part of the self-energy $\Sigma'(\omega)$, as marked by yellow shadows in Fig. 2(b). Figure 3(a) illustrates the thickness dependence of $\Sigma'(\omega)$. Each curve evidently shows a maxima which can be used to mark the energy position of the kink. It is found that the kink structure is always located at around 62 meV below E_F, as highlighted by the gradient cyan shadow. Such a result can be also confirmed by the imaginary part of the self-energy $\Sigma''(\omega)$ analysis, which is directly related with momentum distribution curve (MDC) peak widths [see Fig. 3(b)]. As we can see, each $\Sigma''(\omega)$ curve exhibits a characteristic steplike increase, implying the sudden change of the scattering rate of electrons. With the decreasing of the film thickness, the steplike feature's characteristic energy remains around 62 meV (binding energy) as well, in line with the $\Sigma'(\omega)$ analysis. We can further estimate the kink energy of each film by applying Gaussian fitting to the maxima region of the $\Sigma'(\omega)$, given that the maxima region of the $\Sigma'(\omega)$ qualitatively adopts the Gaussian function shape. As shown by the left axis of Fig. 4(a), the kink energy qualitatively remains unchanged with film thickness.

Perovskite $SrRuO_3$ was reported to host a fundamental thickness limit of the long-range ferromagnetism: the Curie temperature T_C keeps decreasing with thinning the film [19], as illustrated by the reproduced data in Fig. 4(a) (the right axis). In a typical itinerant ferromagnet, the effective exchange

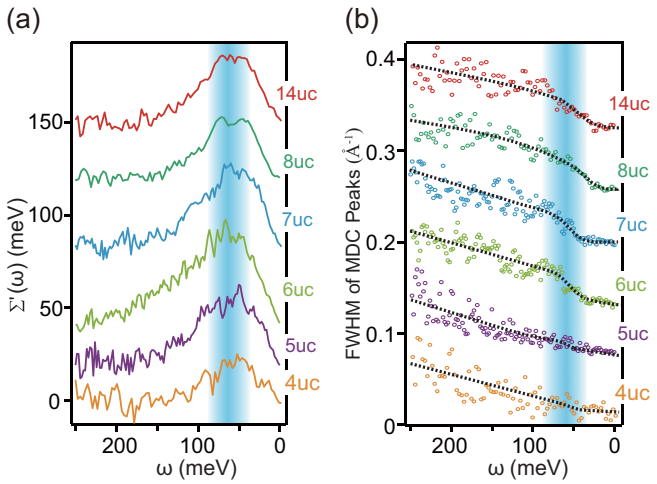

FIG. 3. Negligible thickness dependence of the kink in $SrRuO_3$. (a) Real part [$\Sigma'(\omega)$] analyses of the self-energies of films. Offsets are used to display those curves clearly, and no normalizations are applied. The gradient cyan shadow area indicates the maxima region of the real part of the self-energies, which denotes the binding energies of the kinks. All kinks occur at around 62 meV below the E_F. (b) Corresponding imaginary part [$\Sigma''(\omega)$, can be represented by the FWHM of MDC peaks] analyses of self-energies. To display these data clearly, offsets and normalizations of "amplitude" (difference between the biggest and smallest FWHMs in one film) are used. In addition, black dotted lines are used as guides to the eyes. The gradient cyan shadow marks the abrupt change of the imaginary part, which represents the kink. All kinks occur at around 62 meV below the E_F, which is in accordance with the real part analyses in (a).

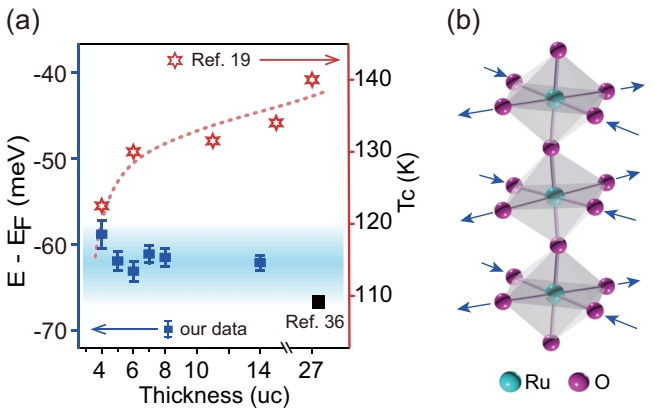

FIG. 4. Electron-phonon coupling origin of the kink in $SrRuO_3$. (a) Left axis: measured negligible thickness dependence of the energy position of the kink. The kink energy is extracted by applying Gaussian function fitting to the maxima region of the real part of self-energy. Right axis: reported thickness dependence of the Curie temperature (Ref. [19]). The black rectangular marker displays the energy scale of in-phase stretching phonon mode proposed by the combined studies of Raman spectroscopy and calculation (Ref. [36]). (b) Schematic of in-phase stretching phonon mode (associated with the movement of in-plane oxygen atoms as marked by blue arrows) (Ref. [36]), based on the perovskite structure of $SrRuO_3$ which is constituted of oxygen octahedra connected by oxygen atoms (note that Sr atoms are not drawn for simplicity).

interaction J is expected to be proportional to the T_C, and thus the energy of spin waves or magnons, which is proportional to the spin wave stiffness $D \propto J$, would be reduced as the T_C decreases. If the kink structure of $SrRuO_3$ indeed originates from the electron-magnon coupling, the energy of the kink should have shown an evident downward trend with thinning the film. However, by contrast, the binding energy of the kink shows negligible thickness dependence as illustrated in Fig. 4(a) (the left axis). In addition, for another two members of the Ruddlesden-Popper (RP) series of ruthenates, Sr_2RuO_4 and $Sr_3Ru_2O_7$, whose magnetic ground states are totally different from $SrRuO_3$, the spectral behaviors of the kinks are similar to that of $SrRuO_3$ [25]. Therefore, we suggest that the collective magnetic excitations may have little contribution to the kink of $SrRuO_3$. Alternately, it was proposed that strong electron-electron interaction could solely lead to the formation of a kink in the electron band [32,35] as well, which however is not the case of $SrRuO_3$ since $SrRuO_3$ is known as a moderately correlated without well-separated sub-Hubbard band [7].

On the other hand, the combined study of Raman spectroscopy and lattice dynamical calculations revealed that perovskite $SrRuO_3$ films possess the prominent in-phase stretching mode in the phonon spectra [as illustrated in Fig. 4(b) schematically], the energy scale of which (540 $cm^{-1} \sim 67$ meV) is remarkably close to our measured kink's binding energy 62 meV [36]. In addition, such bond-stretching phonons with similar energy scale have been well identified as the origin of the kink structure in the band dispersion of RP-structured manganite $La_{2-2x}Sr_{1+2x}Mn_2O_7$ [27]. Thus, it is most probable that the coupling of electrons to the bond-stretching phonons plays a dominant role in the formation of kink in perovskite $SrRuO_3$ films. Indeed, since in-plane phonon mainly involves in-plane movements of atoms, its mode energy should not notably change with driving $SrRuO_3$ to two-dimensional limit.

As mentioned above, for two other members of RP-structured ruthenates, Sr_2RuO_4 and $Sr_3Ru_2O_7$ both show the kink structure with the same binding energy in the band dispersion [25]. Considering their more two-dimensional electronic structure and negligible thickness dependence of kink in perovskite $SrRuO_3$ think films, it is natural to assign these phenomena to the coupling of electrons to the *in-plane* stretching phonon branch. Moreover, such kink structure in the band dispersion was also observed in many other correlated oxides, such as various cuprate superconductors [28,29] and $SrVO_3$ [26]. In terms of crystal structure, these compounds belong to the perovskite and layered perovskite oxide family, which are constituted of oxygen octahedra/tetrahedra connected by oxygen atoms [see the structure of $SrRuO_3$ in Fig. 4(b) as an example]. The vibration of oxygen atoms, together with various tilts and distortions of similar oxygen octahedra would lead to considerable phonon modes. Once such phonon modes couple with electrons, renormalization with cut-off binding energies may occur and the scattering rate near the E_F may be changed as well, thus forming a kink in the band dispersion.

Thus, we suggest that the interaction between electrons and phonons may be ubiquitous (in many cases even form

a kink in the band dispersion, as discussed above) and then impact the physical performance of correlated oxides with the transition-metal–oxygen octahedra units. Particularly, this kind of coupling has also been considered to be important in understanding the formation of Cooper pairs in cuprates [28,33], and the colossal magnetoresistance effect in manganites [27]. The studies of electron-phonon coupling in ruthenates may provide opportunities to uncover the roles phonons play in these novel materials.

IV. CONCLUSION

To summarize, we have utilized the delicate combo of reactive MBE and *in situ* ARPES to systematically study the kink structure of $SrRuO_3$ thin films with various well-controlled thicknesses. The kink structure exists in all $SrRuO_3$ films (even in four-uc-thick films). Moreover, through quantitative self-energy analysis, we observed that all kinks approximately occur at around 62 meV below the E_F. This observation, and comparisons with other oxides, together with reported transport and Raman studies, demonstrate that the kink originates from the the strong electron-phonon coupling other than electron-magnon coupling. In addition, we discussed the possible ubiquity of electron-phonon coupling in correlated oxides. Our work not only uncovers the kink origin of $SrRuO_3$ and gives a hint on fundamental exploration of other correlated oxides, but also demonstrates that the *in situ* MBE and ARPES system could be a powerful toolkit in studying novel quantum materials.

ACKNOWLEDGMENTS

We gratefully acknowledge the helpful discussions with Professor Xiangang Wan. This work was supported by National Basic Research Program of China (973 Program) under Grant No. 2012CB927401 and the National Science Foundation of China under Grants No. 11274332 and No. 11227902. H.F.Y. and D.W.S. are also supported by the "Strategic Priority Research Program (B)" of the Chinese Academy of Sciences (Grant No. XDB04040300).

[1] M. Imada, A. Fujimori, and Y. Tokura, Rev. Mod. Phys. **70**, 1039 (1998).
[2] P. A. Lee, N. Nagaosa, and X.-G. Wen, Rev. Mod. Phys. **78**, 17 (2006).
[3] A. Damascelli, Z. Hussain, and Z.-X. Shen, Rev. Mod. Phys. **75**, 473 (2003).
[4] M. B. Salamon and M. Jaime, Rev. Mod. Phys. **73**, 583 (2001).
[5] R. Ramesh and N. A. Spaldin, Nat. Mater. **6**, 21 (2007).
[6] I. I. Mazin and D. J. Singh, Phys. Rev. B **56**, 2556 (1997).
[7] G. Koster, L. Klein, W. Siemons, G. Rijnders, J. S. Dodge, C. B. Eom, D. H. A. Blank, and M. R. Beasley, Rev. Mod. Phys. **84**, 253 (2012).
[8] J. J. Randall and R. Ward, J. Am. Chem. Soc. **81**, 2629 (1958).
[9] H. N. Lee, H. M. Christen, M. F. Chisholm, C. M. Rouleau, and D. H. Lowndes, Nature (London) **433**, 395 (2005).
[10] L. W. Martin, Y.-H. Chu, Q. Zhan, R. Ramesh, S.-J. Han, S. X. Wang, M. Warusawithana, and D. G. Schlom, Appl. Phys. Lett. **91**, 172513 (2007).
[11] M. Ziese, I. Vrejoiu, E. Pippel, P. Esquinazi, D. Hesse, C. Etz, J. Henk, A. Ernst, I. V. Maznichenko, W. Hergert, and I. Mertig, Phys. Rev. Lett. **104**, 167203 (2010).
[12] M. Verissimo-Alves, P. García-Fernández, D. I. Bilc, P. Ghosez, and J. Junquera, Phys. Rev. Lett. **108**, 107003 (2012).
[13] M. Q. Gu, Q. Y. Xie, X. Shen, R. B. Xie, J. L. Wang, G. Tang, D. Wu, G. P. Zhang, and X. S. Wu, Phys. Rev. Lett. **109**, 157003 (2012).
[14] S. J. Callori, J. Gabel, D. Su, J. Sinsheimer, M. V. Fernandez-Serra, and M. Dawber, Phys. Rev. Lett. **109**, 067601 (2012).
[15] W. P. Zhou, Q. Li, Y. Q. Xiong, Q. M. Zhang, D. H. Wang, Q. Q. Cao, L. Y. Lv, and Y. W. Du, Sci. Rep. **4**, 6991 (2014).
[16] X. H. Liu, J. D. Burton, M. Ye. Zhuravlev, and E. Y. Tsymbal, Phys. Rev. Lett. **114**, 046601 (2015).
[17] S. Z. Wu, J. Miao, X. G. Xu, W. Yan, R. Reeve, X. H. Zhang, and Y. Jiang, Sci. Rep. **5**, 8905 (2015).
[18] D. E. Shai, C. Adamo, D. W. Shen, C. M. Brooks, J. W. Harter, E. J. Monkman, B. Burganov, D. G. Schlom, and K. M. Shen, Phys. Rev. Lett. **110**, 087004 (2013).
[19] Y. J. Chang, C. H. Kim, S.-H. Phark, Y. S. Kim, J. Yu, and T. W. Noh, Phys. Rev. Lett. **103**, 057201 (2009).
[20] Luca de' Medici, J. Mravlje, and A. Georges, Phys. Rev. Lett. **107**, 256401 (2011).
[21] D. W. Jeong, H. C. Choi, C. H. Kim, S. H. Chang, C. H. Sohn, H. J. Park, T. D. Kang, D.-Y. Cho, S. H. Baek, C. B. Eom, J. H. Shim, J. Yu, K. W. Kim, S. J. Moon, and T. W. Noh, Phys. Rev. Lett. **110**, 247202 (2013).
[22] H. T. Dang, J. Mravlje, A. Georges, and A. J. Millis, Phys. Rev. B **91**, 195149 (2015).
[23] A. P. Mackenzie and Y. Maeno, Rev. Mod. Phys. **75**, 657 (2003).
[24] S. A. Grigera, R. S. Perry, A. J. Schofield, M. Chiao, S. R. Julian, G. G. Lonzarich, S. I. Ikeda, Y. Maeno, A. J. Millis, and A. P. Mackenzie, Science **294**, 329 (2001).
[25] Y. Aiura, Y. Yoshida, I. Hase, S. I. Ikeda, M. Higashiguchi, X. Y. Cui, K. Shimada, H. Namatame, M. Taniguchi, and H. Bando, Phys. Rev. Lett. **93**, 117005 (2004).
[26] S. Aizaki, T. Yoshida, K. Yoshimatsu, M. Takizawa, M. Minohara, S. Ideta, A. Fujimori, K. Gupta, P. Mahadevan, K. Horiba, H. Kumigashira, and M. Oshima, Phys. Rev. Lett. **109**, 056401 (2012).
[27] Z. Sun, Y.-D. Chuang, A. V. Fedorov, J. F. Douglas, D. Reznik, F. Weber, N. Aliouane, D. N. Argyriou, H. Zheng, J. F. Mitchell, T. Kimura, Y. Tokura, A. Revcolevschi, and D. S. Dessau, Phys. Rev. Lett. **97**, 056401 (2006).
[28] A. Lanzara, P. V. Bogdanov, X. J. Zhou, S. A. Kellar, D. L. Feng, E. D. Lu, T. Yoshida, H. Eisaki, A. Fujimori, K. Kishio, J.-I. Shimoyama, T. Noda, S. Uchida, Z. Hussain, and Z.-X. Shen, Nature (London) **412**, 510 (2001).
[29] X. J. Zhou, T. Yoshida, A. Lanzara, P. V. Bogdanov, S. A. Kellar, K. M. Shen, W. L. Yang, F. Ronning, T. Sasagawa, T. Kakeshita, T. Noda, H. Eisaki, S. Uchida, C. T. Lin, F. Zhou, J. W. Xiong, W. X. Ti, Z. X. Zhao, A. Fujimori, Z. Hussain, and Z.-X. Shen, Nature (London) **423**, 398 (2003).
[30] C. M. Brooks, L. F. Kourkoutis, T. Heeg, J. Schubert, D. A. Muller, and D. G. Schlom, Appl. Phys. Lett. **94**, 162905 (2009).

[31] D. Pesquera, X. Marti, V. Holy, R. Bachelet, G. Herranz, and J. Fontcuberta, Appl. Phys. Lett. **99**, 221901 (2011).

[32] K. Byczuk, M. Kollar, K. Held, Y.-F. Yang, I. A. Nekrasov, Th. Pruschke, and D. Vollhardt, Nat. Phys. **3**, 168 (2007).

[33] T. Cuk, D. H. Lu, X. J. Zhou, Z.-X. Shen, T. P. Devereaux, and N. Nagaosa, Phys. Status Solidi B **242**, 11 (2005).

[34] M. H. Liu, C. Z. Chang, Z. C. Zhang, Y. Zhang, W. Ruan, K. He, L. L. Wang, X. Chen, J. F. Jia, S. C. Zhang, Q. K. Xue, X. C. Ma, and Y. Y. Wang, Phys. Rev. B **83**, 165440 (2011).

[35] K. Held, R. Peters, and A. Toschi, Phys. Rev. Lett. **110**, 246402 (2013).

[36] M. N. Iliev, A. P. Litvinchuk, H.-G. Lee, C. L. Chen, M. L. Dezaneti, C. W. Chu, V. G. Ivanov, M. V. Abrashev, and V. N. Popov, Phys. Rev. B **59**, 364 (1999).

Comparative angle-resolved photoemission spectroscopy study of $CaRuO_3$ and $SrRuO_3$ thin films: Pronounced spectral weight transfer and possible precursor of lower Hubbard band

H. F. Yang,[1,2] C. C. Fan,[1,2] Z. T. Liu,[1,2] Q. Yao,[1,3] M. Y. Li,[1,2] J. S. Liu,[1,2] M. H. Jiang,[1] and D. W. Shen[1,2,*]

[1]*State Key Laboratory of Functional Materials for Informatics, Shanghai Institute of Microsystem and Information Technology (SIMIT), Chinese Academy of Sciences, Shanghai 200050, China*

[2]*CAS-Shanghai Science Research Center, Shanghai 201203, China*

[3]*State Key Laboratory of Surface Physics, Department of Physics, and Advanced Materials Laboratory, Fudan University, Shanghai 200433, China*

(Received 20 May 2016; revised manuscript received 29 July 2016; published 23 September 2016)

In the prototypical 4*d* system (Sr,Ca)RuO_3, the degree and origin of electron correlations, and how they correlate with physical properties, still remain elusive, though extensive studies have been performed. In this work we present a comparative electronic structure study of high-quality epitaxial $CaRuO_3$ and $SrRuO_3$ thin films, by means of reactive molecular beam epitaxy and *in situ* angle-resolved photoemission spectroscopy. We found that while $SrRuO_3$ possesses sharp features signaling the Fermi liquid state, the isostructural $CaRuO_3$ exhibits broad features and its spectral weight is markedly transferred from the Fermi level to −1.2 eV forming a "hump" structure which resembles the Mott-Hubbard system (Sr,Ca)VO_3. We suggest that this hump is the precursor of the lower Hubbard band, and the U/W (U and W represent the on-site Coulomb interactions and bandwidth, respectively) of our $CaRuO_3$ thin film is much larger than that of $SrRuO_3$. In addition, we discuss the origin of electron correlations as well as the ferromagnetism in $SrRuO_3$ which is absent in $CaRuO_3$. Our findings put constraints on future studies, and also show that perovskite ruthenates are indeed an experimentally tunable system for the study of electron correlations.

DOI: 10.1103/PhysRevB.94.115151

I. INTRODUCTION

The physics of electron correlations is one of the most fundamental topics in the study of transition metal oxides, since it essentially lays the foundation for versatile extraordinary physical phenomena including high-T_c superconductivity [1,2], metal-insulator transitions [3], and colossal magnetoresistance [4], etc.

The celebrated single-band Hubbard model addresses the role of on-site Coulomb interaction U of electrons. The Mott-Hubbard transition illustrates that when the U is large enough to be comparable with the bandwidth W, the half-filled band will be split into the upper and lower Hubbard bands separated by a considerable band gap, and the system will be driven into the Mott insulating state [3,5]. Such a well-known example is the $3d^1$ electron system (Sr,Ca)VO_3. Although this system would not reach the real insulating state through continuous Ca substitution, the pronounced spectral weight transfer from the Fermi level (E_F) towards high binding energy region and the resulted lower Hubbard band located at around −1.6 eV have been directly observed by photoemission studies [6–8]. When going from 3*d* to 4*d* electron systems, U would usually decrease since 4*d* electrons are expected to be more delocalized than 3*d* ones, while the spin-orbit coupling (SOC) would become stronger due to the heavier elements.

Among various 4*d* transition metal oxides, perovskite ruthenium (Ru) oxides $CaRuO_3$ (CRO) and $SrRuO_3$ (SRO) have aroused plenty of interest, since they not only serve as key building bricks in all-oxide electronics and spintronics but also can provide rich implications for fundamental physics [9]. In these compounds, Ru^{4+} has a $4d^4$ configuration with four electrons occupying three degenerate t_{2g} orbitals. Despite their similar crystal structure, while SRO is a metallic ferromagnet with a T_c of 160 K and exhibits the Fermi-liquid (FL) state at low temperatures [9,10], CRO remains metallic with the absence of long-range magnetic orderings and does not exhibit FL behaviors until 1.5 K [11–13]. So far, electron correlations have been proposed to account for such striking differences [9,14,15]. However, controversies on the extent of electron correlations and how they determine the physical properties still exist, despite a magnitude of theoretical [15–21] and experimental attempts [10,22–31]. Additionally, the origin of electron correlations in this system remains an open question. Besides the common Coulomb repulsion (Mott physics), the Hund's coupling [16,32,33] and SOC [34] were also proposed to play an important role.

In order to study electron correlations in CRO and SRO, directly detecting their electronic structures is highly desirable. However, the difficulty to cleave the pseudocubic (Sr,Ca)RuO_3 highly hinders the visualization of their band structures by means of experimental probes like scanning tunneling spectroscopy (STS) and angle-resolved photoemission spectroscopy (ARPES). To the best of our knowledge, the measured band structure of CRO has not been reported before. And thus, a comparable picture of low-lying electronic structures of CRO and SRO is still lacking to date.

In this article we took advantage of reactive molecular beam epitaxy (MBE) and *in situ* ARPES [10,35,36] to investigate the band structures of CRO and SRO in a comparative way. We found that, while SRO exhibits sharp spectra formed by evident quasiparticles near E_F signaling the FL state, the photoemission spectra of CRO show broad and blurry features in the vicinity of E_F and a pronounced "hump" structure centered at −1.2 eV which we suggest is the precursor of the lower Hubbard band.

*dwshen@mail.sim.ac.cn

 ©2016 American Physical Society

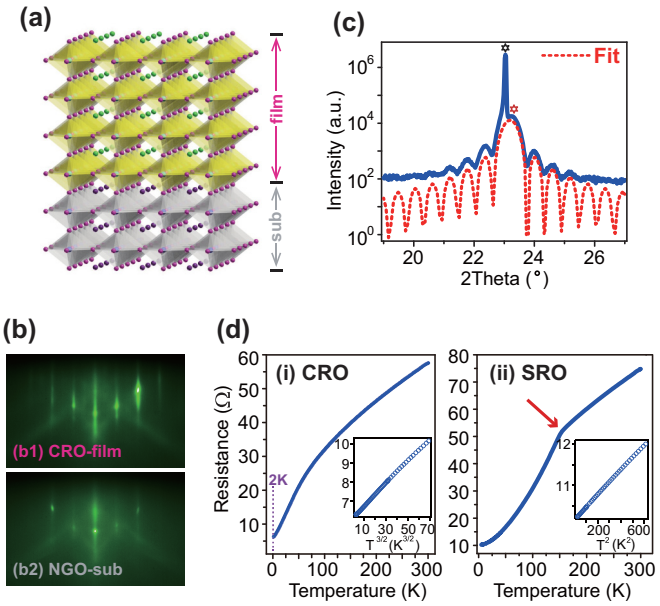

FIG. 1. Growth and characterization of CRO thin films. (a) Schematic of CRO thin films epitaxially grown on NGO substrates. (b) Typical RHEED patterns of CRO thin film (b1) and the NGO substrate (b2) along the $(100)_p$ azimuthal. Sharp diffraction spot-streak structures and visible Kikuchi lines in the CRO RHEED pattern indicate its high quality with long-range ordered surface structure. (c) X-ray diffraction pattern around $(001)_p$ peak for a CRO thin film. The red and black markers denote $(001)_p$ peaks of the CRO thin film and the NGO substrate, respectively. The red dotted line is the good fitting curve which gives a thickness of 41 unit cells (UCs) and out-of-plane constant of 3.832 Å as a result of the tensile strain. (d) Temperature dependence of the resistances of this 41-UC-thick CRO film (i) and 21-UC-thick SRO film (ii). In (i), no signature of a phase transition in our CRO film was observed within the temperature range of our measurement; the inset shows that the low-temperature resistance has a linear dependence of $T^{3/2}$ (T is short for temperature). In (ii), the red arrow marks the kink corresponding to the ferromagnetic transition of SRO; the inset shows that the low-temperature resistance has a linear dependence of T^2, which indicates the Fermi liquid ground state. The growth details of high-quality SRO thin films with well-controlled thicknesses can be found in our previous work [34].

II. EXPERIMENT

Perovskite $(001)_p$ (where the subscript p denotes pseudocubic indices) CRO films [Fig. 1(a)] were fabricated using a DCA R450 OMBE system at a substrate temperature of 750 °C in a background pressure of 2×10^{-6} Torr of distilled ozone. Ca and Ru were evaporated from an effusion cell and an electron beam evaporator, respectively. To achieve high-quality CRO thin films, $(001)_p$ $NdGaO_3$ (NGO) was used as the substrate to effectively get rid of multidomains [37], which leads to a 0.6% tensile strain for epitaxial films. During growth, *in situ* surface-sensitive reflection high-energy electron diffraction (RHEED) was used to monitor the growth and check surface structure. Growth details of our high-quality SRO thin films can be found in our previous work [35].

After growth, thin films were quickly transferred to the combined ARPES chamber (within 5 min) for measurements through an ultrahigh vacuum buffer chamber ($\sim1.0\times10^{-10}$ Torr). Our in-house ARPES system is equipped with a VG-Scienta R8000 electron analyzer and a SPECS UVLS helium discharging lamp with a monochromator. The data were collected at 15 K with He Iα (21.2 eV) photons under ultrahigh vacuum of 8×10^{-11} Torr. The overall energy and angular resolutions were set to 15 meV and 0.3°, respectively. During the measurements, the films were checked to be stable and no signatures of degradation or charging were observed.

III. RESULTS AND DISCUSSIONS

As displayed in Fig. 1(b1), the RHEED pattern of a typical CRO thin film features shiny diffraction spot-streak structures and visible Kikuchi lines which are comparable to the NGO single-crystalline substrate [Fig. 1(b2)]. These fine structures of RHEED pattern reveal the high quality of films with long-range ordered lattice structure and flat surface, which guarantee the following good ARPES data. Figure 1(c) shows the typical x-ray diffraction (XRD) θ-2θ scan of the CRO film around the $(001)_p$ peak. One can see persistent fringes which indicate the sharp and smooth interface between the thin film and the substrate that again confirms the high quality of thin films. Good fitting to these fringes [see the red dotted line in Fig. 1(c)] gives a thickness of 41 unit cells (UCs) and the out-of-plane constant of 3.832 Å as a result of the tensile strain from the NGO substrate. Characterizations of SRO films have been reported in our previous work [35].

Figure 1(d)(i) displays the temperature dependence of the electrical resistance $[R(T)]$ of this 41-UC-thick CRO film. CRO remains metallic in the whole temperature range (from 2.0 to 300 K), and exhibits a smooth curve without the kinklike feature, suggesting no signature of long-range magnetic ordering as in SRO [9,10]. Moreover, in our measurement range, the low-temperature resistivity obeys a $T^{3/2}$ dependence, implying the non-Fermi-liquid (NFL) state. This behavior as well as the $R(T)$ curve shape, is in accordance with previous reports [11–13]. By contrast, SRO is generally thought to possess the FL ground state [i.e., low-temperature resistance obeys a T^2 dependence; see the inset of Fig. 1(d)(ii)] with a ferromagnetic transition around 155 K signaled by a "kink" (marked by the red arrow) in the $R(T)$ curve [9,10].

To understand these differences between the isostructural CRO and SRO thin films, *in situ* ARPES measurements were carried out to compare their low-lying electronic structures. Figures 2(a) and 2(b) show the representative valence band (VB) spectra of CRO and SRO along the (0, 0)-(0, π) high symmetry direction [see the cut #1 in the inset of Fig. 2(b)] and the corresponding integrated energy dispersive curves (EDCs) [normalization within (−4.2 eV, −3.4 eV) was used to display the near-E_F features clearly], respectively. Evident dispersive bands can be observed, which again confirms the high-quality surface and crystal structures of the thin film. High-energy parts of their band dispersions (from −2.5 to −7.5 eV) look quite similar, as illustrated by their spectra in Fig. 2(a). However, near E_F [cyan shadow region in Fig. 2(b)], a pronounced difference is directly revealed from the integrated EDCs, whereas SRO shows one sharp peak at E_F, CRO exhibits one peak at E_F and an additional

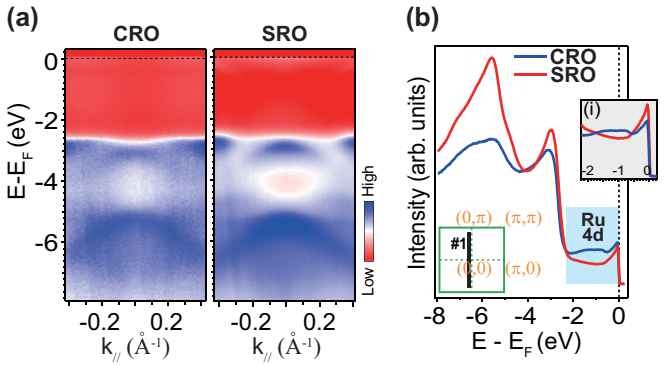

FIG. 2. Valence bands of CRO and SRO. (a) Valence band spectra of CRO and SRO. Their high-binding energy dispersions (below −2.4 eV) are similar. (b) Integrated valence bands of CRO (blue curve) and SRO (red curve). The normalization of these two curves was done within the energy window of [−4.2 eV, −3.4 eV] to clearly show their near-E_F structures. In (i), near-E_F parts were shown with the normalization within the energy window of [−2.2 eV, 0]. The inset is the schematic of the first Brillouin zone (corresponding to the pseudocubic substrate) with the cut #1.

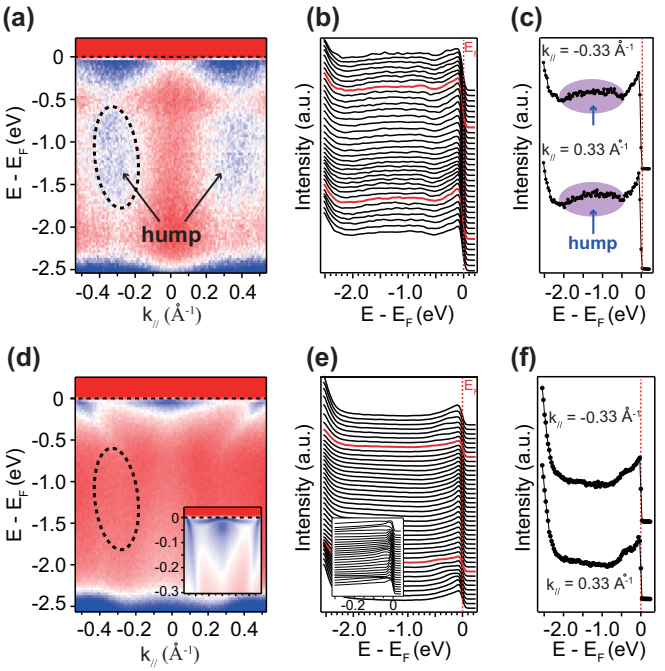

FIG. 3. Side-by-side comparison of representative long-cut dispersions of CRO and SRO along the cut #1. (a) Long-cut spectrum (down to −2.5 eV) of CRO. The hump structure enclosed by black dotted line is evidently shown to be located around −1.2 eV. (b) EDCs of the spectrum (a) exhibiting broad peaks. (c) Two representative EDCs cutting across the hump structure marked by the purple shadow. (d) Long-cut spectrum of SRO. No hump structure is observed [no evident spectral weight in the same black-dotted-line region as (a)]. The inset shows sharp band dispersions near E_F. (e) EDCs of the spectrum (d), exhibiting sharp peaks. The inset shows EDCs near E_F. (f) Two representative EDCs at the same positions as (c) showing no signatures of hump in SRO.

hump structure centered at −1.2 eV. These differences are also shown in the zoom-in plot [Fig. 2(b)(i)], in which the normalization within (−2.2 eV, 0) was used. Note that bands in this region mainly originate from Ru 4*d* electrons. It is worth noting that spectra backgrounds of CRO and SRO can be intrinsically different, and generally a high-binding-energy region has a higher background than the near-E_F region within one spectrum.

Then we investigated the band dispersions of CRO and SRO in the vicinity of E_F, as directly compared in Fig. 3. While SRO shows sharp band dispersions built by evident quasiparticles around E_F [10,35] [insets of Figs. 3(d) and 3(e)], CRO displays blurry and broad features which reveals that electrons (quasiparticles) have quite short lifetimes [Figs. 3(a) and 3(b)]. This finding indicates the NFL state of CRO and FL state of SRO at our measurement temperature (15 K), which is in line with bulk-sensitive transport studies discussed above. Moreover, in contrast to SRO, CRO possesses appreciable spectral weight around −1.2 eV forming an ellipsoid-shaped band [Fig. 3(a)]. This additional feature contributes to the pronounced hump structure, which is as also confirmed by the side-by-side comparison of individual EDCs [Figs. 3(c) and 3(f)].

What's the origin of the hump feature discovered in CRO thin film? Since this hump resides at relatively high binding energy region (more than 1.0 eV below E_F), low-energy excitations which may exist in this system (e.g., phonons [35], polarons [38], and magnons [2]) should not be attributed to. If we compare the renormalized integrated EDCs of CRO and SRO [Fig. 4(a)], we can conjecture that part of spectral weight of the quasiparticle peak near E_F should have shifted to −1.2 eV and formed the hump structure in CRO. This is naturally reminiscent of the well-established example—Sr(Ca)VO_3 system with a simple $3d^1$ configuration [3]. As displayed in Fig. 4(b)(i), $SrVO_3$ shows a coherent peak at E_F and a broad feature centered at −1.6 eV ascribed to the lower Hubbard band; when going from $SrVO_3$ to $CaVO_3$, the effective Coulomb interaction increases and consequently more spectral weight transfers from the coherent peak to the lower Hubbard band at higher binding energy [6–8]. Such behavior was also observed in some other typical Mott-Hubbard systems, such as V_2O_3 [39] and $NiS_{2-x}Se_x$ [40]. Theoretically, Mott-Hubbard spectral weight transferring has been studied in the context of the dynamical mean field theory (DMFT) solution of the Hubbard model [41,42]. As schematically shown in Fig. 4(b)(ii), as increasing Coulomb interactions between electrons, spectral features evolve from sharp peak at E_F [electrons are entirely independent which is characteristic of a "good" metal (see the curve *a*)] to the vanishing of the quasiparticle peak and the formation of incoherent lower Hubbard band [electrons hugely interact with each other which is characteristic of Mott insulator (see the curve *f*)]; in the mediate region, the spectrum features a quasiparticle peak near E_F and a broad hump which is the precursor of the lower Hubbard band.

Likewise, the spectral weight transferring of CRO could be understood in the similar Mott physics picture, and the hump of CRO can be ascribed to the lower Hubbard band. Actually, its cousin compound Ca_2RuO_4 is a well-studied Mott insulator [43,44], and doping SRO showed similar spectral weight transfer which was interpreted to be related

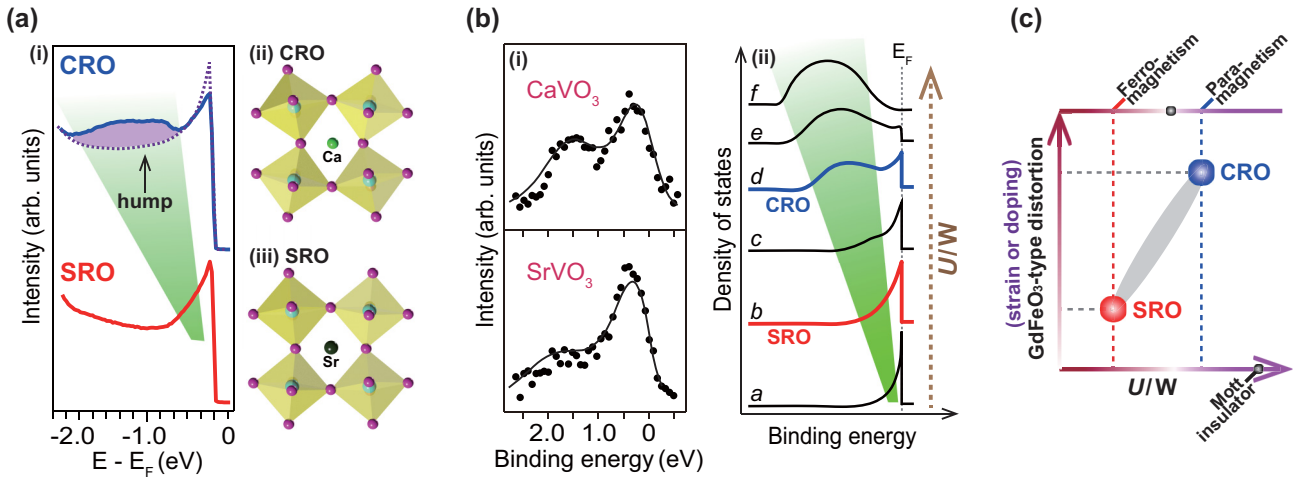

FIG. 4. (a) Integrated EDCs of CRO (blue curve) and SRO (red curve) (i), and schematic of CRO (ii) showing a bigger $GdFeO_3$-type distortion than SRO (iii). (b) Pronounced spectral weight transfer in Mott-Hubbard system Sr(Ca)VO_3, which is reproduced from Ref. [7] (i). Schematic of spectral weight transfer with increasing the U/W in a typical Mott-Hubbard system (from the DMFT solution of the Hubbard model; Refs. [41,42]) (ii). (c) Simple phase diagram of CRO and SRO. The y axis and the bottom and top x axes are the $GdFeO_3$-type distortion and the U/W and magnetism, respectively. Ruthenium perovskites are indeed a tunable system to explore the electron correlations and related quantum criticality, with structural distortion as the knob (can be experimentally modified via epitaxial strain and doping).

with correlation effects [24,25]. Therefore, it is reasonable to demonstrate that the Mott physics plays an important role in the formation of the hump in CRO, and CRO shows a larger U/W than SRO [see Fig. 4(b)(ii)]. From the perspective of structural distortion, smaller size of Ca^{2+} than Sr^{2+} leads to bigger $GdFeO_3$-type distortion in CRO [Fig. 4(a)], and further suppresses the hopping of electrons (decreases the bandwidth W), and thus increases the effective Coulomb interactions [14,15,31,33].

Since C(S)RO are 4d non-half-filled multiband compounds, besides Mott physics, some other scenarios were proposed to play a role in electron correlations. On one hand, recently initiated by the studies of iron-based superconductors [45,46], Hund's rule coupling (intra-atomic exchange J) was proposed to play a key role in determining the electron correlations from two aspects: it drives the system away from the Mott transition and decreases the possible Mott gap; meanwhile, it makes the metallic state more correlated by strongly suppressing the quasiparticle coherence scale [16,32]. Considering the multiband nature and highly suppressed coherence temperature of CRO, it may also contribute to the electron correlations [16,33]. On the other hand, SOC was also involved into the strongly correlated physics (e.g., spin-orbit Mott insulator): the split bands by SOC are so narrow that a small on-site Coulomb interaction U may introduce a relatively large U/W which drives the system into the Mott insulating state [34]. Since Ru possesses a stronger SOC than 3d elements, it is reasonable to take SOC into consideration. However, our photoemission data do not reveal any notable splitting phenomena of bands near E_F of C(S)RO, which is consistent with previous theoretical predictions that SOC would not have a large effect on the electronic structure [14,18].

Except the hump structure, another pronounced difference in the band structures of CRO and SRO is the flat band around the BZ center of SRO which is absent in CRO. These bands contribute to large density of states, which together with the FL ground state, may account for the itinerant ferromagnetism of SRO [17,47]. Note that local moment may also play a role [10,21], regarding the Hund's coupling in the non-half-filled shells. Although CRO does not show any long-range magnetic ordering (in our thin film case and bulk studies reported [11,12]), it was suggested to be located in the vicinity of magnetic ordering region [12,17]. Recently, ferromagnetic CRO thin film was reported by applying considerable tensile strain [48] possibly due to modifying structural distortion. Meanwhile, strain was also suggested to change the Curie temperature of SRO [49].

Figure 4(d) displays a simple phase diagram of ruthenium perovskites. The y axis and top and bottom x axes represent the $GdFeO_3$-type distortion and magnetism and the U/W, respectively. With the increase of the $GdFeO_3$-type distortion, the system can evolve from a ferromagnet (bulk SRO) with FL ground state and small effective Coulomb interaction, to a nonmagnet (bulk CRO) with NFL ground state and big effective Coulomb interaction. Thus, a quantum critical point is expected in the mediate region, and the $GdFeO_3$-type distortion can be used as an essential knob. This distortion can be experimentally tuned via epitaxial strain [10,48,49] and chemical doping [24,25,50–52]. Therefore, ruthenium perovskites are indeed a profound system to study the electron correlations and relevant quantum criticality.

IV. CONCLUSION

To summarize, comparative *in situ* ARPES studies of high-quality CRO and SRO thin films were presented. In contrast to SRO possessing sharp features at the Fermi level, CRO exhibits broad features and the spectral weight is substantially transferred from E_F to around -1.2 eV forming a hump

structure which we suggest is the precursor of lower Hubbard band. We show that the U/W of CRO thin films on NGO is bigger than that of SRO. Discussions about the possible origins of the electron correlations and magnetism are also presented. Our results suggest that ruthenium perovskites are indeed a tunable system to study the electron correlations and quantum criticality therein. Further studies from both theoretical and experimental aspects are highly advocated, and our results could be a good start point.

ACKNOWLEDGMENTS

We gratefully acknowledge the discussions with Professor D. J. Singh. This work is supported by the National Key R&D Program of the MOST of China (Grant No. 2016YFA0300204) and the National Science Foundation of China (Grants No. 11274332, No. 11574337, and No. 11227902). D.W.S. is also supported by the "Strategic Priority Research Program (B)" of the Chinese Academy of Sciences (Grant No. XDB04040300) and the "Youth Innovation Promotion Association CAS."

[1] P. A. Lee, N. Nagaosa, and X.-G. Wen, Rev. Mod. Phys. **78**, 17 (2006).
[2] A. Damascelli, Z. Hussain, and Z.-X. Shen, Rev. Mod. Phys. **75**, 473 (2003).
[3] M. Imada, A. Fujimori, and Y. Tokura, Rev. Mod. Phys. **70**, 1039 (1998).
[4] M. B. Salamon and M. Jaime, Rev. Mod. Phys. **73**, 583 (2001).
[5] P. W. Anderson, Phys. Rev. **115**, 2 (1959).
[6] I. H. Inoue, I. Hase, Y. Aiura, A. Fujimori, Y. Haruyama, T. Maruyama, and Y. Nishihara, Phys. Rev. Lett. **74**, 2539 (1995).
[7] K. Maiti, D. D. Sarma, M. J. Rozenberg, I. H. Inoue, H. Makino, O. Goto, M. Pedio, and R. Cimino, Europhys. Lett. **55**, 246 (2001).
[8] K. Maiti, U. Manju, S. Ray, P. Mahadevan, I. H. Inoue, C. Carbone, and D. D. Sarma, Phys. Rev. B **73**, 052508 (2006).
[9] G. Koster, L. Klein, W. Siemons, G. Rijnders, J. S. Dodge, C. B. Eom, D. H. A. Blank, and M. R. Beasley, Rev. Mod. Phys. **84**, 253 (2012).
[10] D. E. Shai, C. Adamo, D. W. Shen, C. M. Brooks, J. W. Harter, E. J. Monkman, B. Burganov, D. G. Schlom, and K. M. Shen, Phys. Rev. Lett. **110**, 087004 (2013).
[11] L. Klein, L. Antognazza, T. H. Geballe, M. R. Beasley, and A. Kapitulnik, Phys. Rev. B **60**, 1448 (1999).
[12] G. Cao, O. Korneta, S. Chikara, L. E. Delong, and P. Schlottmann, Solid State Commun. **148**, 305 (2008).
[13] M. Schneider, D. Geiger, S. Esser, U. S. Pracht, C. Stingl, Y. Tokiwa, V. Moshnyaga, I. Sheikin, J. Mravlje, M. Scheffler, and P. Gegenwart, Phys. Rev. Lett. **112**, 206403 (2014).
[14] S. Middey, P. Mahadevan, and D. D. Sarma, Phys. Rev. B **83**, 014416 (2011).
[15] E. Jakobi, S. Kanungo, S. Sarkar, S. Schmitt, and T. Saha-Dasgupta, Phys. Rev. B **83**, 041103(R) (2011).
[16] L. de' Medici, J. Mravlje, and A. Georges, Phys. Rev. Lett. **107**, 256401 (2011).
[17] I. I. Mazin and D. J. Singh, Phys. Rev. B **56**, 2556 (1997).
[18] J. M. Rondinelli, N. M. Caffrey, S. Sanvito, and N. A. Spaldin, Phys. Rev. B **78**, 155107 (2008).
[19] H. Hadipour and M. Akhavan, Eur. Phys. J. B **84**, 203 (2011).
[20] G. T. Wang, M. P. Zhang, Z. X. Yang, and Z. Fang, J. Phys.: Condens. Matter **21**, 265602 (2009).
[21] M. Kim and B. I. Min, Phys. Rev. B **91**, 205116 (2015).
[22] R. S. Singh, V. R. R. Medicherla, and K. Maiti, Physica B **403**, 1398 (2008).
[23] K. Maiti and R. S. Singh, Phys. Rev. B **71**, 161102(R) (2005).
[24] J. Kim, J.-Y. Kim, B.-G. Park, and S.-J. Oh, Phys. Rev. B **73**, 235109 (2006).
[25] W. Siemons, G. Koster, A. Vailionis, H. Yamamoto, D. H. A. Blank, and M. R. Beasley, Phys. Rev. B **76**, 075126 (2007).
[26] J. Okamoto, T. Mizokawa, A. Fujimori, I. Hase, M. Nohara, H. Takagi, Y. Takeda, and M. Takano, Phys. Rev. B **60**, 2281 (1999).
[27] J. Park, S. J. Oh, J. H. Park, D. M. Kim, and C. B. Eom, Phys. Rev. B **69**, 085108 (2004).
[28] S. Grebinskij, S. Masys, S. Mickevicius, V. Lisauskas, and V. Jonauskas, Phys. Rev. B **87**, 035106 (2013).
[29] K. Maiti, R. S. Singh, and V. R. R. Medicherla, Europhys. Lett. **78**, 17002 (2007).
[30] D. W. Jeong, H. C. Choi, C. H. Kim, S. H. Chang, C. H. Sohn, H. J. Park, T. D. Kang, D.-Y. Cho, S. H. Baek, C. B. Eom, J. H. Shim, J. Yu, K. W. Kim, S. J. Moon, and T. W. Noh, Phys. Rev. Lett. **110**, 247202 (2013).
[31] C.-Q. Jin, J.-S. Zhou, J. B. Goodenough, Q. Q. Liu, J. G. Zhao, L. X. Yang, Y. Yu, R. C. Yu, T. Katsura, A. Shatskiy, and E. Ito, Proc. Natl. Acad. Sci. USA **105**, 7115 (2008).
[32] A. Georges, Luca de' Medici, and J. Mravlje, Annu. Rev. Condens. Matter Phys. **4**, 137 (2013).
[33] H. T. Dang, J. Mravlje, A. Georges, and A. J. Millis, Phys. Rev. B **91**, 195149 (2015).
[34] B. J. Kim, H. Jin, S. J. Moon, J.-Y. Kim, B.-G. Park, C. S. Leem, J. Yu, T. W. Noh, C. Kim, S.-J. Oh, J.-H. Park, V. Durairaj, G. Cao, and E. Rotenberg, Phys. Rev. Lett. **101**, 076402 (2008).
[35] H. F. Yang, Z. T. Liu, C. C. Fan, Q. Yao, P. Xiang, K. L. Zhang, M. Y. Li, H. Li, J. S. Liu, D. W. Shen, and M. H. Jiang, Phys. Rev. B **93**, 121102(R) (2016).
[36] M. Y. Li, Z. T. Liu, H. F. Yang, J. L. Zhao, Q. Yao, C. C. Fan, J. S. Liu, B. Gao, D. W. Shen, and X. M. Xie, Chin. Phys. Lett. **32**, 057402 (2015).
[37] D. L. Proffit, H. W. Jang, S. Lee, C. T. Nelson, X. Q. Pan, M. S. Rzchowski, and C. B. Eom, Appl. Phys. Lett. **93**, 111912 (2008).
[38] C. Y. Chen, J. Avila, E. Frantzeskakis, A. Levy, and M. C. Asensio, Nat. Commun. **6**, 8585 (2015).
[39] S.-K. Mo, J. D. Denlinger, H.-D. Kim, J.-H. Park, J. W. Allen, A. Sekiyama, A. Yamasaki, K. Kadono, S. Suga, Y. Saitoh, T. Muro, P. Metcalf, G. Keller, K. Held, V. Eyert, V. I. Anisimov, and D. Vollhardt, Phys. Rev. Lett. **90**, 186403 (2003).
[40] H. C. Xu, Y. Zhang, M. Xu, R. Peng, X. P. Shen, V. N. Strocov, M. Shi, M. Kobayashi, T. Schmitt, B. P. Xie, and D. L. Feng, Phys. Rev. Lett. **112**, 087603 (2014).
[41] A. Georges, G. Kotliar, W. Krauth, and M. J. Rozenberg, Rev. Mod. Phys. **68**, 13 (1996).

[42] G. Kotliar and D. Vollhardt, Phys. Today **57**, 53 (2004).
[43] E. Gorelov, M. Karolak, T. O. Wehling, F. Lechermann, A. I. Lichtenstein, and E. Pavarini, Phys. Rev. Lett. **104**, 226401 (2010).
[44] M. Neupane, P. Richard, Z.-H. Pan, Y. M. Xu, R. Jin, D. Mandrus, X. Dai, Z. Fang, Z. Wang, and H. Ding, Phys. Rev. Lett. **103**, 097001 (2009).
[45] K. Haule and G. Kotliar, New J. Phys. **11**, 025021 (2009).
[46] Z. P. Yin, K. Haule, and G. Kotliar, Nat. Mater. **10**, 932 (2011).
[47] D. J. Singh, J. Appl. Phys. **79**, 4818 (1996).
[48] S. Tripathi, R. Rana, S. Kumar, P. Pandey, R. S. Singh, and D. S. Rana, Sci. Rep. **4**, 3877 (2014).
[49] A. T. Zayak, X. Huang, J. B. Neaton, and K. M. Rabe, Phys. Rev. B **77**, 214410 (2008).
[50] G. Cao, S. McCall, M. Shepard, J. E. Crow, and R. P. Guertin, Phys. Rev. B **56**, 321 (1997).
[51] Z. Fang, N. Nagaosa, K. S. Takahashi, A. Asamitsu, R. Mathieu, T. Ogasawara, H. Yamada, M. Kawasaki, Y. Tokura, and K. Terakura, Science **302**, 92 (2003).
[52] K. Yoshimura, T. Imai, T. Kiyama, K. R. Thurber, A. W. Hunt, and K. Kosuge, Phys. Rev. Lett. **83**, 4397 (1999).

Charge Transfer Effects in Naturally Occurring van der Waals Heterostructures $(PbSe)_{1.16}(TiSe_2)_m$ ($m = 1, 2$)

Q. Yao,[1,2,3] D. W. Shen,[2,4,*] C. H. P. Wen,[1,3] C. Q. Hua,[5] L. Q. Zhang,[3,6] N. Z. Wang,[7] X. H. Niu,[1,3] Q. Y. Chen,[1,3] P. Dudin,[8] Y. H. Lu,[9] Y. Zheng,[5] X. H. Chen,[3,7,10] X. G. Wan,[3,6] and D. L. Feng[1,3]

[1]*State Key Laboratory of Surface Physics, Department of Physics, and Laboratory of Advanced Materials, Fudan University, Shanghai 200433, China*

[2]*State Key Laboratory of Functional Materials for Informatics, Shanghai Institute of Microsystem and Information Technology (SIMIT), Chinese Academy of Sciences, Shanghai 200050, China*

[3]*Collaborative Innovation Centre of Advanced Microstructures, Nanjing 210093, China*

[4]*CAS Center for Excellence in Superconducting Electronics (CENSE), Shanghai 200050, China*

[5]*Department of Physics, Zhejiang University, Hangzhou 310027, China*

[6]*National Laboratory of Solid State Microstructures, College of Physics, Nanjing University, Nanjing 210093, China*

[7]*Hefei National Laboratory for Physical Sciences at Microscale and Department of Physics and Key Laboratory of Strongly-coupled Quantum Matter Physics, University of Science and Technology of China, Hefei 230026, China*

[8]*Diamond Light Source, Harwell Science and Innovation Campus, Didcot OX11 0DE, United Kingdom*

[9]*State Key Lab of Silicon Materials, Zhejiang University, Hangzhou 310027, China*

[10]*High Magnetic Field Laboratory, Chinese Academy of Sciences, Hefei 230031, China*

(Received 5 November 2017; published 7 March 2018)

van der Waals heterostructures (VDWHs) exhibit rich properties and thus has potential for applications, and charge transfer between different layers in a heterostructure often dominates its properties and device performance. It is thus critical to reveal and understand the charge transfer effects in VDWHs, for which electronic structure measurements have proven to be effective. Using angle-resolved photoemission spectroscopy, we studied the electronic structures of $(PbSe)_{1.16}(TiSe_2)_m$ ($m = 1, 2$), which are naturally occurring VDWHs, and discovered several striking charge transfer effects. When the thickness of the $TiSe_2$ layers is halved from $m = 2$ to $m = 1$, the amount of charge transferred increases unexpectedly by more than 250%. This is accompanied by a dramatic drop in the electron-phonon interaction strength far beyond the prediction by first-principles calculations and, consequently, superconductivity only exists in the $m = 2$ compound with strong electron-phonon interaction, albeit with lower carrier density. Furthermore, we found that the amount of charge transferred in both compounds is nearly halved when warmed from below 10 K to room temperature, due to the different thermal expansion coefficients of the constituent layers of these misfit compounds. These unprecedentedly large charge transfer effects might widely exist in VDWHs composed of metal-semiconductor contacts; thus, our results provide important insights for further understanding and applications of VDWHs.

DOI: 10.1103/PhysRevLett.120.106401

Boosted by then enormous effort put into graphenelike materials, research into artificial materials formed by stacking different two-dimensional (2D) crystals in a desired sequence, the so-called van der Waals heterostructures (VDWHs) have gradually drawn considerable attention [1–6]. The interaction between neighboring 2D crystals is relatively weak, but owing to the atomically flat interfaces and precise crystallographic alignment, electronic orbitals can still protrude across the interfaces and thus affect charge carriers in the adjacent 2D crystals. The resulting charge reconstruction leads to emergent properties distinct from those of its individual components, e.g., the observation of Hofstadter's butterfly [7,8], the fractal quantum hall effect [9,10], and the unconventional diode and photovoltaic effects in MoS_2/WSe_2 heterostructures [11], which naturally pique both fundamental and technological interest. However, the deterministic placement methods for preparing most artificial VDWHs impede the experimental investigation of the influence of charge transfer on their low-energy electronic structure, which is the key to understanding the underlying mechanism and of important directive significance to further devices based on VDWHs.

Misfit compounds, bulk materials that consist of alternately stacked rock-salt and transition metal chalcogenide layers, belong to naturally occurring VDWHs [12–16]. The neighboring structural subsystems exhibit different symmetry and periodicity, leading to an incommensurate crystal structure bound by weak van der Waals interactions between interleaved layers, as sketched in Fig. 1(a) [17].

 © 2018 American Physical Society

These compounds provide a unique opportunity to investigate the manipulation of VDWHs, and in particular the cleavable crystal structure and absence of unwanted interlayer adsorbates enable the direct probing of their intrinsic electronic structure by angle-resolved photoemission spectroscopy (ARPES).

In this Letter, through systematic ARPES measurements and first-principles calculations on the low-lying electronic structure of typical naturally occurring VDWHs $(PbSe)_{1.16}(TiSe_2)_m$ $(m = 1, 2)$ (denoted as $m1$ and $m2$ hereinafter), we demonstrate remarkable charge transfer effects that may prove endemic to VDWHs. First, varying the thickness of $TiSe_2$ layers from $m2$ to $m1$ results in the significant increase in the charge transferred at the interfaces, which is accompanied by a dramatic drop in the electron-phonon coupling (EPC) strength far beyond the prediction by first-principles calculations. Furthermore, an unexpected temperature-dependent band shift is revealed, which introduces an up to 40% decrease in the charge transfer when warmed from 10 K to room temperature. Since a large number of current prototype VDWH devices are made from transition metal chalcogenides, and their design is optimized mainly based on their low-temperature properties, this finding may prove crucial to the further exploration of VDWH applications.

High-quality $(PbSe)_{1.16}(TiSe_2)_m$ $(m = 1, 2)$ single crystals were synthesized by a chemical vapor transport method as described elsewhere [18]. They could be mechanically exfoliated down to few-layer thickness, forming natural and air-stable VDWHs suitable for device applications (see Supplemental Material [19] for details). ARPES measurements were performed at beam line 5–4 of Stanford Synchrotron Radiation Laboratory, beam line I05-ARPES of Diamond Light Source, and beam line 13U of National Synchrotron Radiation Laboratory (NSRL). These beam lines are all equipped with VG-Scienta R4000 electron analyzers. The overall energy resolution was 10–15 meV depending on the photon energy, and the angular resolution was set to 0.3°. All samples were cleaved under a vacuum better than 5×10^{-11} Torr. The details of first-principles calculations can be found in Supplemental Material [19–23].

We first present the photoemission intensity maps of $m1$ [Fig. 1(c)] and $m2$ [Fig. 1(d)] at the Fermi energy E_F. Both full-scale maps show hexagonal symmetry in accord with the lattice of bulk $1T$-$TiSe_2$. According to the crystal structure of misfit compounds, there should be a sizable possibility for the PbSe layer to be present on the surface. However, neither map shows any fourfold symmetric feature from the PbSe layers in all of our more than a dozen samples. We speculate that the random or incommensurate potential may affect PbSe severely and localize its holes, and its photoemission signal is thus smeared in momentum space.

Both Fermi surface maps exhibit elliptical Fermi pockets around the M point similar to bulk $1T$-$TiSe_2$ [24], but a

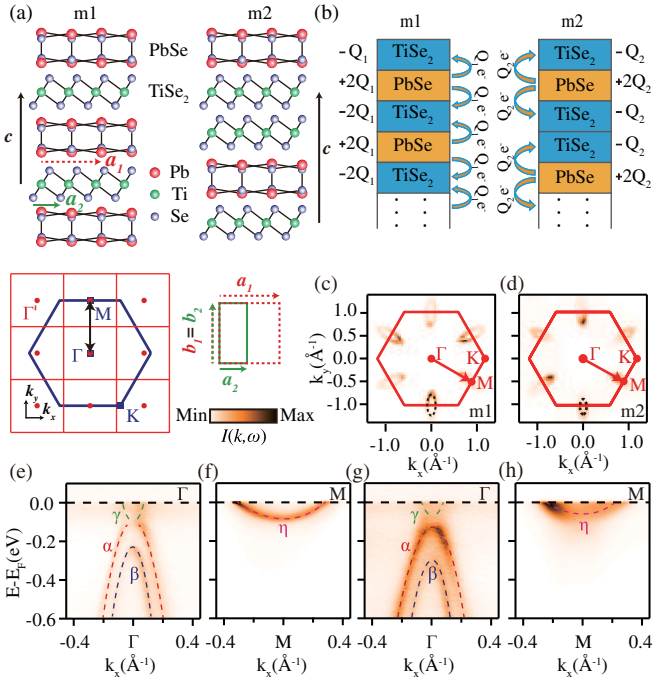

FIG. 1. (a) Crystal structure of $(PbSe)_{1.16}(TiSe_2)_m$ $(m = 1, 2)$. The bottom left depicts the projected 2D Brillouin zones (BZ) of the $TiSe_2$ (blue hexagon) and PbSe layers (red squares). Note that the Γ point of the second PbSe BZ and the M point of the $TiSe_2$ layer coincide. The bottom right shows a comparison of their lattice constants. (b) Schematic diagram of the charge transfer at interfaces. Orange and cyan rectangles represent PbSe and $TiSe_2$ layers, respectively. PbSe layers donate electrons to $TiSe_2$ layers. [(c) and (d)] Photoemission intensity maps of $m1$ and $m2$ at E_F, respectively, over the projected 2D BZ. Black dashed ellipses indicate the Fermi pockets and the intensity has been integrated over a window of $(E_F - 2.5$ meV, $E_F + 2.5$ meV). Data were threefold symmetrized. Photoemission intensity plots (e) and (f) for $m1$ and (g) and (h) for $m2$ are presented near Γ and M, respectively. The dashed lines indicate band dispersions obtained from the momentum and energy distribution curves (MDCs and EDCs). All data were taken at 10 K with 80 eV photons.

detailed comparison indicates significant electron doping in both $m1$ and $m2$. The estimated Luttinger volumes of the Fermi pockets are 13% and 7.4% of the Brillouin zone for $m1$ and $m2$, respectively (see more details in Supplemental Material [19]). Based on the charge transfer processes sketched in Fig. 1(b), the doped charge in the surface layer of $m1$ would be half its bulk value, while there is no charge reconstruction in $m2$, which gives bulk doping levels of 0.26 e^- and 0.074 e^- per $TiSe_2$ for $m1$ and $m2$, respectively [25–28]. This finding confirms the previous model that the PbSe layers serve as a carrier reservoir for $TiSe_2$ layers, thus giving rise to the charge transfer. When the thickness of the $TiSe_2$ layers is halved from $m2$ to $m1$, the amount of transferred charge increases by as large as 250%, which suggests that varying the thickness of the interleaved layers might provide a rather efficient means of tuning

charge transfer in VDWHs. We note that the charge transfer originates from the difference in Fermi level/chemical potential of neighboring layers in VDWHs [19]. Although our findings are on bulk misfit compounds, they represent the behaviors of VDWHs down to a few unit cells. As shown by the static electric model analysis in Supplemental Material [19,29], the charge distribution is stable and independent of the number of unit cells down to 2 u.c. of PbSe/$TiSe_2$, 2 u.c. PbSe/$TiSe_2$/$TiSe_2$, or 1 u.c. $TiSe_2$/PbSe/$TiSe_2$.

More detailed electronic structure comparisons of $m1$ and $m2$ are shown in Figs. 1(e)–1(h). In the vicinity of E_F, one electronlike (γ) and two holelike bands (α and β) around Γ together with another electronlike band (η) around M can be clearly resolved. As in the bulk material, η is a Ti $3d$ band while the highly dispersive α and β are spin-orbit-split Se $4p$ bands [30,31]. However, we stress that the γ band in $(PbSe)_{1.16}(TiSe_2)_m$ cannot be assigned as scattered states by the charge-density-wave (CDW) wave vector as in $1T$-$TiSe_2$, since the CDW is unlikely present in $m1$ and $m2$ for the following reasons. First, throughout the whole temperature range from 300 to 10 K, we have never found any sign of band folding in our ARPES measurements, which is the smoking gun for the presence of bulk or surface CDW states in $1T$-$TiSe_2$ [32]. Secondly, our ARPES measurements have confirmed nearly the same photoemission spectra of $m2$ as those of $Cu_{0.65}TiSe_2$, which is located in the same optimal doping regime as $m2$; CDW has been proven absent at this doping [32,33]. Thirdly, the doping level of $m1$ is much higher than $m2$ on the surface, and even higher in the bulk, and thus $m1$ is further away from the CDW regime than $m2$. Instead, γ is more reasonably accounted for as the electronic states of $TiSe_2$ scattered from M by the reciprocal lattice constant of the PbSe layers [illustrated by the double-headed arrow in Fig. 1(a)]. This result suggests that the charge density from the PbSe layers impinges upon the $TiSe_2$ planes, serving as a commensurate potential that scatters the electrons therein [34].

The dramatic change in the transferred charge with m is accompanied by an unexpected modulation of the photoemission spectra of these naturally occurring VDWHs. Figures 2(a) and 2(b) compare EDCs of $m1$ and $m2$ along Γ-M at low temperatures. Note that while the η band of $m1$ shows typical quasiparticlelike dispersion with sharp and well-defined peaks, the spectral line shape of $m2$ taken at the same momenta is remarkably broad and the linewidth is on the same order as the dispersion, which strongly suggests the incoherent nature of the spectra. Meanwhile, the maxima of these incoherent peaks still follow the dispersion predicted by band structure calculations. Taking spectra around the η band bottoms of both compounds as an example [Fig. 2(c)], rather different behavior is clearly observed. The EDC for $m1$ is well fit by a Lorentzian peak having a linewidth of 22.1 meV, in which

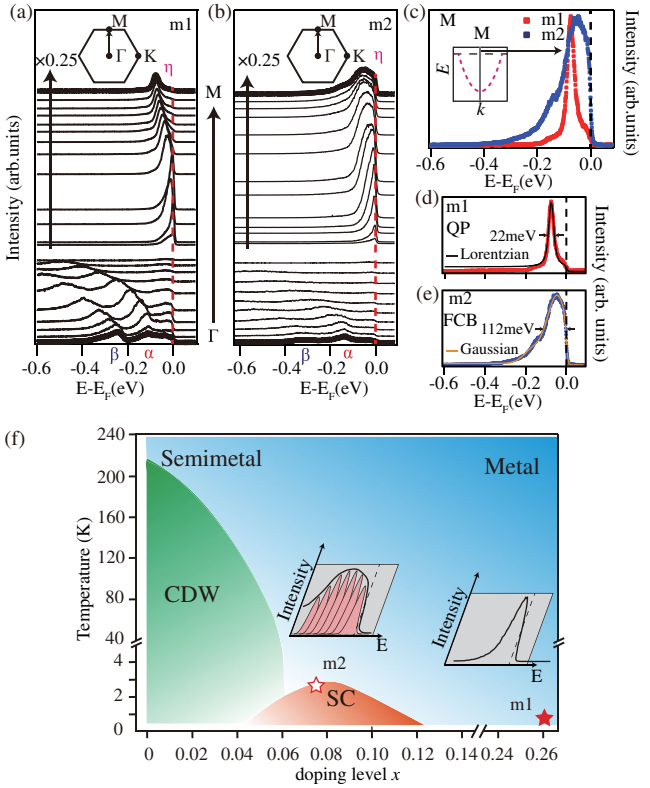

FIG. 2. [(a) and (b)] EDCs along the Γ-M cuts shown in Figs. 1(c) and 1(d) for $m1$ and $m2$, respectively. Spectra around M have been intentionally scaled down by 0.25 to be comparable to those around Γ. (c) Comparison of their EDCs at the M point. The line shape (d) for $m1$ can be fitted by a Lorentzian peak, while that (e) for $m2$ is fit best by a Gaussian envelope. (f) The phase diagram of electron-doped $TiSe_2$, whose regime below 0.1 doping is reproduced from that of Cu_xTiSe_2 with one Cu ion doping one electron [33], and the overdoped regime is a sketch. $m1$ is located in the heavily overdoped regime with quasiparticle-like spectra, which extends the original phase diagram, while $m2$ is located in the optimally doped regime and its spectra exhibit the typical Franck-Condon broadening of polarons due to strong EPC.

the shadow band background and the Fermi-Dirac function have been considered [Fig. 2(d)]. In contrast, as shown in Fig. 2(e), the line shape of the spectrum taken from $m2$ is clearly nonquasiparticlelike, and it can only be reasonably fit by a Gaussian function with a linewidth of 112 meV, more than 5 times wider than $m1$. Note that both samples are rather 2D in nature (see Supplemental Material [19] for details, [35]) and transport measurements have further proven the more 2D electronic structure of $m2$. Furthermore, X-ray diffraction and transition electron microscopy have illustrated the similar crystalline quality of our $m1$ and $m2$ samples [18]. Therefore, this unconventional spectroscopic broadening of $m2$ is not due to k_z broadening or disorder. Moreover, since the actual doping in bulk is twice that on the surface for $m1$, its linewidth of bulk states should be even much smaller.

Such spectroscopic linewidth broadening has also been reported at low doping x in Cu_xTiSe_2 [32]—photoemission spectra of $Cu_{0.065}TiSe_2$, located in the same optimal doping regime as $m2$, exhibit an analogous broad feature. The observed sharp Fermi edges in both our data and Ref. [32] represent the Fermi-Dirac cutoff of a broad feature extending well above E_F. This behavior is characteristic of the typical polarons in transition metal chalcogenides [36,37], indicating the very strong EPC in $m2$, which is reasonable as it is in proximity to a CDW phase [38]. In principle, our first-principles calculations can reproduce the tendency for diminishing EPC strength with increasing electron doping in $TiSe_2$, with the coupling constant λ decreasing from 0.55 in $m2$ to 0.51 in $m1$ (see Supplemental Material [19] for more details of calculations, [39–41]). However, the $>500\%$ difference in the spectroscopic linewidth between these two sibling VDWHs is not well accounted for by this calculation, suggesting a much more drastic change in the EPC strength owing to charge transfer. Our findings also suggest that the strong EPC would likely reduce the charge transfer and cause the observed large difference between $m1$ and $m2$—the two $TiSe_2$ layers in $m2$ would share electrons transferred from one layer of PbSe, so that the carrier concentration in its $TiSe_2$ layer would be less than the $m1$ case, which results in stronger EPC that subsequently reduces the charge transfer. This possibility needs to be tested by further calculations including the doping dependent EPC. Moreover, one immediate consequence of such a significant modulation of the EPC is on the emergence of superconductivity in $(PbSe)_{1.16}(TiSe_2)_m$ ($m = 1,\ 2$). As summarized in the phase diagram of electron-doped $TiSe_2$ [Fig. 2(f)], the spectra of $m2$ exhibit typical Franck-Condon broadening of polarons due to rather strong EPC, while those of $m1$ behave like the coherent quasiparticle in a weak-coupling regime (see more analysis in Supplemental Material [19]). The weak EPC in $m1$ explains its absence of superconductivity despite the higher density of states near E_F than in $m2$.

Unexpectedly, we discovered that the carrier concentrations of these naturally occurring VDWHs exhibit strong temperature dependence. The upper halves of Fig. 3(a) show the room-temperature photoemission intensity maps of $m1$ and $m2$. Compared with those taken at low temperatures, the electron pockets around M shrink markedly. The more quantitative comparison of Fermi surface contours at different temperatures [the lower part of Fig. 3(a)], extracted from the MDC peak fitting, further confirms that the charge transferred from PbSe to $TiSe_2$ is reduced for both $m1$ and $m2$ on increasing temperature. This shrinking of the Fermi pockets can be attributed to the upward shift of the Ti $3d$ η band [Fig. 3(b)], which could be directly observed from comparisons of EDCs taken at high and low temperatures for $m1$ and $m2$ as well [Figs. 3(c1)–3(c2)]. Detailed temperature dependence measurements indicate that this band shift is continuous and not due to some sudden phase transition, as illustrated in Fig. 3(d). Quantitatively, the η bands of $m1$ and $m2$ shift as much as 24.5 and 21.2 meV towards E_F, respectively, from our lowest measurement temperature to room temperature [Fig. 3(e)].

To account for the temperature-dependent energy shift of the η band, we have considered the thermal expansion

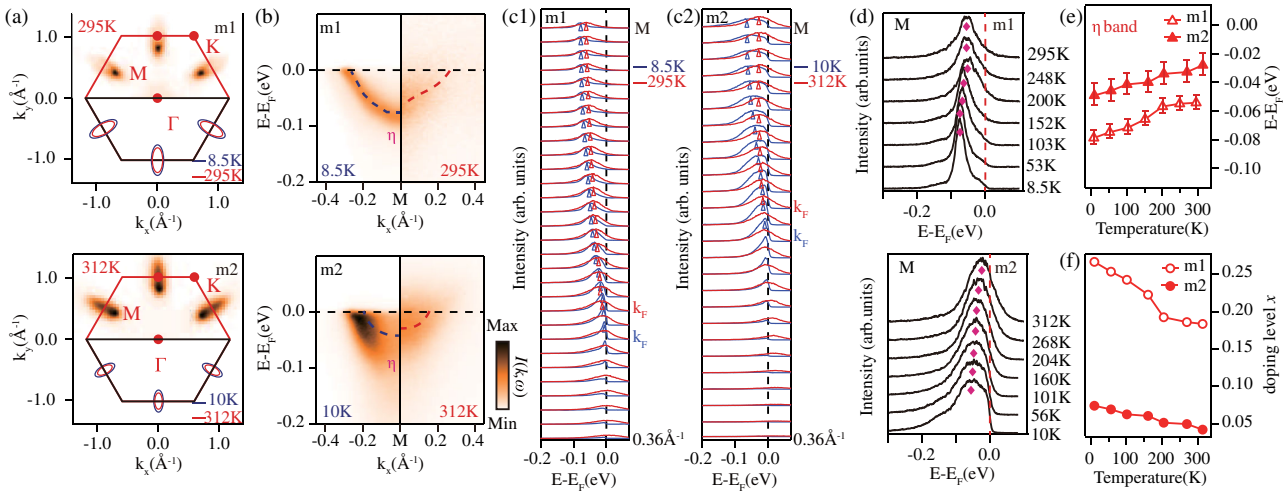

FIG. 3. (a) Fermi surfaces of $(PbSe)_{1.16}(TiSe_2)_m$ ($m = 1, 2$). The upper halves are room-temperature photoemission intensity maps of $m1$ and $m2$ integrated over ($E_F - 2.5$ meV, $E_F + 2.5$ meV). Data were sixfold symmetrized. The lower halves are a quantitative comparison of Fermi pocket size at low (8.5 and 10 K) and room (295 and 312 K) temperatures. (b) Comparisons of photoemission intensity plots around M for $m1$ and $m2$ at low and ambient temperatures. ($c1 - c2$) Direct comparisons of the EDCs taken at high and low temperatures for $m1$ and $m2$, respectively. (d) Temperature-dependent EDCs located at M for $m1$ and $m2$, respectively. (e) Temperature dependence of the η band bottom energy for $m1$ and $m2$. (f) Temperature dependence of carrier concentrations for $m1$ and $m2$ due to charge transfer.

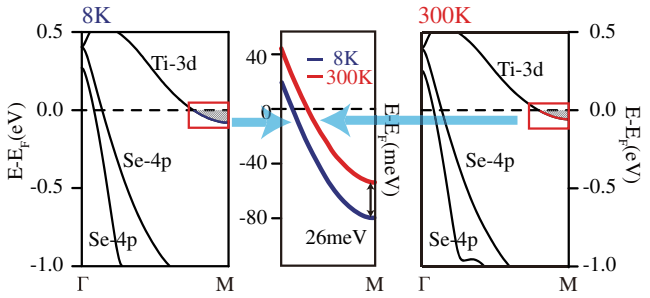

FIG. 4. Band structure comparison of the $TiSe_2$ component in misfit VDWHs at low and room temperatures, as simulated by first-principles calculations based on the thermal expansion of the lattice.

effect of the $TiSe_2$ lattice and then estimated the Ti $3d$ band shift through band structure calculations (Fig. 4) [42]. This band energy shift is calculated to be about 26 meV from 8 to 300 K, in good agreement with our experimental results (see Supplemental Material [19] for details of this calculation). Since the chemical potential of PbSe lies higher in energy than the Fermi level of $TiSe_2$ [43] and the upward shift of the Ti $3d$ band observed on warming in misfit VDWHs would reduce the energy gap between them, the electron transfer from PbSe to $TiSe_2$ is effectively suppressed. Accordingly, the resulting carrier concentrations of $m1$ and $m2$ are modulated by as much as 30% and 40%, respectively, by temperature [Fig. 3(f)]. Currently, most prototype devices based on VDWHs are designed mainly according to their low-temperature properties, but are intended to be employed in a room-temperature environment. If such a huge variation in carrier concentration with temperature occurs more generally in VDWHs, it is essential that it should be taken into account.

To summarize, we have comprehensively characterized the electronic structure of the typical naturally occurring VDWHs $(PbSe)_{1.16}(TiSe_2)_m$ $(m = 1, 2)$. By varying the thickness of the $TiSe_2$ layers, we can realize carrier concentration modulation of these VDWHs on an unprecedentedly large scale. Simultaneously, the EPC strength in these VDWHs can be tuned via charge transfer, and thus the domelike dependence of the superconducting transition temperature with carrier concentration in electron-doped $TiSe_2$ can be understood. Most remarkably, a dramatic temperature-dependent band shift is revealed that cuts the carrier concentration nearly in half on warming to room temperature. These findings may provide crucial feedback for the application of devices based on VDWHs and offer a new direction to further our understanding of this interesting class of materials.

We acknowledge Diamond Light Source for time on beamline I05 under proposal SI14737, which contributed to the results presented here. We gratefully acknowledge experimental support from Drs. D. H. Lu, T. K. Kim, M. Hoesch, L. G. Ma, and helpful discussions with Drs. T. P. Ying, R. Peng, and D. C. Peets. This work is supported by the National Key R&D Program of the MOST of China (Grant No. 2016YFA0300200) and the National Science Foundation of China (Grants No. 11574337, No. 11227902, and No. U1332209). D. W. S. is also supported by "Award for Outstanding Member in Youth Innovation Promotion Association CAS".

*dwshen@mail.sim.ac.cn

[1] A. K. Geim and I. V. Grigorieva, Nature (London) **499**, 419 (2013).
[2] D. Jariwala, V. K. Sangwan, L. J. Lauhon, T. J. Marks, and M. C. Hersam, ACS Nano **8**, 1102 (2014).
[3] X. Cui, G. Lee, Y. D. Kim, G. Arefe, P. Y. Huang, C. Lee, D. A. Chenet, X. Zhang, L. Wang, F. Ye, F. Pizzocchero, B. S. Jessen, K. Watanabe, T. Taniguchi, D. A. Muller, T. Low, P. Kim, and J. Hone, Nat. Nanotechnol. **10**, 534 (2015).
[4] K. S. Novoselov, A. Mishchenko, A. Carvalho, and A. H. Castro Neto, Science **353**, aac9439 (2016).
[5] J. E. Padilha, A. Fazzio, and A. J. R. da Silva, Phys. Rev. Lett. **114**, 066803 (2015).
[6] P. Rivera, K. L. Seyler, H. Yu, J. R. Schaibley, J. Yan, D. G. Mandrus, W. Yao, and X. Xu, Science **351**, 688 (2016).
[7] B. Hunt, J. D. Sanchez-Yamagishi, A. F. Young, M. Yankowitz, B. J. LeRoy, K. Watanabe, T. Taniguchi, P. Moon, M. Koshino, P. Jarillo-Herrero, and R. C. Ashoori, Science **340**, 1427 (2013).
[8] C. R. Dean, L. Wang, P. Maher, C. Forsythe, F. Ghahari, Y. Gao, J. Katoch, M. Ishigami, P. Moon, M. Koshino, T. Taniguchi, K. Watanabe, K. L. Shepard, J. Hone, and P. Kim, Nature (London) **497**, 598 (2013).
[9] A. Tsukazaki, S. Akasaka, K. Nakahara, Y. Ohno, H. Ohno, D. Maryenko, A. Ohtomo, and M. Kawasaki, Nat. Mater. **9**, 889 (2010).
[10] X. Du, I. Skachko, F. Duerr, A. Luican, and E. Y. Andrei, Nature (London) **462**, 192 (2009).
[11] C. Lee, G. Lee, A. M. van der Zande, W. Chen, Y. Li, M. Han, X. Cui, G. Arefe, C. Nuckolls, T. F. Heinz, J. Guo, J. Hone, and P. Kim, Nat. Nanotechnol. **9**, 676 (2014).
[12] G. Wiegers, Prog. Solid State Chem. **24**, 1 (1996).
[13] G. Wiegers and A. Meerschaut, J. Alloys Compd. **178**, 351 (1992).
[14] J. Rouxel, A. Meerschaut, and G. Wiegers, J. Alloys Compd. **229**, 144 (1995).
[15] A. J. Molina-Mendoza, E. Giovanelli, W. S. Paz, M. A. Niño, J. O. Island, C. Evangeli, L. Aballe, M. Foerster, H. S. J. van der Zant, G. Rubio-Bollinger, N. Agraït, J. J. Palacios, E. M. Pérez, and A. Castellanos-Gomez, Nat. Commun. **8**, 14409 (2017).
[16] M. Velický, P. S. Toth, A. M. Rakowski, A. P. Rooney, A. Kozikov, C. R. Woods, A. Mishchenko, L. Fumagalli, J. Yin, V. Zlyomi, T. Georgiou, S. J. Haigh, K. S. Novoselov, and R. A. W. Dryfe, Nat. Commun. **8**, 14410 (2017).
[17] D. Merrill, D. Moore, S. Bauers, M. Falmbigl, and D. Johnson, Materials **8**, 2000 (2015).
[18] N. Z. Wang, S. F. Yuan, R. Cong, X. F. Lu, F. B. Meng, C. Shang, and X. H. Chen, Europhys. Lett. **112**, 67007 (2015).

[19] See Supplemental Material http://link.aps.org/supplemental/10.1103/PhysRevLett.120.106401 for more details on experiments, data analysis, and calculations.
[20] G. Kresse and D. Joubert, Phys. Rev. B **59**, 1758 (1999).
[21] G. Kresse and J. Furthmller, Comput. Mater. Sci. **6**, 15 (1996).
[22] J. P. Perdew, K. Burke, and M. Ernzerhof, Phys. Rev. Lett. **77**, 3865 (1996).
[23] D. D. Koelling and B. N. Harmon, J. Phys. C **10**, 3107 (1977).
[24] P. Chen, Y. H. Chan, X. Y. Fang, Y. Zhang, M. Y. Chou, S. K. Mo, Z. Hussain, A. V. Fedorov, and T. C. Chiang, Nat. Commun. **6**, 8943 (2015).
[25] J. M. Luttinger and J. C. Ward, Phys. Rev. **118**, 1417 (1960).
[26] N. Nakagawa, H. Y. Hwang, and D. A. Muller, Nat. Mater. **5**, 204 (2006).
[27] X. H. Niu, R. Peng, H. C. Xu, Y. J. Yan, J. Jiang, D. F. Xu, T. L. Yu, Q. Song, Z. C. Huang, Y. X. Wang, B. P. Xie, X. F. Lu, N. Z. Wang, X. H. Chen, Z. Sun, and D. L. Feng, Phys. Rev. B **92**, 060504 (2015).
[28] R. Peng, H. C. Xu, M. Xia, J. F. Zhao, X. Xie, D. F. Xu, B. P. Xie, and D. L. Feng, Appl. Phys. Lett. **104**, 081606 (2014).
[29] J. H. Davies, *The Physics of Low-Dimensional Semiconductors: An Introduction* (Cambridge University Press, Cambridge, 1997).
[30] T. E. Kidd, T. Miller, M. Y. Chou, and T.-C. Chiang, Phys. Rev. Lett. **88**, 226402 (2002).
[31] P. Aebi, T. Pillo, H. Berger, and F. Lévy, J. Electron Spectrosc. Relat. Phenom. **117–118**, 433 (2001).
[32] J. F. Zhao, H. W. Ou, G. Wu, B. P. Xie, Y. Zhang, D. W. Shen, J. Wei, L. X. Yang, J. K. Dong, M. Arita, H. Namatame, M. Taniguchi, X. H. Chen, and D. L. Feng, Phys. Rev. Lett. **99**, 146401 (2007).
[33] E. Morosan, H. W. Zandbergen, B. S. Dennis, J. W. G. Bos, Y. Onose, T. Klimczuk, A. P. Ramirez, N. P. Ong, and R. J. Cava, Nat. Phys. **2**, 544 (2006).
[34] H. W. Ou, J. F. Zhao, Y. Zhang, B. P. Xie, D. W. Shen, Y. Zhu, Z. Q. Yang, J. G. Che, X. G. Luo, X. H. Chen, M. Arita, K. Shimada, H. Namatame, M. Taniguchi, C. M. Cheng, K. D. Tsuei, and D. L. Feng, Phys. Rev. Lett. **102**, 026806 (2009).
[35] P. Chen, Y. H. Chan, X. Y. Fang, S. K. Mo, Z. Hussain, A. V. Fedorov, M. Y. Chou, and T. C. Chiang, Sci. Rep. **6**, 37910 (2016).
[36] L. Perfetti, H. Berger, A. Reginelli, L. Degiorgi, H. Höchst, J. Voit, G. Margaritondo, and M. Grioni, Phys. Rev. Lett. **87**, 216404 (2001).
[37] F. Caruso, H. Lambert, and F. Giustino, Phys. Rev. Lett. **114**, 146404 (2015).
[38] Y. Liu, D. F. Shao, L. J. Li, W. J. Lu, X. D. Zhu, P. Tong, R. C. Xiao, L. S. Ling, C. Y. Xi, L. Pi, H. F. Tian, H. X. Yang, J. Q. Li, W. H. Song, X. B. Zhu, and Y. P. Sun, Phys. Rev. B **94**, 045131 (2016).
[39] P. Giannozzi *et al.*, J. Phys. Condens. Matter **21**, 395502 (2009).
[40] J. P. Perdew and A. Zunger, Phys. Rev. B **23**, 5048 (1981).
[41] P. B. Allen and R. C. Dynes, Phys. Rev. B **12**, 905 (1975).
[42] S. L. Budko, P. C. Canfield, E. Morosan, R. J. Cava, and G. M. Schmiedeshoff, J. Phys. Condens. Matter **19**, 176230 (2007).
[43] D. R. Merrill, D. B. Moore, S. R. Bauers, M. Falmbigl, and D. C. Johnson, Materials **8**, 2000 (2015).

CHIN. PHYS. LETT. Vol. 32, No. 5 (2015) 057402

Tuning the Electronic Structure of Sr_2IrO_4 Thin Films by Bulk Electronic Doping Using Molecular Beam Epitaxy *

LI Ming-Ying(李明颖)[1], LIU Zheng-Tai(刘正太)[1], YANG Hai-Feng(杨海峰)[1], ZHAO Jia-Lin(赵家琳)[1], YAO Qi(姚岐)[1,2], FAN Cong-Cong(樊聪聪)[1], LIU Ji-Shan(刘吉山)[1], GAO Bo(高波)[1], SHEN Da-Wei(沈大伟)[1**], XIE Xiao-Ming(谢晓明)[1]

[1]*State Key Laboratory of Functional Materials for Informatics, Shanghai Institute of Microsystem and Information Technology (SIMIT), Chinese Academy of Sciences, Shanghai 200050*

[2]*State Key Laboratory of Surface Physics, Department of Physics, and Advanced Materials Laboratory, Fudan University, Shanghai 200433*

(Received 16 April 2015)

By means of oxide molecular beam epitaxy with shutter-growth mode, we fabricate a series of electron-doped $(Sr_{1-x}La_x)_2IrO_4$ (001) (x=0, 0.05, 0.1 and 0.15) single crystalline thin films and then investigate the doping dependence of the electronic structure utilizing in-situ angle-resolved photoemission spectroscopy. It is found that with the increasing doping content, the Fermi levels of samples progressively shift upward. Prominently, an extra electron pocket crossing the Fermi level around the M point is evidently observed in the 15% nominal doping sample. Moreover, bulk-sensitive transport measurements confirm that the doping effectively suppresses the insulating state with respect to the as-grown Sr_2IrO_4, though the doped samples still remain insulating at low temperatures due to the localization effect possibly stemming from disorders including oxygen deficiencies. Our work provides another feasible doping method to tune electronic structure of Sr_2IrO_4.

PACS: 71.20.−b, 71.30.+h, 73.21.Ac, 77.55.Px DOI: 10.1088/0256-307X/32/5/057402

Researchers may notice that 5*d* transition-metal oxides (TMOs) have recently drawn a great deal of attention. In these compounds, the complicated interplay between spin-orbit coupling (SOC) and electron correlations has been suggested to host multiple novel quantum states, including topological Mott insulators,[1] Weyl semimetals,[3,4] axion insulators,[5,6] and spin liquids.[7–9] These studies were mostly initialized by the pioneering experiments on the prototype layered perovskite Sr_2IrO_4, in which the strong SOC was revealed to lift the orbital degeneracy and then to result in a narrow half-filled $J_{\rm eff} = 1/2$ band so that even the relatively weak Coulomb repulsion of 5*d* electrons could induce a Mott metal-insulator transition (MIT) therein.[2,10] Scattering experiments have found that this Mott insulator, showing an effective pseudospin 1/2 antiferromagnetic (AFM) order at low temperature, can be well described by the Heisenberg model with an exchange coupling of 60–100 meV.[11,12] Such findings indicate that the low-energy behavior of this single-layer iridate rather resembles that of cuprates. Consequently, it is tempting to investigate the carrier doping of Sr_2IrO_4, which might pave the way to discover a new family of unconventional superconductors. Indeed, a recent theoretical work has predicted the unconventional superconductivity in the electron-doped Sr_2IrO_4.[13]

In this context, various experimental attempts have been performed to achieve the effective carrier doping of Sr_2IrO_4.[14,15,18–21] So far, one of the most promising progresses is the try of surface electron doping of Sr_2IrO_4 via *in situ* potassium deposition, in which Fermi arcs and pseudogap behavior have been reported.[16] Nevertheless, this finding is not consistent with the reports on the sibling La-doped $Sr_3Ir_2O_7$, in which only small Fermi pockets rather than Fermi arcs were revealed.[22,23] This controversy naturally raises one open question, namely, whether the existence of Fermi arcs is an universal property of the electron-doped iridates irrespective of the specific doping method. As there has been no equivalent study reported so far for La-doped Sr_2IrO_4. This important question still remains unanswered.

In the present work, we synthesize a series of high-quality La-doped Sr_2IrO_4 thin films on $SrTiO_3$(001) single crystal substrates by means of oxide molecular beam epitaxy (OMBE), by which the metastable phases with large electron doping levels could be stabilized in the formation of thin films. We can thus investigate the electron-doping dependence of electronic structure of bulk Sr_2IrO_4 through *in situ* angle-resolved photoemission spectroscopy (ARPES). We find that, with the increasing La-doped content, the Fermi levels of samples gradually shift upward to the conduction band, which is consistent with the electron doping. In addition, we recognize an extra electron-

*Supported by the National Basic Research Program of China (973 Program) under Grant Nos 2011CBA00106 and 2012CB927400, the National Natural Science Foundation of China under Grant Nos 11274332 and 11227902, and Helmholtz Association through the Virtual Institute for Topological Insulators (VITI). M. Y. Li and D. W. Shen are also supported by the Strategic Priority Research Program (B) of the Chinese Academy of Sciences under Grant No XDB04040300.

**Correspondence author. Email: dwshen@mail.sim.ac.cn

© 2015 Chinese Physical Society and IOP Publishing Ltd

like band crossing the Fermi level upon 15% nominal La-doping, forming one pocket-like feature around the boundary of the reduced Brillouin zone (BZ), in stark contrast to as-grown Sr_2IrO_4 samples. Although electric transport measurements manifest that the lanthanum substitution of Sr can significantly suppress the resistivity of this system, the doped Sr_2IrO_4 still shows clear insulating behavior. We argue that this may be caused by the random carrier hoping between localized states in our system due to inevitable oxygen related defects.

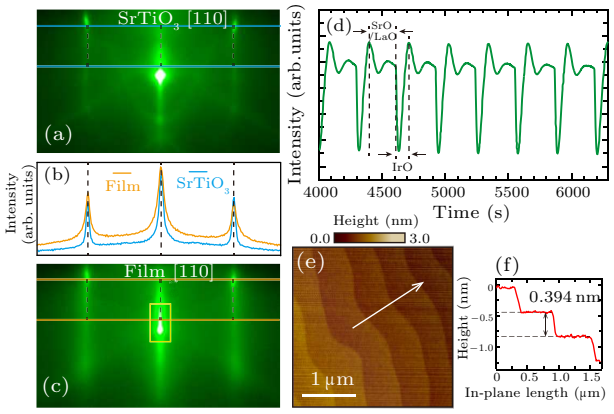

Fig. 1. (a) and (c) RHEED patterns of the $SrTiO_3(001)$ substrate and as-grown $(Sr_{0.95}La_{0.05})_2IrO_4$ along $[110]_p$ azimuth direction, respectively. (b) RHEED intensity curves integrated within the rectangle windows in panels (a) and (c). (d) Time dependence of the intensity of [00] diffraction streak in RHEED pattern of $(Sr_{1-x}La_x)_2IrO_4$ ($x = 0.05$) thin film during deposition. (e) AFM topographic image of as-grown $(Sr_{0.95}La_{0.05})_2IrO_4$ thin film. (f) The in-plane length dependence of height along the arrow direction in panel (e).

The La-doped $Sr_2IrO_4(001)$ films were deposited onto $SrTiO_3(001)$ single crystalline substrates using a DCA R450 OMBE system. The flat stepped surface of substrates was obtained by etching in hydrofluoric acid buffer solution (BHF) and annealing in a muffle furnace according the standard procedure.[24] The in-plane lattice constant of $SrTiO_3$ substrates is 3.905 Å, which leads to a 0.44% tensile strain to the pseudo-cubic $(La,Sr)_2IrO_4$ (3.888 Å). The shuttered growth mode was applied to synthesize the films in the distilled ozone atmosphere of 2×10^{-6} Torr. During the growth, the temperature of substrates was kept at 800℃ verified by the thermocouple behind the sample stage. Moreover, the overall growth rate and surface structure of thin films were monitored by *in situ* reflection high-energy electron diffraction (RHEED) during the growth. Strontium (lanthanum) and iridium were evaporated from Knudsen effusion cells and an electron beam evaporator, respectively. All the doping levels mentioned here are nominal values.

Figures 1(a) and (c) show the RHEED patterns of the $SrTiO_3(001)$ substrate before the growth and after the growth of the 6-unit-cell $(Sr_{0.95}La_{0.05})_2IrO_4$ thin film, respectively, which were both taken with a glancing electron beam parallel to the $[110]_p$ azimuthal direction. These RHEED images exhibit prominent Kikuchi lines, indicating the high crystalline perfection of films. We compared the RHEED intensity curves integrated within the rectangle windows of the $(Sr_{0.95}La_{0.05})_2IrO_4$ film and substrate [Fig. 1(b)], and the negligible shift of the intensity peak indicates that there is no evident lattice relaxation for the strained film. The amplitudes and periods of RHEED intensity oscillations of the [00] diffraction streak tend to be constant once the Sr(La)/Ir flux ratio is adjusted to be close to stoichiometric 2. However, to further confirm that the shuttered $SrO/(La_2O_3)_{0.5}$ and IrO_2 monolayers are complete during the growth, we measured the total thickness of films and their c-axis lattice constants through x-ray diffraction (XRD) to estimate the actual number of unit cells. By comparing this value to the number of shutting periods of our calibration sample, we can then deduce the scaling factor, by which we can calibrate the Sr/La and Ir shutter opening times. In this way, the layer-by-layer growth of $(Sr_{1-x}La_x)_2IrO_4$ films could be achieved. Figure 1(d) shows a typical RHEED intensity oscillation of the [00] diffraction streak (surrounded by a yellow pane in Fig. 1(c)) of such a calibrated film. By means of the *ex situ* atomic force microscopy (AFM), we further examined the typical surface morphology of our thin film, as displayed in Fig. 1(e). The film surface shows a well defined terrace-step structure with a typical step height of 0.394 nm [Fig. 1(f)], preserving the flat terraces and surface morphology of $SrTiO_3(001)$ substrates. This finding confirms the layer-by-layer growth mode of our films. Moreover, since all growths of our films were terminated after an integral number of oscillation finishing, we can expect a single IrO_2 surface termination for all the films.

To characterize the phase purity and crystallinity of $(Sr_{1-x}La_x)_2IrO_4$ thin films, the high-resolution cross-sectional transmission electron microscopy (TEM) and the *ex situ* XRD measurements were performed. Figures 2(a) and 2(b) show the TEM images of the typical Sr_2IrO_4 and $(Sr_{0.85}La_{0.15})_2IrO_4$ thin films deposited on $SrTiO_3(001)$ substrates. Both data demonstrate the continuous and evenly spaced $SrO/(La_2O_3)_{0.5}$ and IrO_2 layers and the atomically sharp interfaces between the epitaxial thin films and the substrates, with no discernible interdiffusion or vacancy observable. The XRD results of typical $(Sr_{1-x}La_x)_2IrO_4$ thin films are shown in Figs. 2(c) and 2(d). The θ–2θ scans of the films [Fig. 2(d)] are consistent with the growth of phase-pure (001)-oriented $(Sr_{1-x}La_x)_2IrO_4$. The clear Kiessig interface fringes indicate smooth film surfaces and sharp interfaces between the thin films and substrates. We also measured the rocking curves around the (006) peaks of Sr_2IrO_4 and $(Sr_{0.85}La_{0.15})_2IrO_4$, as shown in Fig. 2(c). The full widths at half maximum (FWHM) of these curves are 0.062° and 0.069°, respectively, in-

dicating the good epitaxial film quality. In addition, through Bragg's function on the (006) peak positions, we can deduce the out-of-plane c lattice constants of Sr_2IrO_4 and $(Sr_{0.85}La_{0.15})_2IrO_4$ to be 12.782 Å and 12.821 Å, respectively. For comparison, the out-of-plane c lattice constant of bulk Sr_2IrO_4 was determined to be 12.899 Å.[25] Obviously, the in-plane tensile strain for the epitaxial films results in the compression in the out-of-plane c direction, while the doping of lanthanum with smaller ionic radius partially counterbalances this effect. From another perspective, this finding confirms the real bulk doping of lanthanum in our $(Sr_{1-x}La_x)_2IrO_4$ films grown by OMBE.

After growth, we performed *in situ* ARPES measurements on these samples in order to investigate the electron doping evolution of $(Sr_{1-x}La_x)_2IrO_4$. Thin films were transferred through an ultrahigh vacuum buffer chamber (1.0×10^{-10} Torr) to the combined ARPES chamber for measurements immediately after the growth. This ARPES system is equipped with a VG-Scienta R8000 electron analyzer and a SPECS UVLS helium discharging lamp. The data were collected at 40 K under ultrahigh vacuum of 8×10^{-11} Torr. The angular resolution was 0.3°, and the overall energy resolution was set to 15 meV (He I, 21.2 eV photon energy). During the measurements, the films were stable and did not show any sign of degradation.

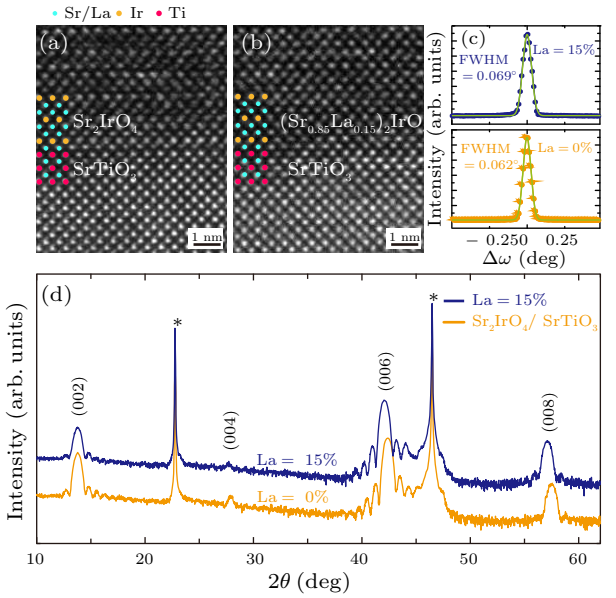

Fig. 2. (a) and (b) TEM cross-sections of Sr_2IrO_4 and $(Sr_{0.85}La_{0.15})_2IrO_4$ thin films on $SrTiO_3$(001) substrates, respectively. (c) Rocking curves of (006) diffraction peaks of Sr_2IrO_4 (orange symbol-line) and $(Sr_{0.85}La_{0.15})_2IrO_4$ (blue symbol-line) thin films, respectively. Green lines are Gauss curves for fitting the rocking curves of thin films. (d) X-ray diffraction θ-2θ scans of 8-nm-thick $(Sr_{1-x}La_x)_2IrO_4$ (x = 0 and 0.15) thins films on $SrTiO_3$(001) substrates. The characteristic peaks of substrates are labeled with an asterisk.

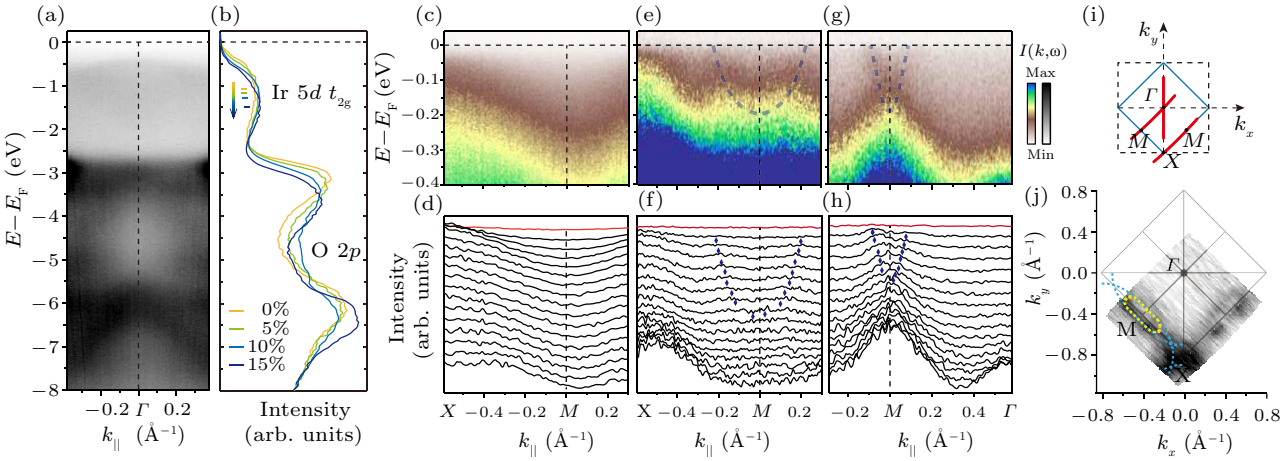

Fig. 3. (a) Photoemission intensity plots of Sr_2IrO_4 thin film along X–Γ–X direction, taken with 21.2 eV photon energy at 40 K. (b) The valence-band photoemission spectra at the Γ point for $(Sr_{1-x}La_x)_2IrO_4$ thins films. (c) Photoemission intensity plots along X–M of the Sr_2IrO_4 thin film. (e) and (g) Photoemission intensity plots along X–M and M–Γ of $(Sr_{0.85}La_{0.15})_2IrO_4$, respectively. (d), (f), (h) The momentum distribution curves for the data in panels (c), (e) and (g). (i) The two-dimensional projection of the Brillouin zone and the high-symmetry directions. The blue solid lines represent the reduced Brillouin zone. (j) Fermi surface map integrated over [E_F = −15 meV, E_F = +15 meV] of the $(Sr_{0.85}La_{0.15})_2IrO_4$ thin film. Yellow dashed lines guide for the elliptical Fermi surface around M. The blue dashed lines illustrate the reflected shadow band of Fermi arcs. All the APRES data were taken with 21.2 eV photon energy at 40 K.

Figure 3(a) shows the valence band photoemission intensity plot for Sr_2IrO_4 epitaxial films along X–Γ–X high-symmetry direction highlighted by the red line in Fig. 3(i). Comparing with DFT calculations, we can identify that the features between −7.0 and −2.0 eV are mainly contributed by the O 2p states, while the Ir t_{2g} orbitals mainly distribute the feature located at around −0.5 eV, as illustrated by the

integrated spectra in momenta around the Γ point [Fig. 3(b)].[10,26–28] However, upon further La doping (from $x = 0$ to 0.15 nominal doping level), we discovered a continuous energy shift (as large as ~500 meV) for these spectral features as shown in Fig. 3(b). This finding confirms the gradual electron doping into the insulating Sr_2IrO_4 by substituting Sr with La, which would increase the chemical potential of this system and keep pushing valence band (VB) features to higher binding energy. Here all the spectra have been renormalized by the spectral intensity at the binding energy of 8.0 eV for comparison.

Surprisingly, as for the sample with nominal 15% La-doping, we observe an extra electron-like band crossing the Fermi level [Figs. 3(e) and (g)], while the non-doped Sr_2IrO_4 just presents as a typical insulator with an energy gap [Fig. 3(c)]. Moreover, the comparison between the corresponding momentum distribution curves in Figs. 3(d), 3(f) and 3(h) further confirms this finding. As shown in Fig. 3(j), the band forms one elliptical electron pocket around the M point of the reduced Brillouin zone which is guided by yellow dashed line [Fig. 3(i)]. It seems that our findings are in qualitative agreement with the Fermi pockets discovered in the metallic electron-doped $Sr_3Ir_2O_7$, in which electron carriers are doped into the conduction band and produces a small Fermi surface containing only the added x electrons.[22] However, we could still not simply rule out the possibility of the Fermi arcs. Taking into account of the significant octahedral rotation and the possible antiferromagnetic (AF) ordering in $(Sr_{1-x}La_x)_2IrO_4$, it is highly possible for ARPES to observe the reflected shadow bands of the Fermi arcs, which would also produce the pocket-like feature as illustrated by the blue dashed lines in Fig. 3(j). To further pin down the origin of this pocket-like feature, a more detailed doping dependence of the low-lying electronic structure is highly imperative.

To further determine whether our findings are caused by the surface or the bulk electronic structure, we compared the in-plane resistivity of films with different doping levels. As shown in Fig. 4(a), for the as-grown Sr_2IrO_4, the normalized R–T curve manifests a typical insulator behavior and the resistivity has been out of measurement range when the temperature is below 70 K. Nevertheless, though the film with 15% nominal doping level still behaves as an insulator, its in-plane resistivity has dropped by around three orders at 70 K, and it is still in the range of our measuring system at as low as 5 K. This prominent change of the bulk properties of films is in good agreement with our ARPES result, and it undoubtedly supports that our findings are mainly caused by the electron doping into the bulk Sr_2IrO_4. We note that $(Sr_{0.85}La_{0.15})_2IrO_4$ is still insulating though there is finite spectrum weight in the vicinity of Fermi energy (E_F), which implies that this system might be in the strongly localized regime.[29] Figure 4(b) shows the logarithm of the in-plane resistivity as a function of $T^{-1/3}$ for a temperature range 5–300 K. In the low temperature range (5–40 K), we could observe an excellent agreement with a linear fit, consistent with the typical two-dimensional variable range hopping (VRH) model.[30] In this case, carriers would hop between localized states as sketched by the inset of Fig. 4(b). At higher temperatures, though there exists a slight deviation from the linear fit, we can conclude that the VRH may still be the main conduction mechanism. Recently, one scanning tunneling microscopy and spectroscopy experiment discovered some oxygen related defects on the surface of Sr_2IrO_4, which are likely native to the sample and regardless of the good sample quality.[31] Such random distribution of the defects are in good agreement with the VRH behavior in our in-plane resistivity data.

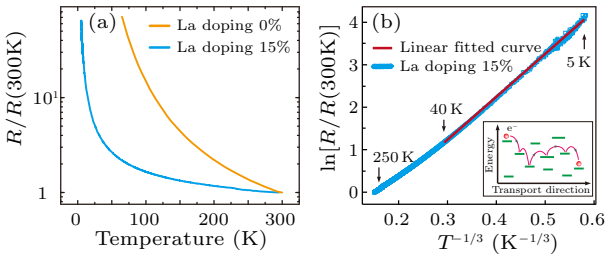

Fig. 4. (a) The temperature dependence of resistance for $(Sr_{1-x},La_x)_2IrO_4(001)$ ($x = 0$ and 0.15) epitaxial films, normalized by the resistance at 300 K temperature. (b) The logarithm of the in-plane normalized resistivity as a function of $T^{-1/3}$ for the $(Sr_{0.85},La_{0.15})_2IrO_4$ epitaxial film. Inset: sketch of a typical two-dimensional variable range hoping model.

In summary, we have grown a series of La-doped $(Sr_{1-x}La_x)_2IrO_4(001)$ ($x = 0$, 0.05, 0.1, and 0.15) epitaxial films on $SrTiO_3(001)$ substrates and studied the corresponding electronic structure and transport properties. By increasing the La-doping level, Fermi level for the samples are drifted up getting close to higher binding energy. Moreover, a fast dispersing state is observed around the M point for the samples with 15% La-doping. In addition, the R–T curves of $(Sr_{0.85}La_{0.15})_2IrO_4$ thin film is suppressed under the one of undoped Sr_2IrO_4 thin film. Although the La-doped content is as high as 15%, the films still remain insulators, which might be resulted from the strong localized effect induced by disorders including the oxygen defects in the samples.

We gratefully acknowledge Professor Donglai Feng, Dr. Rui Peng and Dr. Wei Li for the helpful discussion.

References

[1] Pesin D and Balents L 2010 *Nat. Phys.* **6** 376
[2] Kim B J, Ohsumi H, Komesu T, Sakai S, Morita T, Takagi H and Arima T 2009 *Science* **323** 1329
[3] Burkov A A and Balents L 2011 *Phys. Rev. Lett.* **107** 127205

[4] Yang K Y, Lu Y M and Ran Y 2011 *Phys. Rev.* B **84** 075129
[5] Witczak-Krempa W, Chen G, Kim Y B and Balents L 2014 *Annu. Rev. Condens. Matter Phys.* **5** 57
[6] Wan X G, Vishwanath A and Savrasov S Y 2012 *Phys. Rev. Lett.* **108** 146601
[7] Balents L 2010 *Nature* **464** 199
[8] Wen X G 2002 *Phys. Rev.* B **65** 165113
[9] Lawler M J, Paramekanti A, Kim Y B and Balents L 2008 *Phys. Rev. Lett.* **101** 197202
[10] Kim B J, Jin H, Moon S J, Kim J Y, Park B G, Leem C S, Yu J J, Noh T W, Kim C, Oh S J, Park J H, Durairaj V, Cao G and Rotenberg E 2008 *Phys. Rev. Lett.* **101** 076402
[11] Kim J, Casa D, Upton M H, Gog T, Kim Y J, Mitchell J F, van Veenendaal M, Daghofer M, van den Brink J, Khaliullin G and Kim B J 2012 *Phys. Rev. Lett.* **108** 177003
[12] Fujiyama S, Ohsumi H, Komesu T, Matsuno J, Kim B J, Takata M, Arima T and Takagi H 2012 *Phys. Rev. Lett.* **108** 247212
[13] Watanabe H, Shirakawa T and Yunoki S 2013 *Phys. Rev. Lett.* **110** 027002
[14] Ge M, Qi T F, Korneta O B, De Long D E, Schlottmann P, Crummett W P and Cao G 2011 *Phys. Rev.* B **84** 100402
[15] Qi T F, Korneta O B, Li L, Butrouna K, Cao V S, Wan X G, Schlottmann P, Kaul R K and Cao G 2012 *Phys. Rev.* B **86** 125105
[16] Kim Y K, Krupin O, Denlinger J D, Bostwick A, Rotenberg E, Zhao Q, Mitchell J F, Allen J W and Kim B J 2014 *Science* **345** 187
[17] Korneta O B, Qi T F, Chikara S, Parkin S, De Long L E, Schlottmann P and Cao G 2010 *Phys. Rev.* B **82** 115117
[18] Nichols J, Terzic J, Bittle E G, Korneta O B, De Long L E, Brill J W, Cao G and Seo S S A 2013 *Appl. Phys. Lett.* **102** 141908
[19] Serrao C R, Liu J, Heron J T, Singh-Bhalla G, Yadav A, Suresha S J, Paull R J, Yi D, Chu J H, Trassin M, Vishwanath A, Arenholz E, Frontera C, Zelezny J, Jungwirth T, Marti X and Ramesh R 2013 *Phys. Rev.* B **87** 085121
[20] Miao L D, Xu H and Mao Z Q 2014 *Phys. Rev.* B **89** 035109
[21] Lee J S, Krockenberger Y, Takahashi K S, Kawasaki M and Tokura Y 2012 *Phys. Rev.* B **85** 035101
[22] de la Torre A, Hunter E C, Subedi A, Mckeown Walker S, Tamai A, Kim T K, Hoesch M, Perry R S, Georges A and Baumberger F 2014 *Phys. Rev. Lett.* **113** 256402
[23] He J H, Hafiz H, Mion T R, Hogan T, Dhital C, Chen X, Lin Q, Hashimoto M, Lu D H, Zhang Y, Markiewicz R S, Bansil A, Wilson S D and He R H 2015 *Sci. Rep.* **5** 8533
[24] Kawasaki M, Takahashi K, Maeda T, Tsuchiya R, Shinohara M, Ishiyama O, Yonezawa T, Yoshimoto M and Koinuma H 1994 *Science* **266** 1540
[25] Crawford M K, Subramanian M A, Harlow R L, Fernandez-Baca J A, Wang Z R and Johnston D C 1994 *Phys. Rev.* B **49** 9198
[26] Arita R, Kunes J, Kozhevnikov A V, Eguiluz A G and Imada M 2012 *Phys. Rev. Lett.* **108** 086403
[27] Martins C, Aichihorn M, Vaugier L and Biermann S 2011 *Phys. Rev. Lett.* **107** 266404
[28] Watanabe H, Shirakawa T and Yunoki S 2010 *Phys. Rev. Lett.* **105** 216410
[29] Scherwitzl R, Gariglio S, Gabay M, Zubko P, Gibert M and Triscone J M 2011 *Phys. Rev. Lett.* **106** 246403
[30] Brenig W, Dohler G H and Heyszenau H 1973 *Philos. Mag.* **27** 1093
[31] Dai J X, Calleja E, Cao G and McElroy K 2014 *Phys. Rev.* B **90** 041102(R)

Copyright of Chinese Physics Letters is the property of IOP Publishing and its content may not be copied or emailed to multiple sites or posted to a listserv without the copyright holder's express written permission. However, users may print, download, or email articles for individual use.

Tunable electronic structure and surface states in rare-earth monobismuthides with partially filled f shell

Peng Li,[1] Zhongzheng Wu,[1] Fan Wu,[1] Chao Cao,[2,*] Chunyu Guo,[1] Yi Wu,[1] Yi Liu,[3] Zhe Sun,[3] Cheng-Maw Cheng,[4] Deng-Sung Lin,[5] Frank Steglich,[1] Huiqiu Yuan,[1,6,†] Tai-Chang Chiang,[7] and Yang Liu[1,6,‡]

[1]*Center for Correlated Matter and Department of Physics, Zhejiang University, Hangzhou, China*
[2]*Department of Physics, Hangzhou Normal University, Hangzhou, China*
[3]*National Synchrotron Radiation Laboratory, University of Science and Technology of China, Hefei, China*
[4]*National Synchrotron Radiation Research Center, Hsinchu, Taiwan*
[5]*Department of Physics, National Tsinghua University, Hsinchu, Taiwan*
[6]*Collaborative Innovation Center for Advanced Microstructures, Nanjing University, Nanjing, China*
[7]*Department of Physics and Frederick Seitz Materials Research Laboratory, University of Illinois at Urbana-Champaign, Urbana, Illinois 61801, USA*

(Received 14 November 2017; revised manuscript received 15 July 2018; published 2 August 2018)

Here we report the evolution of bulk band structure and surface states in rare-earth monobismuthides with partially filled f shell. Utilizing synchrotron-based photoemission spectroscopy, we determined the three-dimensional bulk band structure and identified the bulk band inversions near the X points, which, according to the topological theory, could give rise to nontrivial band topology with an odd number of gapless topological surface states. Near the surface $\overline{\Gamma}$ point, no clear evidence for a predicted gapless topological surface state is observed due to its strong hybridization with the bulk bands. Near the $\overline{M}$ point, the two surface states, because of projections from two inequivalent bulk band inversions, interact and give rise to two peculiar sets of gapped surface states. The bulk band inversions and corresponding surface states can be tuned substantially by varying rare-earth elements, in good agreement with density-functional theory calculations assuming local f electrons. Our study therefore establishes rare-earth monobismuthides as an interesting class of materials possessing tunable electronic properties and magnetism, providing a promising platform to search for various properties in potentially correlated topological materials.

DOI: 10.1103/PhysRevB.98.085103

I. INTRODUCTION

The discovery of topological insulators has sparked tremendous research interest in condensed matter physics in the past decade [1–3]. The recent realization of topological semimetal, including Dirac and Weyl semimetals [4–12], has further advanced the field and significantly expanded the scope of topological materials. Although a majority of known topological materials are weakly correlated systems, searching for topological phases with strong electron correlations could yield a plethora of new quantum states and phenomena [13]. A well-known example of a correlated topological material is the topological Kondo insulator, e.g., SmB_6, where the hybridization between f and conduction electrons opens up an energy gap, which is smoothly connected by topological surface states (TSSs) [14–18]. Recently rare-earth (RE) monoantimonides/bismuthides, RESb/REBi, have attracted considerable research interest as potential candidates for correlated topological semimetals [19–22]. In LaSb/LaBi where no f electrons are present, it has been predicted that strong spin-orbit coupling (SOC) causes bulk band inversion, leading to nontrivial Z_2-topological invariant and TSSs [21]. If La is replaced with other RE elements with a partially filled f shell, a magnetic transition could occur at low temperature, which breaks time-reversal symmetry and potentially leads to novel topological phases with strong electronic correlations, such as Weyl fermions [23]. The simultaneous presence of nontrivial band topology and magnetism provides an opportunity to study the topological phase in a strongly correlated setting.

The electronic structure of RESb/REBi has been studied by first-principles calculations and angle-resolved photoemission spectroscopy (ARPES). Nontrivial band topology and TSSs have been observed experimentally in LaBi by ARPES measurements [24–28], while most RESb compounds are found to be topologically trivial without TSSs [29–33]. In this paper, we focus on the electronic structure of a few representative REBi compounds with different numbers of f electrons, including CeBi, PrBi, SmBi, and GdBi, in order to probe the evolution of bulk bands and possible TSSs. Since most previous ARPES studies of REBi are focused on LaBi [24–28] (with two recent papers on CeBi [20,34]), such a systematic study is crucial to reveal the role of f electrons and their influence on the electronic structure near the Fermi level.

II. EXPERIMENTAL AND COMPUTATIONAL DETAILS

Single crystals of REBi were grown using an indium flux method with a molar ratio of RE:Bi:In of 1:1:10. The raw

*ccao@hznu.edu.cn
†hqyuan@zju.edu.cn
‡yangliuphys@zju.edu.cn

 ©2018 American Physical Society

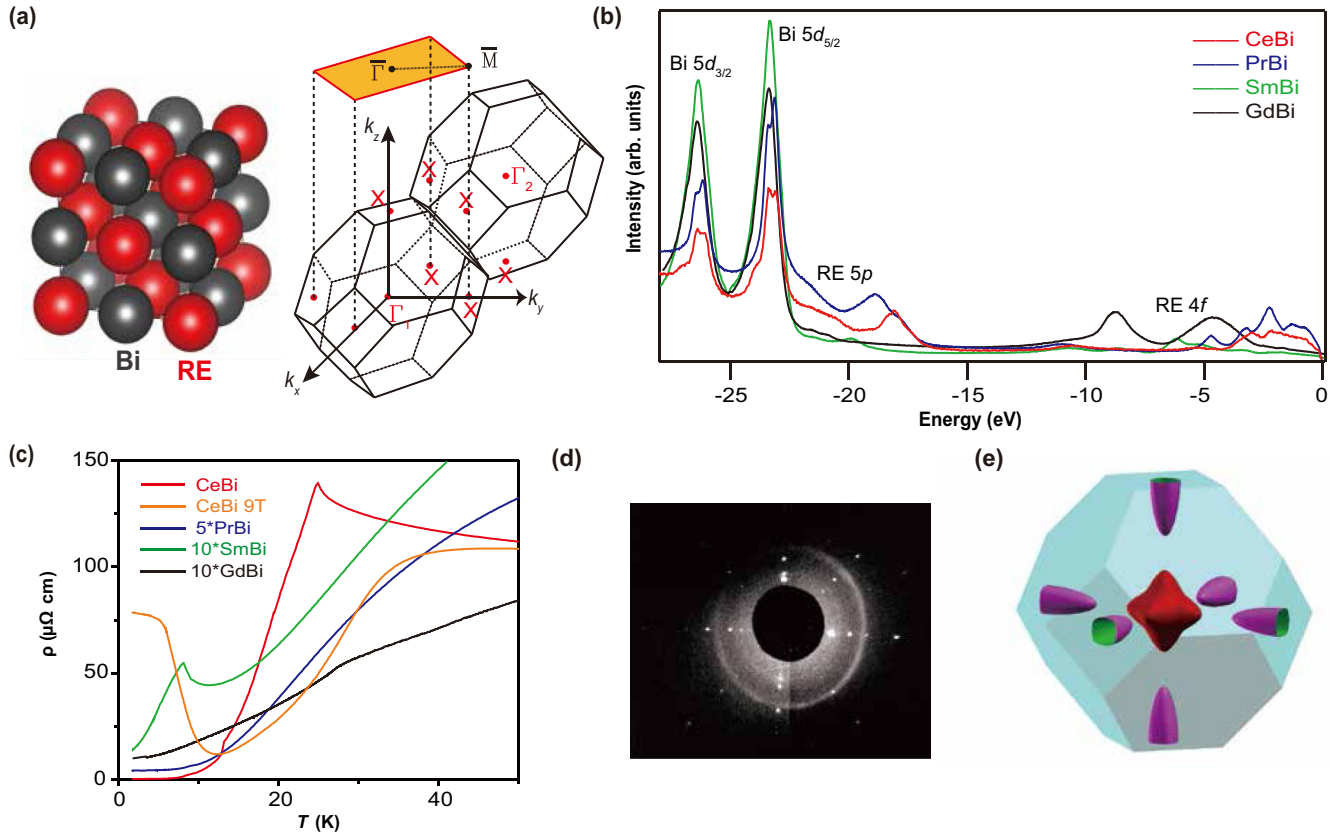

FIG. 1. Sample characterization of REBi. (a) Crystal structure (left) and its corresponding bulk and surface BZ (right) of REBi. (b) Momentum-integrated large-range energy scans for various REBi compounds. The spectrum for CeBi, PrBi was taken with 42-eV photons, while 54-eV photons were used for SmBi and GdBi. The small splitting of both the Bi $5d_{3/2}$ and $5d_{5/2}$ lines is caused by simultaneous contributions from surface and bulk Bi atoms due to the cleaved surface, and their relative ratio could be dependent on the photon energy. The spectra between -2 and -10 eV are dominated by RE $4f$ bands, which gradually move to deeper binding energies with heavier RE. (c) The resistivity vs temperature for all REBi compounds. The resistivity for CeBi under 9-T magnetic field is also displayed, showing its extremely large magnetoresistance. (d) A Laue image of SmBi indicating high-quality single crystal. (e) Three-dimensional FS for GdBi within the first BZ, typical for all REBi's.

materials were weighed and put into Al_2O_3 crucible, sealed in an evacuated quartz tube, and heated to 1100°C before cooling down slowly to 800 °C. The excessive indium was removed in a centrifuge. The typical size of the crystal is $2 \times 2 \times 2$ mm. After growth, the samples were characterized by Laue diffraction, magnetotransport, and thermodynamic measurements. Synchrotron-based ARPES measurements were carried out at BL13U beamline at National Synchrotron Radiation Lab (NSRL, China) and beamline 21B at Taiwan Light Source, both equipped with a R4000 electron energy analyzer. All ARPES spectra in this paper were taken at ∼30 K, i.e., the samples are in their paramagnetic phase. The typical energy resolution is ∼20 meV and the momentum resolution is typically 0.01 $Å^{-1}$. Constant energy contours are generated by rotating the sample in steps of 1° or 0.5° with respect to the vertical z axis (at NSRL). Large single crystals of ReBi were cleaved *in situ* in the ARPES chamber (base pressure $\sim 7 \times 10^{-11}$ Torr), resulting in a flat and shiny surface for the ARPES measurement. Because these samples are easily oxidized, all data presented in this paper were taken only within a few hours (<4 h) after a fresh cleave at low temperature. Sample aging is monitored regularly (by checking the reference scan) to ensure that the data presented in the paper reflect the intrinsic band structure of the materials.

Electronic structure calculations were performed using density functional theory (DFT) and a plane-wave basis projected augmented wave method, as implemented in the Vienna ab initio simulation package (VASP) [35]. The f electrons were treated as core electrons in all DFT calculations. An energy cutoff of 480 eV and $12 \times 12 \times 12$ gamma-centered k-mesh were employed to converge the calculation to 1 meV/atom. The spin-orbit coupling effect was considered using a second variational step. Since the Perdew-Burke-Ernzerhof (PBE) flavor of the generalized gradient approximation to the exchange-correlation functional is known to exaggerate the band inversion features [36], we have employed the modified Becke-Johnson (MBJ) potential to obtain better agreement with experiments [37]. For the PBE calculations, the surface states were obtained by using a 25-layer slab-model with 25-Å vacuum layer (PBE slab), whereas for the MBJ calculations, the surface states were obtained with the surface Green's function method (MBJ GF calculations) [38], assuming a semi-infinite slab. Slab calculations using the MBJ potential are difficult to perform at the moment, due to the nonconvergence problem.

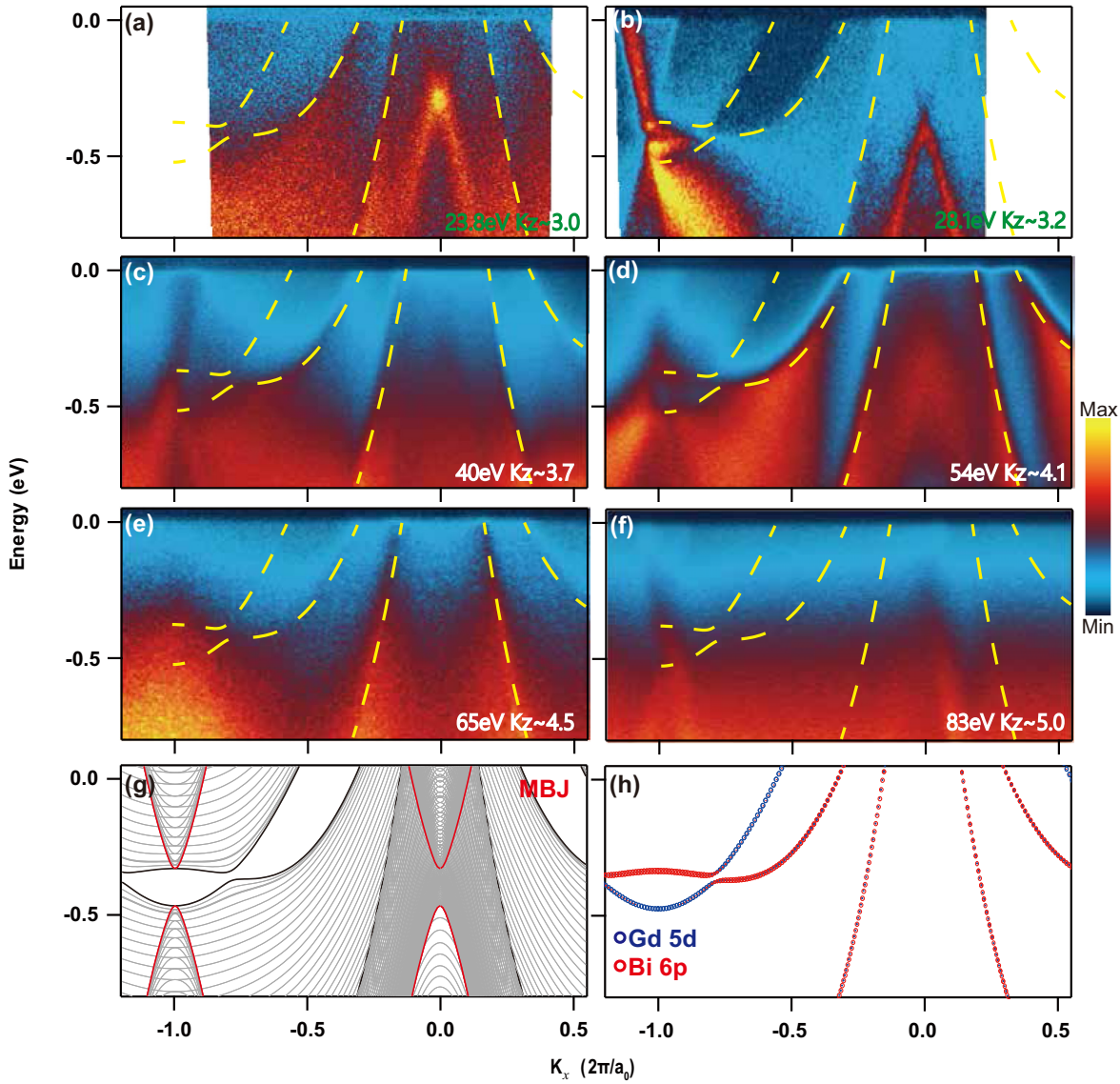

FIG. 2. Probing the three-dimensional band structure by photon-energy dependent ARPES, example of GdBi. (a)–(f) ARPES spectra of GdBi taken along the $\overline{\Gamma M}$ direction with various photon energies, in comparison with the projected bulk band calculation using the MBJ potential (g). The k_z values, indicated at the bottom right of the experimental data, are calculated based on the dipole transition model using an estimated inner potential of 14 eV. The dashed yellow curves on top of experimental data are the extracted dispersion relations of the bulk bands at $k_z = 0$ cut. The fact that they do not show a continuous change with photon energy indicates large k_z broadening in the photoemission process, which yields emission features dominated by the band edge ($k_z = 0$ or π cuts). The thick black (red) curves in (g) indicate $k_z = 0$ ($k_z = \pi$) cuts. (h) The band character for the $k_z = 0$ cut, highlighting the bulk band inversion between Gd $5d$ and Bi $6p$ bands near the $\overline{M}$ point.

III. RESULTS AND DISCUSSIONS

A. Sample characterization

REBi crystallizes in the simple rocksalt structure (face-centered-cubic) as shown in Fig. 1(a), where its bulk three-dimensional (3D) Brillouin zone (BZ) and projected 2D BZ, typically used for APRES analysis, are also shown. Since we work on the (001) surface in this paper, the bulk Γ and one X ($k_z = \pi$) point project onto 2D $\overline{\Gamma}$ point with $(k_x, k_y) = (0, 0)$, and two bulk symmetry-inequivalent X points (with $k_z = 0$ or π, respectively) project onto the same 2D $\overline{M}$ point with $(k_x, k_y) = (\sim 1\ \text{Å}^{-1}, 0)$. A momentum-integrated energy scan reveals sharp core levels, including Bi $5d$ (-26 eV and -23 eV), RE $5p$ (between -28 and -18 eV) and RE $4f$ (from -10 eV up to -2 eV) [Fig. 1(b)], confirming a good sample quality. The sample quality is further verified by the large residual resistivity ratio (typically over 100), as well as sharp Laue patterns, as shown in Figs. 1(c) and 1(d). An extremely large magnetoresistance (MR) was also observed [39], and an example is shown for CeBi with MR up to 2×10^4 % at 9 T and 2 K. Magnetic transitions take place at low temperature for many REBi's, due to partially filled $4f$ shells, which may overlap with the orbits of conduction electrons and develop long-range magnetic order. A well-known example is CeBi, where highly anisotropic magnetic orderings with a complex phase diagram occur at low temperature, accompanied by

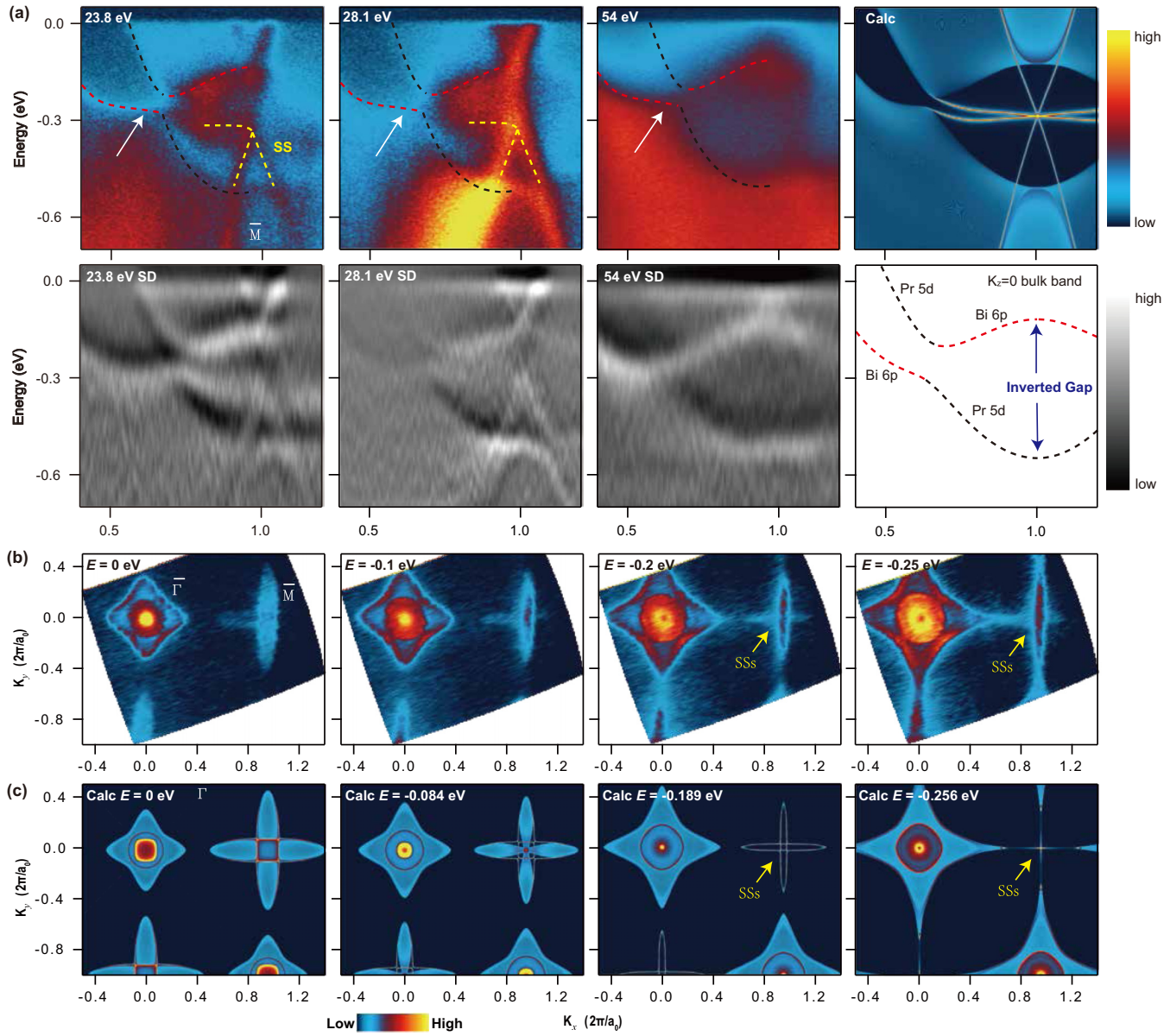

FIG. 3. Identifying bulk band inversion and associated SSs, using PrBi data as an example. (a) Upper row: ARPES data along the $\overline{\Gamma M}$ direction taken with different photon energies, compared with the calculation (the rightmost panel). The yellow, black, and red dashed curves indicate extracted SSs, bulk band edge of Pr $5d$ and Bi $6p$, respectively. The white arrows indicate the bulk band inversion point. In the calculation, the blue background indicates the bulk continuum and the SSs are shown as sharp lines lying within the inverted gap. Lower row: The corresponding second derivative of experimental data, together with the plot of bulk band character for $k_z = 0$ cut (the rightmost panel), which is directly relevant for bulk band inversion. (b) Experimental constant energy contours using 23.8-eV photons at $E = 0$, -0.18, -0.24, and -0.315 eV, which corresponds to the Fermi energy, the conduction band bottom, the bulk band inversion point, and the center point of SSs. (c) Theoretical constant energy contours, to be compared with (b). Thin lines at $E = -0.189$ and -0.256 eV maps correspond to SS contours centered at the $\overline{M}$ point. All calculations were performed using the MBJ GF method.

dramatic changes in transport and thermodynamic properties [40–43]. Although PrBi (non-Kramers f^2 configuration) stays in a paramagnetic phase at the lowest temperature, a magnetic transition takes place at low temperature for both SmBi (f^5) and GdBi (f^7). These magnetic transitions are evident in the resistivity data [Fig. 1(c)], where sharp change occurs near the antiferromagnetic (AFM) transition for CeBi ($T_N = 25$ K) and SmBi ($T_N = 9$ K), with peaklike features typical for AFM Kondo lattice systems [44]. For GdBi ($T_N \simeq 27$ K), the AFM transition shows up as a small kink in the resistivity. In this paper, we focus on the basic electronic structure of REBi in the high-temperature paramagnetic phase, where time-reversal symmetry is still preserved.

B. Bulk band inversion and surface states

In the paramagnetic phase, the calculated Fermi surface (FS) of bulk REBi consists of two hole pockets at the Γ point (Bi $6p$ orbitals) and one electron pocket at each X point (RE $5d$ orbitals), as illustrated in Fig. 1(e). Because

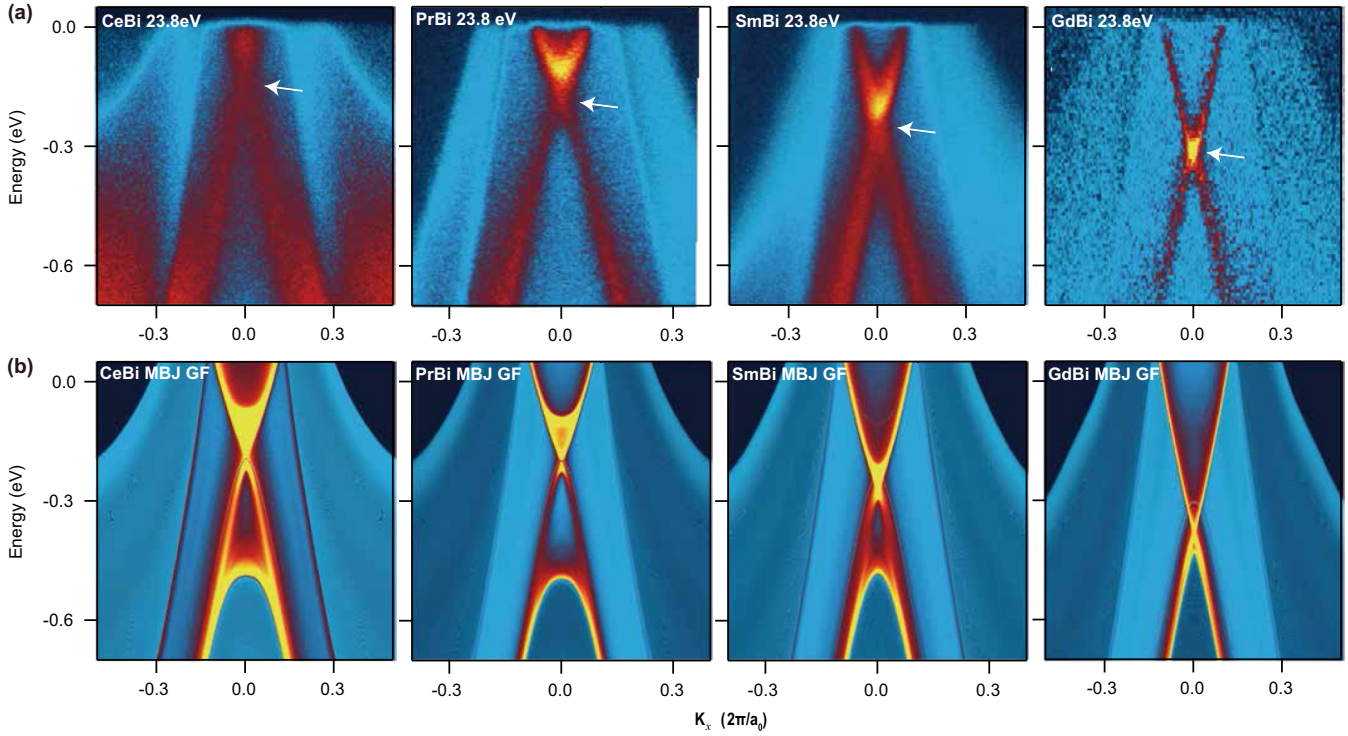

FIG. 4. ARPES spectra near the $\overline{\Gamma}$ point for CeBi, PrBi, SmBi, and GdBi, in comparison with theoretical calculations. (a) Experimental band dispersion near the $\overline{\Gamma}$ point taken at 23.8 eV. The white arrows indicate the crossing points of the conelike emission features. (b) Results from MBJ GF calculations, to compare with experiments.

of the three-dimensional nature of the band structure, we first performed a detailed photon energy dependence study to associate the APRES spectra with different k_z cuts; the example of GdBi is shown in Fig. 2. The projected bulk band structure, obtained by DFT calculations using the MBJ potential, is also shown for comparison. It is clear that the spectra under 83 eV is very close to the $k_z = \pi$ cut [thick red curves in the calculations in Fig. 2(g)], showing two cone-like structures at the $\overline{\Gamma}$ and $\overline{M}$ points, respectively. The 54 eV spectrum shows strong emission from hole bands near the $\overline{\Gamma}$ point and electron bands close to the $\overline{M}$ point, corresponding to the $k_z = 0$ cut [thick black curves in Fig. 2(g)]. Based on the photon energy vs k_z correspondence at these photon energies, one could estimate the inner potential to be $\simeq$14 eV, similar to previous results for LaBi [25]. We should mention that significant k_z broadening is present in REBi; as a result, the bulk bands do not move continuously with photon energy as one might expect for a bulk band under the standard dipole transition. For example, the bulk hole pockets at the $\overline{\Gamma}$ point are observed over a large photon energy range between the "expected" $k_z \sim 3\pi$ (23.8 eV) and $k_z \sim 4.5\pi$ (65 eV), and the bands show little movement with photon energy (cf. the dashed yellow curves). Such a discontinuous movement of bulk bands with photon energy can be attributed to a large k_z broadening, which has also been observed in other monopnictide systems, such as LaSb and CeSb [26,32,34]. The most likely cause for the large k_z broadening is the short photoelectron escape depth (5–10 Å) in the current experiment; indeed, soft x-ray ARPES in CeSb/CeBi has identified continuous movement of the bulk bands with photon energies, due to better bulk sensitivity (hence smaller k_z broadening) [34]. The large k_z broadening in the current photon energy range indicates that it is necessary to make careful comparisons between experiments and calculations to distinguish bulk bands and TSSs.

According to DFT calculations, bulk band inversion (between Bi $6p$ and RE $5d$ bands) takes place along ΓX direction, as indicated by Fig. 2(h), and leads to a nontrivial Z_2-topological invariant and TSSs [24]. Here, the Z_2-topological invariant can be evaluated by calculating the band parity of all occupied bands at all time-reversal invariant momentum points [45]. Although the definition of the Z_2-topological invariant was intended for a topological insulator with an absolute band gap, such a concept can be extended to semimetallic REBi, where a momentum-dependent partial band gap exists, separating the valence and conduction bands [12]. Detailed numerical calculations predict that REBi (with RE ranging from Ce to Gd) could possess a nontrivial Z_2 index and hence TSSs [46]. Since there are three X points in this calculation, the Z_2 index is dependent on the product of the parity of all occupied bands at X: If there is band inversion along the ΓX direction, the Z_2-topological invariant is nontrivial; otherwise, the system will be topologically trivial. This bulk band inversion is indeed observed in all compounds studied in this paper; an example for PrBi is shown in Fig. 3 (same for GdBi in Fig. 2). The bulk band inversion is best displayed under 54-eV photons [Fig. 3(a)], where the Pr $5d$ (black dashed curve) and Bi $6p$ (red dashed curve) bands become crossed and yield an inverted gap, in good agreement with the MBJ GF calculation (the rightmost panel). The emission intensity of the bulk bands does not show an obvious shift across the

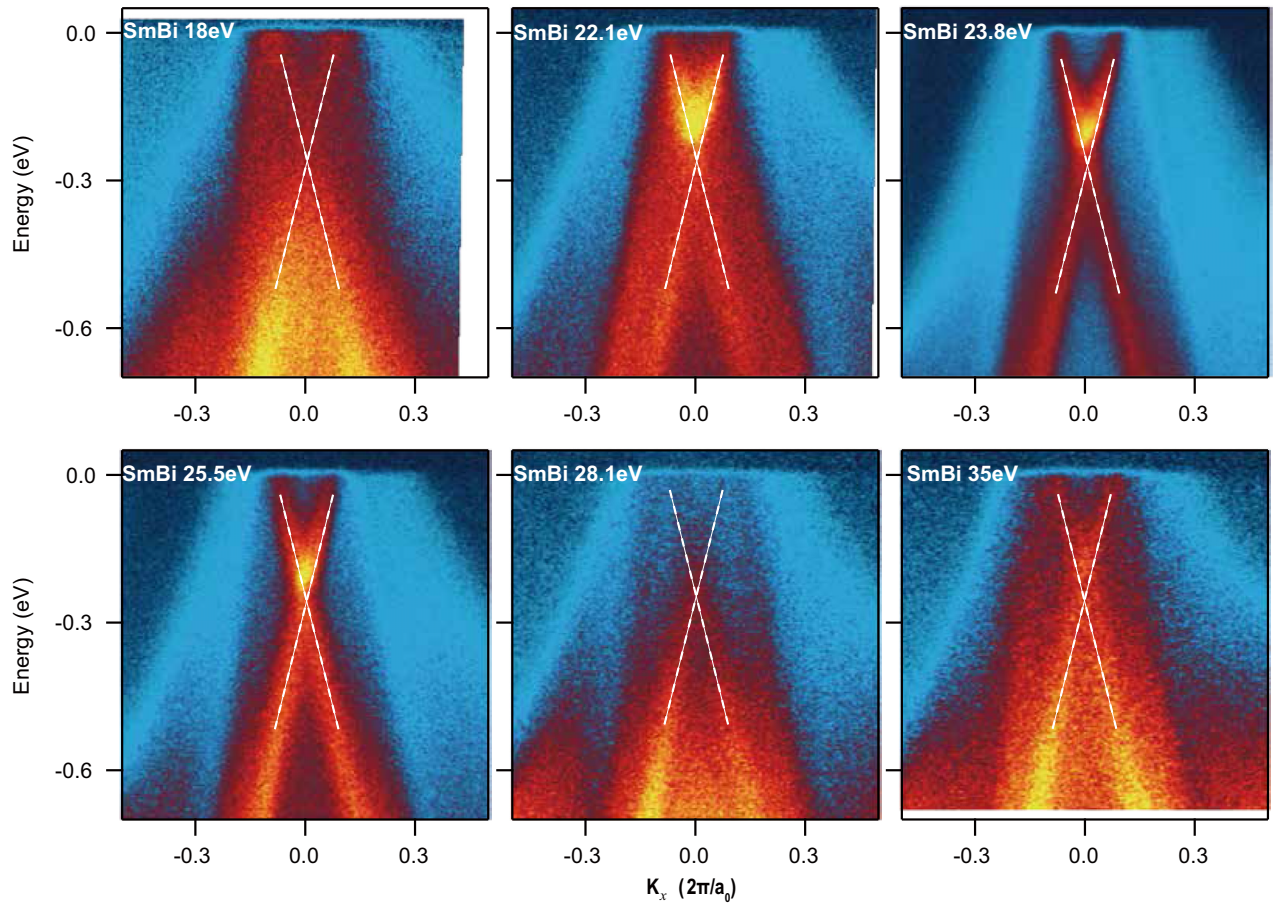

FIG. 5. Photon-energy-dependent ARPES spectra of SmBi near the $\overline{\Gamma}$ point, showing a conelike emission feature (denoted by the white dashed curves), which is visible over a wide photon energy range and does now show an obvious change with photon energy. One possible explanation for this conelike feature is the predicted gapless TSS, although it could be more naturally explained by the bulk bands near band inversion point, because of the large k_z broadening discussed in the paper.

inversion point, which seems strange in view of the changed orbital character. However, it is likely that the photoexcited final state plays an important role in the photoemission matrix element, which, together with the large k_z broadening, smears out the expected intensity shift across the inversion point.

In the MBJ GF calculation, two sets of gapless TSS Dirac cones would be expected at the $\overline{M}$ point due to the projection of two symmetry-inequivalent X points, which consists of linearly dispersive Dirac cones and relatively flat portions that smoothly connect to the bulk inversion point. In the experiments (23.8-and 28.1-eV data), we could only resolve the lower portion of the Dirac cone, while the upper part is somewhat diffuse and cannot be identified clearly. As we shall see later (Sec. III C), two predicted TSSs near the $\overline{M}$ point (based on projections of two bulk X points) actually interact with each other and give rise to two sets of gapped surface states (SSs). As these SSs disperse into the bulk band region, it gradually loses its surface character and merges into the bulk continuum. Although the SSs presumably share an in-plane orbital character that is similar to the bulk states, their detailed photon energy dependence seems to be obviously different, likely due to the difference in the z extent of the wave function (hence a different photoexcitaton cross section).

The experimental FS [Fig. 3(b)] at the $\overline{\Gamma}$ point consists of two hole pockets ($k_z = 0$) and one electron pocket ($k_z = \pi$), due to a large k_z broadening as mentioned earlier. Two elliptically shaped electron pockets, rotated 90° with respect to one another, can be observed at the $\overline{M}$ point, corresponding to $k_z = 0$ and π cuts, respectively. All bands at the FS are expected to derive from bulk states. Moving down in energy, the hole pockets expand and the electron pockets shrink; at the bulk band inversion point ($E \simeq -0.2$ eV), one begins to see significant spectral contributions from SSs near the $\overline{M}$ point, which exhibit an elliptical shape and eventually develop a continuous connection to bulk bands with cross-like features ($E \simeq -0.2$ eV). The highly anisotropic dispersion of the SSs is a direct manifestation of the bulk band structure. All these experimental observations are in good agreement with MBJ GF calculations [Fig. 3(c)]). Note that the MBJ GF calculations assume equal spectral contributions from all k_z's; the good agreement between ARPES results and MBJ GF calculations further confirms the large k_z broadening inherent in the photoemission process of REBi.

A Z_2-topological insulator is characterized by an odd number of gapless TSS(s), and, in the current case, it should theoretically correspond to a gapless TSS at the $\overline{\Gamma}$ point (due to the projection of a single X point). This predicted TSS stems

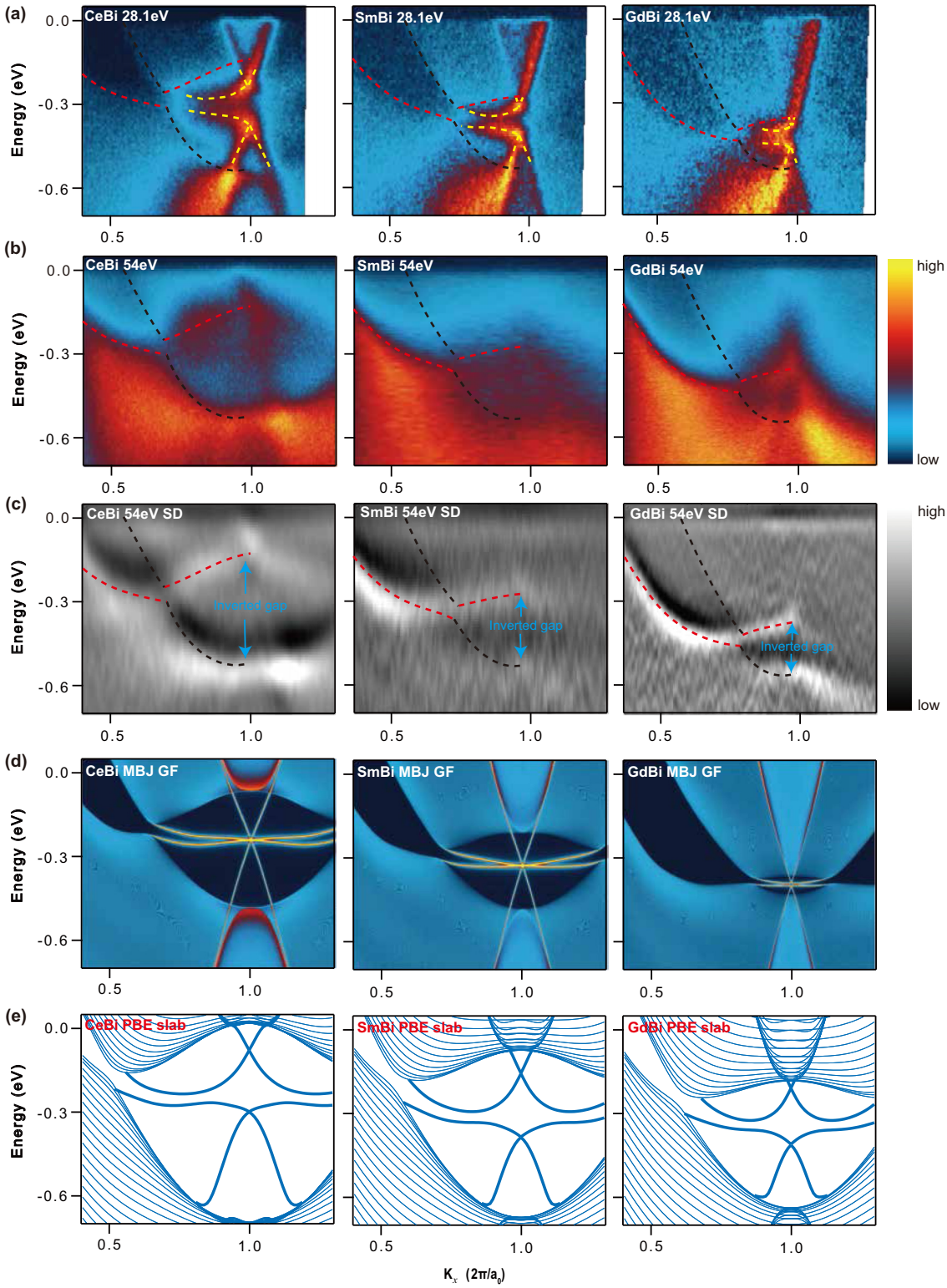

FIG. 6. Evolution of bulk band inversion and associated SSs in CeBi, SmBi, and GdBi, in comparison with theoretical calculations. (a),(b) Experimental band dispersion along $\overline{\Gamma}\overline{M}$ direction taken at two representative photon energies. (c) is the second derivative of the data taken at 54 eV. The yellow dashed lines are the extracted dispersion of the SSs, while the black (red) dashed lines indicate the bulk band edge of RE 5*d* (Bi 6*p*) band. The inverted bulk gap at the $\overline{M}$ point is indicated by cyan arrows in (c). (d),(e) Results from (d) MBJ GF calculations and (e) PBE slab calculations.

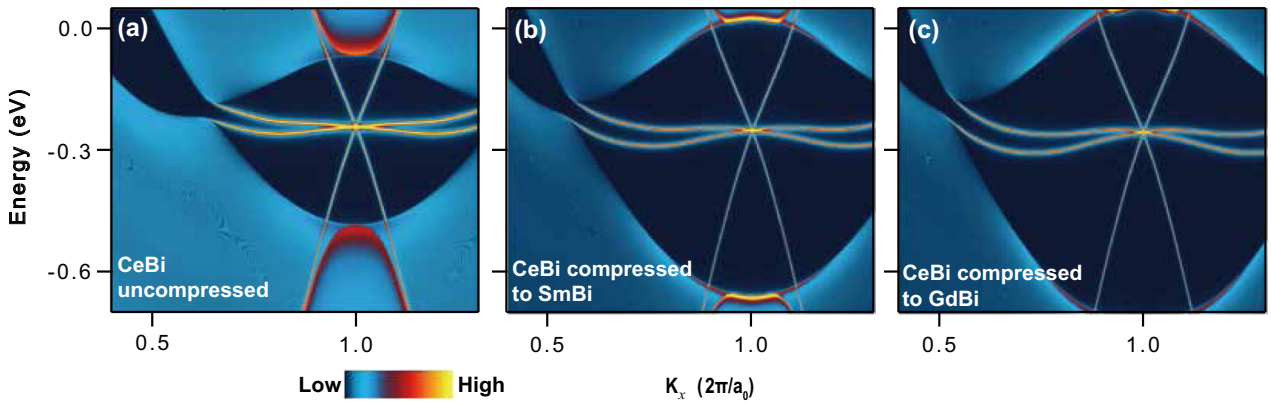

FIG. 7. Theoretical band structure of CeBi with various lattice constants, matched to those of bulk (a) CeBi, (b) SmBi, and (c) GdBi, mimicking the pure pressure effect for CeBi. We used the experimental lattice constants (a_0) of 6.505, 6.35, and 6.311 Å for CeBi, SmBi and GdBi, respectively. The calculations were performed using the MBJ GF method.

from the same bulk band inversion observed near the $\overline{M}$ point, except that it is now from the $k_z \sim \pi$ projection [see Fig. 1(a)]. The ARPES spectra near the $\overline{\Gamma}$ point for CeBi, PrBi, SmBi, and GdBi are summarized in Fig. 4(a). Indeed, a conelike feature can be observed near the $\overline{\Gamma}$ point for all compounds, which extends in a large energy range and forms a continuous dispersion across the valence band. In addition, this sharp conelike feature is present over a large photon energy range (see Fig. 5). Although these behaviors seem to be compatible with the theoretically expected gapless TSS, its dispersion with photon energy in some cases [e.g., in Figs. 2(a) and 2(b)] suggests that it is more likely due to the neighboring bulk states near $k_z \sim \pi$. We argue that due to the absence of a partial bulk gap near the $\overline{\Gamma}$ point, the originally gapless TSS hybridizes strongly with the neighboring bulk bands and therefore loses its surface character. This might be why this Dirac-cone-like feature could appear gapped in some cases [25,27], because of complete overlap with gapped bulk states. This also highlights the unique character of a semimetal with a Z_2-topological invariant: Even if the bulk topology predicts odd numbers of gapless TSS(s), some TSS(s) could hybridize strongly with neighboring bulk states and no longer survive as pure SSs.

C. Evolution of electronic structure with rare-earth elements

With heavier RE's, the conelike features near the $\overline{\Gamma}$ point move down in energy [see the white arrows in Fig. 4(a)], whereas the bulk hole bands show relatively little change, consistent with the MBJ GF calculations [Fig. 4(b)]. In the calculations, a bundle of bulk states piles up near the predicted TSS, which could give rise to visually "gapped Dirac cones" centered at the $\overline{\Gamma}$ point.

In Figs. 6(a)–6(c), we present the evolution of the bulk bands and associated SSs near the $\overline{M}$ point for CeBi, SmBi, and GdBi, respectively. Moving from Ce to Gd, we observe that the inverted bulk gap [denoted by cyan arrows in Fig. 6(c)] gradually shrinks and the band inversion region moves down in the energy, in good agreement with the MBJ GF calculations [Fig. 6(d)]. Interestingly, both experiments and calculations indicate that GdBi possesses a very small inverted gap and highly linear bulk bands, suggesting a possible topologically nontrivial-trivial phase transition when replacing Gd with a slightly heavier RE element. Specifically, DFT calculations have predicted that no bulk band inversion occurs for REBi with RE heavier than Dy [46], resulting in a topologically trivial phase. The large tunability of both bulk bands and SSs in REBi is quite different from the case of RESb, where the change of the electronic structure with RE replacement is much less pronounced [31].

Although the experimental bulk bands are in good agreement with MBJ GF calculations, the detailed dispersion of SSs near the $\overline{M}$ point differs. The experimentally extracted dispersions of SSs are highlighted by the yellow dashed lines in Fig. 6(a), which clearly show two cones with well-separated Dirac points, apparently different from the MBJ GF calculations [Fig. 6(d)]. The difference is probably due to the simplified treatment of surfaces in the GF calculations, which neglects the detailed surface conditions, particularly surface structural distortions and dangling bonds. This discrepancy could be solved by slab calculations that take into account realistic surface conditions, but such slab calculations using the MBJ potential are hampered by the nonconvergence problem in the practical calculation. To circumvent this problem, we present the results of slab calculations using the PBE potential in Fig. 6(e). Indeed, the results show two sets of vertically separated SSs, both of which consist of flat portions connecting to the band inversion point and V-shaped cones centered at the $\overline{M}$ point, in better agreement with the experimental data. Nevertheless, PBE slab calculations yield band inversions that are much larger than experiments, a well-known problem for DFT calculations using the PBE potential [47]. Note that the observed SSs are not real TSSs, since they are apparently gapped and connect to the valence band or conduction band separately, different from intrinsic TSSs that form a continuous connection between valence and conduction bands. Nevertheless, these SSs are thought to be intimately linked to a nontrivial band inversion near the X point, as no SS could be seen in the calculations of heavy REBi where no band inversion occurs [46]. A possible explanation is that a direct projection of two symmetry-inequivalent X points gives rise to two sets of originally gapless TSSs, which then interact and open up a gap, rendering two sets of trivial gapped SSs. The gap opening might be related to surface structural distortions, which act to reduce the dangling bonds at the surface and minimize the

surface energy. These SSs could also be interpreted in terms of classic Shockley-type SSs, which arise due to closings and openings of the local band gaps [48].

To understand the dependence of the electronic structure on the RE element, one needs to disentangle the effects of the varied proton/f-electron counting and simultaneous lattice compression. This insight would be useful to understand the pressure tuning of physical properties in REBi [49]. To simulate the pure lattice-pressure effect, we have calculated the electronic structure of CeBi with differing lattice constants, matched to bulk CeBi, SmBi, and GdBi, respectively (Fig. 7). Apparently, pure lattice compression enlarges the bulk gap inversion due to the stronger wave-function overlap, which is opposite to the experimental trend of replacing with heavier RE elements [Fig. 6(a)]. This indicates that the varied proton/f-electron counting plays a dominant role in tuning the electronic structure, which essentially changes the atomic and exchange potential that the valence/conduction electrons feel. Note that f electrons should be mostly local in the paramagnetic phase, yet they could not be simply considered as partially canceling the nuclei charge.

IV. CONCLUDING REMARKS

To conclude, we present ARPES measurements and comparisons with electronic structure calculations for REBi homologs, a class of materials possessing possibly nontrivial bulk band topology and strong electronic correlations below magnetic transitions. We identified the bulk band inversion, in excellent agreement with MBJ calculations. We did not observe a clear gapless TSS near the $\overline{\Gamma}$ point, probably due to strong mixing with neighboring bulk bands, while two of the originally gapless TSSs near the $\overline{M}$ point interact and yield a peculiar pair of gapped trivial SSs. The large variation of the electronic structure with RE elements provides an opportunity to tune the topological properties, while the presence of magnetism at low temperature sets the stage for exploring strongly correlated topological phases.

Our current results call for future studies to explore the effect of magnetism on the electronic structure at low temperature. Specifically, it would be important to track the change in the electronic structure across the magnetic transition and understand the role of the f electrons. It might also be interesting to reveal SSs under different magnetically ordered phases and search for different topological phases with broken time-reversal symmetry. Experimental efforts are currently under way to tackle these problems.

ACKNOWLEDGMENTS

This work is supported by National Key R&D Program of the MOST of China (Grants No. 2017YFA0303100, No. 2016YFA0300203, and No. 2014CB648400), National Science Foundation of China (Grants No. 11674280, No. 11274006, and No. U1632275), the Science Challenge Project of China (No. TZ2016004). T.C.C. acknowledges support from the US Department of Energy under Grant No. DE-FG02-07ER46383. We would like to thank Pengdong Wang, Dr. Chanyuen Chang for support and help during synchrotron ARPES measurements, and Prof. Fuchun Zhang, Prof. Haijun Zhang, and Prof. Stefan Kirschner for helpful discussions.

P.L., Z.W., and F.W. all contributed equally to this work.

[1] M. Z. Hasan and C. L. Kane, Rev. Mod. Phys. **82**, 3045 (2010).
[2] X.-L. Qi and S.-C. Zhang, Rev. Mod. Phys. **83**, 1057 (2011).
[3] M. König, S. Wiedmann, C. Brüne, A. Roth, H. Buhmann, L-W. Molenkamp, X.-L. Qi, and S.-C. Zhang, Science **318**, 766 (2007).
[4] Z. K. Liu, B. Zhou, Y. Zhang, Z.-J. Wang, H.-M. Weng, D. Prabhakaran, S.-K. Mo, Z.-X. Shen, Z. Fang, X. Dai, Z. Hussain, and Y.-L. Chen, Science **343**, 864 (2014).
[5] S.-Y. Xu, C. Liu, S. K. Kushwaha, R. Sankar, J. W. Krizan, I. Belopolski, M. Neupane, G. Bian, N. Alidoust, T.-R. Chang. H.-R. Jeng, C.-Y. Huang, W.-F. Tsai, H. Lin, P.-P. Shibayev, F.-C. Chou, R.-J. Cava, and M. Zahid Hasan, Science **347**, 294 (2015).
[6] X. Wan, A. M. Turner, A. Vishwanath, and S. Y. Savrasov, Phys. Rev. B **83**, 205101 (2011).
[7] S.-M. Huang, S.-Y. Xu, I. Belopolski, C.-C. Lee, G.-Q. Chang, B.-K. Wang, N. Alidoust, G. Bian, M. Neupane, C.-L. Zhang, S. Jia, A. Bansil, and M. Zahid Hassan, Nat. Commun. **6**, 7373 (2015).
[8] H. Weng, C. Fang, Z. Fang, B. A. Bernevig, and X. Dai, Phys. Rev. X **5**, 011029 (2015).
[9] L. X. Yang, Z. K. Liu, Y. Sun, H. Peng, H. F. Yang, T. Zhang, Y. F. Guo, M. Rahn, D. Prabhakaran, Z. Hussain, S.-K. Mo, C. Felser, B. Yan, and Y. L. Chen, Nat. Phys. **11**, 728 (2015).
[10] B. Q. Lv, H. M. Weng, B. B. Fu, X. P. Wang, H. Miao, J. Ma, P. Richard, X. C. Huang, L. X. Zhao, G. F. Chen, Z. Fang, X. Dai, T. Qian, and H. Ding, Phys. Rev. X **5**, 031013 (2015).
[11] S.-Y. Xu, I. Belopolski, N. Alidoust, M. Neupane, G. Bian, C.-L. Zhang, R. Sankar, G.-Q. Chang, Z.-J. Yuan, C.-C. Lee, S.-M. Huang, H. Zheng, J. Ma, D. S. Sanchez, B.-K. Wang, A. Bansil, F.-C. Chou, P. P. Shibayev, H. Lin, S. Jia, and M. Zahid Hassan, Science **349**, 613 (2015).
[12] H. Weng, X. Dai, and Z. Fang, J. Phys.: Condens. Matter **28**, 303001 (2016).
[13] X. Zhang, H.-J. Zhang, C. Felser, and S.-C. Zhang, Science **335**, 1464 (2012).
[14] M. Dzero, K. Sun, V. Galitski, and P. Coleman, Phys. Rev. Lett. **104**, 106408 (2010).
[15] X.-H. Zhang, N. P. Butch, P. Syers, S. Ziemak, R. L. Greene, and J. Paglione, Phys. Rev. X **3**, 011011 (2013).
[16] N. Xu, X. Shi, P. K. Biswas, C. E. Matt, R. S. Dhaka, Y. Huang, N. C. Plumb, M. Radović, J. H. Dil, E. Pomjakushina, K. Conder, A. Amato, Z. Salman, D. M. Paul, J. Mesot, H. Ding, and M. Shi, Phys. Rev. B **88**, 121102(R) (2013).
[17] M. Neupane, N. Alidoust, S.-Y. Xu, T. Kondo, Y. Ishida, D. J. Kim, C. Liu, I. Belopolski, Y. J. Jo, T.-R. Chang, H.-T. Jeng, T. Durakiewicz, L. Balicas, H. Lin, A. Bansil, S. Shin, Z. Fisk, and M. Z. Hassan, Nat. Commun. **4**, 2991 (2013).

[18] J. Jiang, S. Li, T. Zhang, Z. Sun, F. Chen, Z. R. Ye, M. Xu, Q. Q. Ge, S. Y. Tan, X. H. Niu, M. Xia, B. P. Xie, Y. F. Li, X. H. Chen, H. H. Wen, and D. L. Feng, Nat. Commun. **4**, 3010 (2013)

[19] F. F. Tafti, Q. D. Gibson, S. K. Kushwaha, N. Haldolaarachchige, and R. J. Cava, Nat. Phys. **12**, 272 (2015).

[20] N. Alidoust, A. Alexandradinata, S.-Y. Xu, I. Belopolski, S. K. Kushwaha, M.-G. Zeng, M. Neupane, G. Bian, C. Liu, D. S. Sanchez, P. P. Shibayev, H. Zheng, L. Fu, A. Bansil, H. Lin, R. J. Cava, and M. Z. Hassan, arXiv:1604.08571.

[21] M. Zeng, C. Fang, G.-q. Chang, Y.-A. Chen, T. Hsieh, A. Bansil, H. Lin, and L. Fu, arXiv:1504.03492.

[22] S. Jang, R. Kealhofer, C. John, S. Doyle, J. Hong, J. H. Shim, Q. Si, O. Erten, J. D. Denlinger, and J. G. Analytis, arXiv:1712.05817.

[23] C. Y. Guo, C. Cao, M. Smidman, F. Wu, Y.-J. Zhang, F. Steglich, F.-C. Zhang, and H. Q. Yuan, npj Quantum Mater. **2**, 39 (2017).

[24] J. Nayak, S.-C. Wu, N. Kumar, C. Shekhar, S. Singh, J. Fink, E. Rienks, G. H. Fecher, S. Parkin, B. Yan, and C. Felser, Nat. Commun. **8**, 13942 (2016).

[25] R. Lou, B.-B. Fu, Q. N. Xu, P.-J. Guo, L.-Y. Kong, L.-K. Zeng, J.-Z. Ma, P. Richard, C. Fang, Y.-B. Huang, S.-S. Sun, Q. Wang, L. Wang, Y.-G. Shi, H.C. Lei, K. Liu, H. M. Weng, T. Qian, H. Ding, and S.-C. Wang, Phys. Rev. B **95**, 115140 (2017).

[26] X. H. Niu, D. F. Xu, Y. H. Bai, Q. Song, X. P. Shen, B. P. Xie, Z. Sun, Y. B. Huang, D. C. Peets, and D. L. Feng, Phys. Rev. B **94**, 165163 (2016).

[27] Y. Wu, T. Kong, L.-L. Wang, D. D. Johnson, D.-X. Mou, L. Huang, B. Schrunk, S. L. Bud'ko, P. C. Canfield, and A. Kaminski, Phys. Rev. B **94**, 081108(R) (2016).

[28] B. Feng, J. Cao, M. Yang, Y. Feng, S. Wu, B. Fu, M. Arta, K. Miyamoto, S. He, K. Shimada, Y. Shi, T. Okuda, and Y.-G. Yao, Phys. Rev. B **97**, 155153 (2018).

[29] L.-K. Zeng, R. Lou, D.-S. Wu, Q. N. Xu, P.-J. Guo, L.-Y. Kong, Y.-G. Zhong, J.-Z. Ma, B.-B. Fu, P. Richard, P. Wang, G. T. Liu, L. Lu, Y.-B. Huang, C. Fang, S.-S. Sun, Q. Wang, L. Wang, Y.-G. Shi, H. M. Weng, H.-C. Lei, K. Liu, S.-C. Wang, T. Qian, J.-L. Luo, and H. Ding, Phys. Rev. Lett. **117**, 127204 (2016).

[30] J. He, C.-F. Zhang, N. J. Ghimire, T. Liang, C.-J. Jia, J. Jiang, S.-J. Tang, S. Chen, Y. He, S.-K. Mo, C. C. Hwang, M. Hashimoto, D. H. Lu, B. Moritz, T. P. Deveraux, Y. L. Chen, J. F. Mitchell, and Z.-X. Shen, Phys. Rev. Lett. **117**, 267201 (2016).

[31] Y. Wu, Y. Lee, T. Kong, D.-X. Mou, R. Jiang, L. Huang, S. L. Bud'ko, P. C. Canfield, and A. Kaminski, Phys. Rev. B **96**, 035134 (2017).

[32] H. Oinuma, S. Souma, D. Takane, T. Nakamura, K. Nakayama, T. Mitsuhashi, K. Horiba, H. Kumigashira, M. Yoshida, A. Ochiai, T. Takahashi, and T. Sato, Phys. Rev. B **96**, 041120(R) (2017).

[33] M. Neupane, M. M. Hosen, I. Belopolski, N. Wakeham, K. Dimitri, N. Dhakal, J.-X. Zhu, M. Z. Hasan, E. D. Bauer, and F. Ronning, J. Phys.: Condens. Matter **28**, 23LT02 (2016).

[34] K. Kuroda, M. Ochi, H. S. Suzuki, M. Hirayama, R. Noguchi, C. Bareille, S. Akebi, S. Kunisada, T. Muro, M. D. Watson, H. Kitazawa, Y. Haga, T. K. Kim, M. Hoesch, S. Shin, R. Arita, and T. Kondo, Phys. Rev. Lett. **120**, 086402 (2018).

[35] G. Kresse and J. Hafner, Phys. Rev. B **47**, 558 (1993).

[36] J. P. Perdew, K. Burke, and M. Ernzerhof, Phys. Rev. Lett. **77**, 3865 (1996).

[37] F. Tran and P. Blaha, Phys. Rev. Lett. **102**, 226401 (2009).

[38] M. P. L. Sancho, J. M. L. Sancho, J. M. L. Sancho, and J. Rubio, J. Phys. F **15**, 851 (1985).

[39] F.-F. Tafti, Q. Gibson, S. Kushwaha, J. W. Krizan, N. Haldolaarachchige, and R. J. Cava, Proc. Natl. Acad. Sci. **113**, E3475 (2016).

[40] F. Hulliger, M. Landolt, H. R. Ott, and R. Schmelczer, J. Low Temp. Phys. **20**, 269 (1975).

[41] H. Bartholin, D. Florence, Tcheng-Si Wang, and O. Vogt, Phys. Status Solidi **24**, 631 (1974).

[42] H. Bartholin, P. Burlet, S. Quezel, J. Rossat-Mignod, and O. Vogt, J. Phys. (Paris), Colloq. **40**, C5-130 (1979).

[43] H. Takahashi and T. Kasuya, J. Phys. C: Solid State Phys. **18**, 2697 (1985).

[44] P. Coleman, *Handbook of Magnetism and Advanced Magnetic Materials* (Wiley, New York, 2007), Vol. 1, pp. 95–148.

[45] L. Fu and C. L. Kane, Phys. Rev. B **76**, 045302 (2007).

[46] X. Duan, F. Wu, J. Chen, P. Zhang, Y. Liu, H. Yuan, and C. Cao, arXiv:1802.04554.

[47] P.-J. Guo, H.-C. Yang, B.-J. Zhang, K. Liu, and Z.-Y. Lu, Phys. Rev. B **93**, 235142 (2016).

[48] W. Shockley, Phys. Rev. **56**, 317 (1939).

[49] F. F. Tafti, M. S. Torikachvili, R. L. Stillwell, B. Baer, E. Stavrou, S. T. Weir, Y. K. Vohra, H.-Y. Yang, E. F. McDonnell, S. K. Kushwaha, Q. D. Gibson, R. J. Cava, and J. R. Jeffries, Phys. Rev. B **95**, 014507 (2017).

nature COMMUNICATIONS

ARTICLE

Received 7 Jul 2013 | Accepted 26 Nov 2013 | Published 18 Dec 2013

DOI: 10.1038/ncomms4010 OPEN

Observation of possible topological in-gap surface states in the Kondo insulator SmB_6 by photoemission

J. Jiang[1,*], S. Li[2,*], T. Zhang[1,*], Z. Sun[3,4], F. Chen[5], Z.R. Ye[1], M. Xu[1], Q.Q. Ge[1], S.Y. Tan[1], X.H. Niu[1], M. Xia[1], B.P. Xie[1], Y.F. Li[2], X.H. Chen[3,5], H.H. Wen[2] & D.L. Feng[1]

SmB_6, a well-known Kondo insulator, exhibits a transport anomaly at low temperature. This anomaly is usually attributed to states within the hybridization gap. Recent theoretical work and transport measurements suggest that these in-gap states could be ascribed to topological surface states, which would make SmB_6 the first realization of topological Kondo insulator. Here by performing angle-resolved photoemission spectroscopy experiments, we directly observe several dispersive states within the hybridization gap of SmB_6. These states show negligible k_z dependence, which indicates their surface origin. Furthermore, we perform photoemission circular dichroism experiments, which suggest that the in-gap states possess chirality of the orbital angular momentum. These states vanish simultaneously with the hybridization gap at around 150 K. Together, these observations suggest the possible topological origin of the in-gap states.

[1] State Key Laboratory of Surface Physics, Department of Physics, and Advanced Materials Laboratory, Fudan University, Shanghai 200433, China. [2] National Laboratory of Solid State Microstructures and Department of Physics, Nanjing University, Nanjing 210093, China. [3] Department of Physics, University of Science and Technology of China, Hefei 230026, China. [4] National Synchrotron Radiation Laboratory, University of Science and Technology of China, Hefei 230029, China. [5] Hefei National Laboratory for Physical Science at Microscale, University of Science and Technology of China, Hefei 230026, China. * These authors contributed equally to this work. Correspondence and requests for materials should be addressed to D.L.F. (email: dlfeng@fudan.edu.cn).

© 2013 Macmillan Publishers Limited. All rights reserved.

Kondo insulators (KIs) or heavy-fermion semiconductors[1–3] are exotic materials with strong electron correlations, in which the localized *4f* electrons give rise to novel ground states. SmB_6 is a well-known KI. At high temperature, the many-body interactions between the local spins of Sm ions and conduction electrons (the Kondo screening) are weak, and the system is a correlated metal. With decreasing temperature, an energy gap develops due to the hybridization of *4f* bands and conduction *5d* bands[1–3], featured by a rapidly rising resistance. However, there is a long-standing puzzle: its resistivity does not diverge but saturates at temperatures below 4 K (refs 4–6). The residual conductivity was attributed to some in-gap states, evidenced by optical, neutron scattering, specific heat and angle-resolved photoemission spectroscopy (ARPES) experiments[7–10]. Although various models have been proposed to address the in-gap states[5,11], their exact nature remains illusive after decades of studies.

Recently, the novel concept of topological KI (TKI) may shed new light on the in-gap states in SmB_6 (refs 12,13). In the so-called topological insulator (TI) such as Bi_2Se_3 or Bi_2Te_3 (refs 14,15), there will be surface states that are protected by band topology from impurities that do not break time-reversal symmetry. Although the usual TIs are defined in weakly interacting systems, KIs with strong correlations can also be topologically classified. A topologically non-trivial KI could be realized by strong spin-orbit coupling associated with a hybridization band gap[12,13]. If SmB_6 is a TKI as predicted[12,13,16,17], there will be surface states that naturally explains the origin of in-gap states and the residual conductivity. In particular, unlike traditional TI materials in which surface transport was usually concealed by the defect-induced bulk carriers, SmB_6 seems to possess a true insulating bulk that will make it a promising candidate material for future spintronics applications[18]. Several recent experiments have observed pronounced surface-dominating transport in SmB_6 (refs 10,18–21) suggesting the TKI scenario. However, direct electronic structure evidences for these potential topological surface states are highly demanded for the understanding of their exact nature.

In this letter we present an ARPES study of SmB_6 single crystals. We observe several bands within the hybridization gap of SmB_6, which show negligible k_z dependence, indicative of their surface origin. Furthermore, the photoemission circular dichroism (CD) of these in-gap states suggests the chirality of the orbital angular momentum (OAM), and these states vanish simultaneously with the hybridization gap around 150 K. Our results thus strongly suggest their possible topological origin.

Results

Sample characterization and valence band structure. Sample preparation and experimental details are described in the Methods section. Figure 1a shows the powder X-ray diffraction pattern of SmB_6 taken after grinding the single crystals into powder. No evident secondary phase is observed, showing the high quality of the crystals. The resistivity of our SmB_6 sample exhibits a sharp increase below 50 K and starts to saturate below 5 K (Fig. 1b), similar to previous reports[4–6]. As shown in Fig. 1b,c, magnetoresistance is clearly present, which is negative below ~20 K and positive at higher temperatures. The negative magnetoresistance can be understood in the context of Kondo effect, where the Kondo singlet will be partially broken by the magnetic field, which releases the localized *d*-band electrons and lowers the resistivity. In contrast, the positive magnetoresistance at high temperatures might be induced by the orbital scattering effect. Figure 1d shows the low-energy electron diffraction (LEED) pattern of the cleaved surface. Clean 1×1 pattern of the (001) surface is observed. The bulk and projected Brillouin zones of the (001) surface are shown in Fig. 1e.

The photoemission intensities measured along $\overline{\Gamma}$–$\overline{X}$ and $\overline{X}$–$\overline{M}$ directions over a large energy scale are presented in Fig. 2a,b. Three flat bands can be observed at 18, 150 and 950 meV below the Fermi energy (E_F), as marked in the integrated energy distribution curves (EDCs). They are the $^6H_{5/2}$, $^6H_{7/2}$ and ^6F multiplets of the Sm^{2+} $4f^6 \rightarrow 4f^5$ final state, respectively[10,22]. In addition, there is a highly dispersive band centred at $\overline{X}$ (dashed line). In previous ARPES studies[22], it was ascribed to the bulk *5d* band based on the band calculations[23].

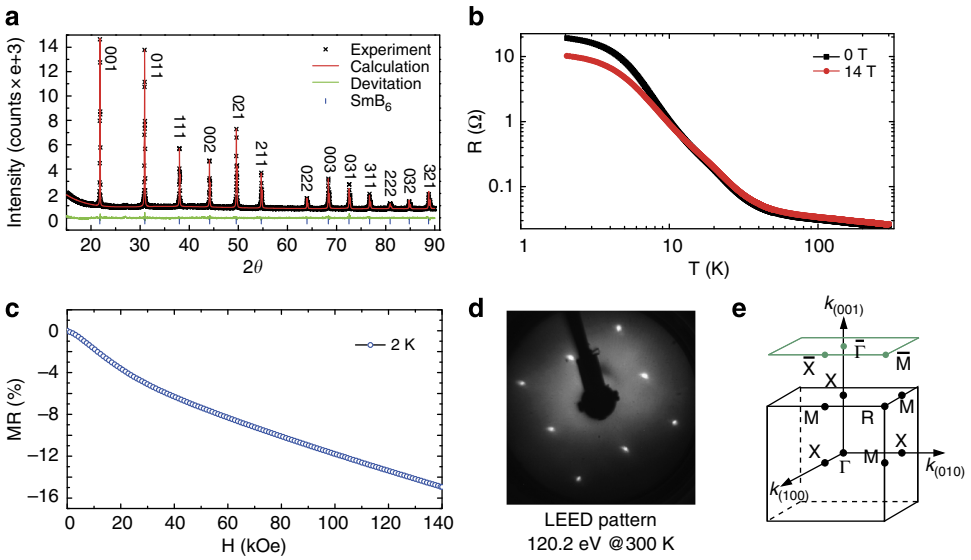

Figure 1 | SmB_6 sample characterization. (**a**) Powder X-ray diffraction pattern of an SmB_6 crystal. Solid line is the Rietveld fitting using the TOPAS software. The s.d. is negligible. (**b**) The temperature dependence of resistance at zero field and 14 T. A negative magnetoresistance is observed in the low temperature region, while it becomes positive in the high temperature region. (**c**) The magnetoresistance of SmB_6 taken at 2 K. A negative magnetoresistance is obvious here. (**d**) LEED pattern of the cleaved SmB_6 (001) surface. Bright spots in square lattice reflect the pristine 1×1 surface, with a lattice constant of 4.13 Å. (**e**) Bulk and surface projected Brillouin zone of SmB_6 and the high symmetry points.

© 2013 Macmillan Publishers Limited. All rights reserved.

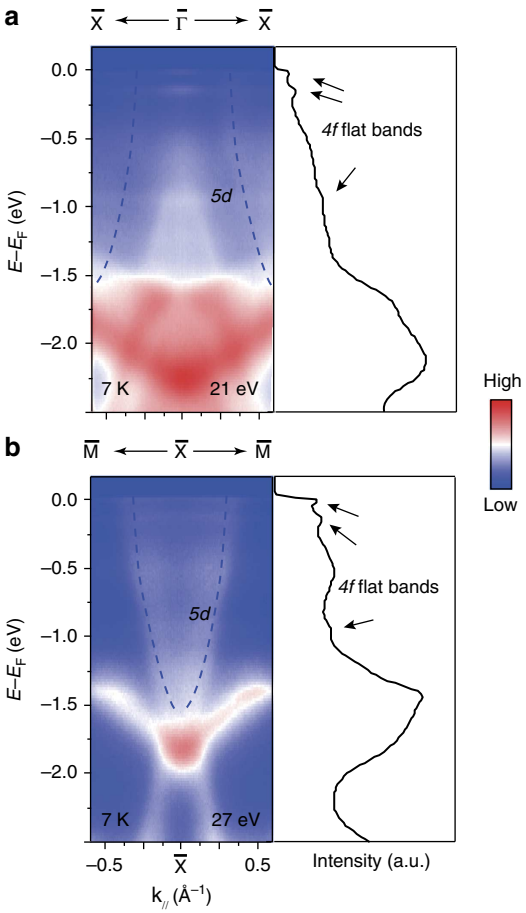

Figure 2 | Valence band structure of SmB_6. (**a**,**b**) Left panel: large energy scale photoemission intensity plot along the $\overline{\Gamma}$-$\overline{X}$ and $\overline{X}$-$\overline{M}$ directions, respectively. Right panel: integrated EDCs to highlight the positions of the flat *4f* bands as marked by the arrows. Dashed lines in panels **a** and **b** indicate the Sm *5d* band that crosses E_F at high temperatures. Data were taken at 7 K with 21 and 27 eV photons, respectively, at Stanford Synchrotron Radiation Lightsource.

Dispersive in-gap states around $\overline{\Gamma}$ and $\overline{X}$. To search for the in-gap states in SmB_6, the photoemission intensity at E_F is collected over the surface projected Brillouin zone (Fig. 3a). Data were taken at 8 K, well into the KI phase. Indeed, four large oval-shaped Fermi surfaces are clearly observed around $\overline{X}$, whose total area covers about 32.7% of the projected two-dimensional Brillouin zone, together with some spectral weight around $\overline{\Gamma}$. In the second Brillouin zone, the Fermi surface contour around $\overline{X}$ is weak while the spectral weight around $\overline{\Gamma}$ is much enhanced probably because of the matrix element effects of the photoemission process. The nature of these states can be further revealed in their dispersions. In Fig. 3b, we show the photoemission intensity plot over a larger energy scale along cut #1 across $\overline{X}$. The aforementioned *5d*-like band is marked as δ, and the band between the two flat *4f* bands is referred to as β. More details of the near-E_F states and the hybridization gap are further illustrated in Fig. 3c. Here the hybridization gap is manifested by the suppressed spectral weight between E_F and the $^6H_{5/2}$ *4f* band at -18 meV (referred to as ϕ). However, there is an in-gap dispersive band centred at $\overline{X}$ (referred to as α), which gives the large oval-shaped Fermi surface as shown in Fig. 3a. The dispersion of α is clearly visible in the momentum distribution curves (MDCs) in Fig. 3d as well, with Fermi crossings at ± 0.29 Å^{-1}. The band becomes obscure when it crosses ϕ and disappears below -30 meV. The photoemission intensity along a cut across $\overline{\Gamma}$ is shown in Fig. 3e, where the weak feature located at $\overline{\Gamma}$ exhibits an electron-like band dispersion as further illustrated by their MDCs in Fig. 3f. This is more readily visible in the second Brillouin zone as shown in Fig. 3g,h. This band (referred to as γ) gives the tiny central electron pocket with a Fermi momentum of ~ 0.09 Å^{-1} in Fig. 3a. Its area is just about 1.1% of the projected two-dimensional Brillouin zone. The bright spot on band ϕ at $\overline{\Gamma}$ could be attributed to its crossing with γ, and the crossing of the two γ branches is estimated to occur at 23 ± 3 meV. Furthermore, an oval-shaped Fermi surface α' can be observed around $\overline{\Gamma}$ in the 2nd Brillouin zone, which shows almost the same size as the α-Fermi surface around $\overline{X}$, although it appears weaker in the 1st Brillouin zone. Its twofold symmetry and size indicate that it is most likely to be the shadow Fermi surface from the umklapp scattering of the α-Fermi surface around $\overline{X}$ owing to the existence of a 1×2 surface reconstruction in this sample as reported in ref. 10 before. However, the superstructure spot of such a reconstruction is missing in the LEED pattern of our samples (Fig. 1d). Probably, it is too weak for the sensitivity of our LEED apparatus.

***k_z* dependence of the electronic structure.** Since the bulk SmB_6 is an insulator based on the transport data and calculations, the in-gap states α and γ should be some metallic surface states. To further illustrate this, we varied photon energies to reveal the k_z dependence of the electronic structure. The photoemission intensity distribution across $\overline{X}$ taken with various photon energies are presented in Fig. 4a. The photon energies we used cover a full k_z period in the extended Brillouin zone (Fig. 4e). The intensity distributions do not show any noticeable k_z dependence. In the corresponding MDC's shown in Fig. 4b, we tracked the dispersion of the α band taken with 25 eV photons and overlaid it on the data taken with other photon energies, which clearly show that the dispersions and Fermi crossings of α are k_z independent. This behaviour indicates the surface origin of the α pockets. However, in addition, one could observe a shoulder feature that does show some photon energy dependence, which thus might be contributed by a bulk state. Furthermore, Fig. 4c shows the photoemission intensity distributions taken with various photon energies over a large energy scale across $\overline{X}$. Since k_x, k_y and k_z are equivalent in a cubic compound, the bulk *5d* bands are expected to have similar fast dispersions along k_z as those in k_x and k_y directions. However, at the first sight, the *5d*-like fast dispersive bands together with others do not show strong k_z dependence, for one can notice that the envelope of the photoemission intensity in Fig. 4c appears to be independent of the photon energies. Nevertheless, the bright interior of the intensity envelope for 29 and 31 eV data is a typical consequence of the projection of intensities from different k_z due to the poor k_z resolution of ARPES[24]. As is further illustrated by the broad MDCs taken at -500 meV around $\overline{X}$ in Fig. 4d, the finite k_z resolution of ARPES spectral weight smears out the intensity distribution for the *5d* band with a strong k_z dispersion. Combining these observations, we could conclude that the α band probably contains both surface and bulk contributions, while the β and δ bands are most probably originated from the bulk *5d* band.

CD of the electronic structure. To study whether the surface states are topologically non-trivial or not, the chirality of their spin (**S**) and OAM shall be examined. This is another remarkable hallmark of the topological surface state: both the spin and OAM are interlocked and rotate with the electron momentum (**k**) and, their sum, the total angular momentum **J**, is a good quantum

© 2013 Macmillan Publishers Limited. All rights reserved.

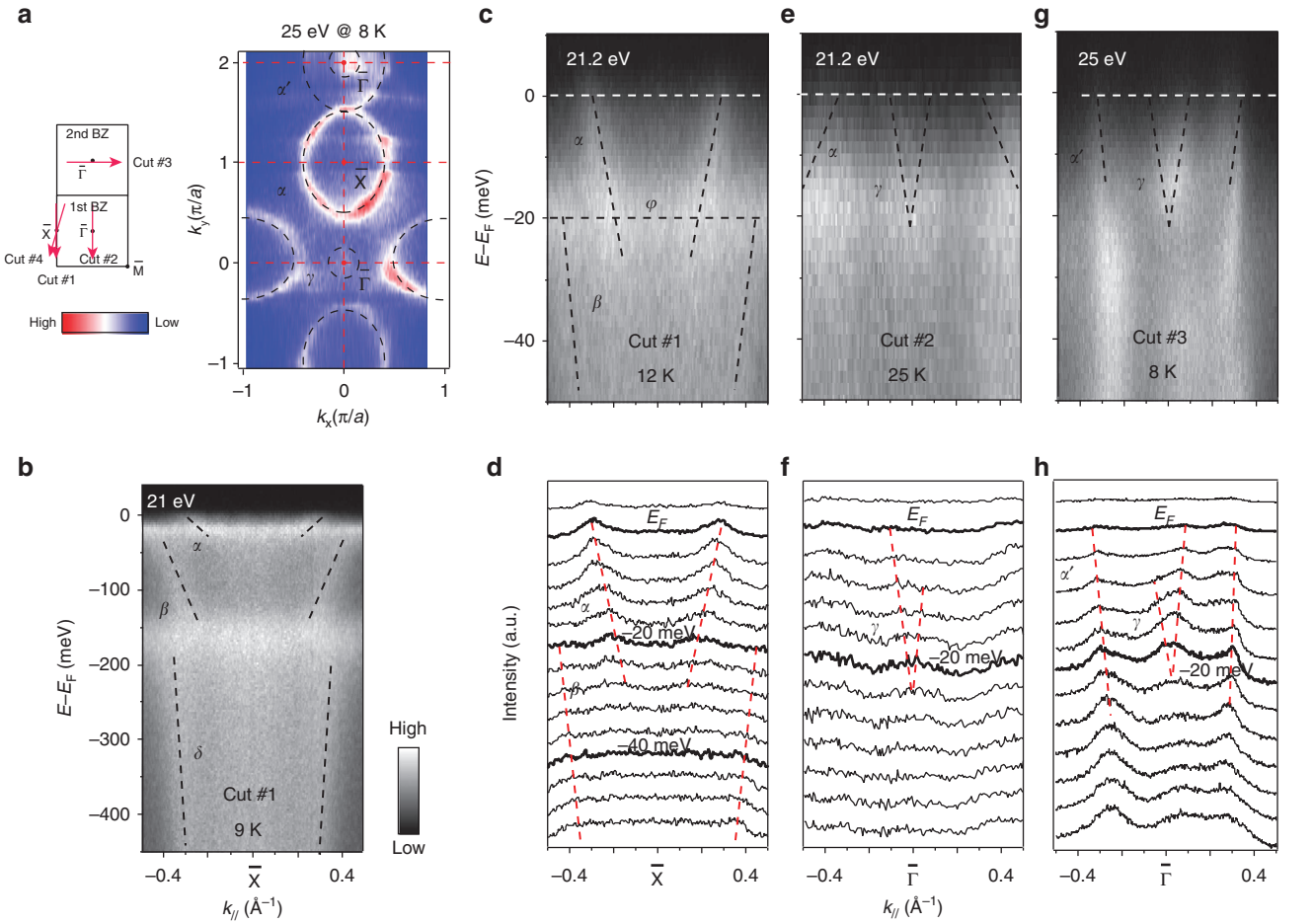

Figure 3 | Dispersive in-gap states around $\bar{\Gamma}$ and $\bar{X}$. (**a**) Photoemission intensity map at the Fermi energy for SmB_6 taken with 25 eV photons at Hiroshima Synchrotron Radiation Center. The intensity was integrated over a window of ($E_F - 5$ meV, $E_F + 5$ meV). The left panel is a sketch of the projected two-dimensional Brillouin zone. (**b**) Photoemission intensity plot over a large energy scale along cut #1 taken with 21 eV photons at Stanford synchrotron Radiation Lightsource. (**c**,**d**) The photoemission intensity plot and momentum distribution curves (MDCs) along cut #1 in the projected two-dimensional Brillouin zone as indicated in panel **a**, respectively. (**e**,**f**) The photoemission intensity plot and MDCs along cut #2, respectively. (**g**,**h**) The photoemission intensity plot and MDCs along cut #3, respectively. The dashed lines in panels **b**–**h** indicate the dispersions of various bands, ignoring band warping at crossings due to hybridization. The photon energies and temperatures for measurements are labelled in individual panels. The α and γ Fermi surfaces cover about 32.7 and 1.1% of projected two-dimensional Brillouin zone, respectively. The Fermi velocities of α and γ are $\sim$0.24 and $\sim$0.22 eV Å, respectively; the linear extrapolations of the α and γ band dispersions cross at 65 ± 4 and 23 ± 3 meV below E_F, respectively.

number. Spin-resolved ARPES requires long acquisition time because of its low count rate and, at this stage, it is not feasible for the weak surface state signal discussed above. Alternatively, instead of examining the chirality of the spin, one could examine the chirality of the OAM with the so-called CD of ARPES, namely, the difference of photoemission intensities taken with right circularly polarized (RCP) light and left circularly polarized (LCP) light. For Bi_2Se_3, it has been shown that photoemission CD signal is proportional to the inner product between OAM and light propagation vector[25]. This technique has been demonstrated to be a powerful tool to investigate the OAM texture of the surface states in TIs[25,26].

Figures 5a and b show two Fermi surface maps taken with 25 eV RCP light and LCP light, respectively. Comparing the two data sets, we can clearly see the difference between the two intensity maps taken with different circular polarizations. The intensity of the upper electron pocket on the positive k_y side is higher than that in the lower electron pocket on the negative k_y side for the RCP data, while the LCP data exhibit an opposite behaviour. The electron pocket at the right side also shows the switching of high intensity regions between the positive k_y side and negative k_y side with different circularly polarized light. However, the electron pocket at the left side does not show strong CD, which is probably because of the asymmetric matrix element effects. Since the incident light is at 50° angle from k_z in the k_x–k_z plane, the emission of the photoelectrons on the left and right Fermi surface sheets are asymmetric with respect to the light propagation direction. The CD can be more clearly represented by the normalized difference (RCP − LCP)/(RCP + LCP) in Fig. 5c. Figure 5d–f shows the similar results for another SmB_{6-x} sample measured with 35 eV photons. More specifically, Fig. 5g plots the CD values in Fig. 5c,f along the right α-Fermi pocket, which could be fitted by individual sinusoidal functions. The amplitude of CD is thus found to be photon energy dependent.

As for the γ band at $\bar{\Gamma}$, its weak intensity makes the CD effects not so obvious. However, for the data taken at 25 eV, Fig. 5h shows that there apparently exists certain intensity inversion between the RCP and LCP data in the MDCs across $\bar{\Gamma}$ along the k_y axis. We can see that higher intensities appear on the negative k_y side for the RCP data but on the positive k_y side for the LCP data. Therefore, both α and γ bands show similar CD that is antisymmetric with respect to the $k_y = 0$ axis.

© 2013 Macmillan Publishers Limited. All rights reserved.

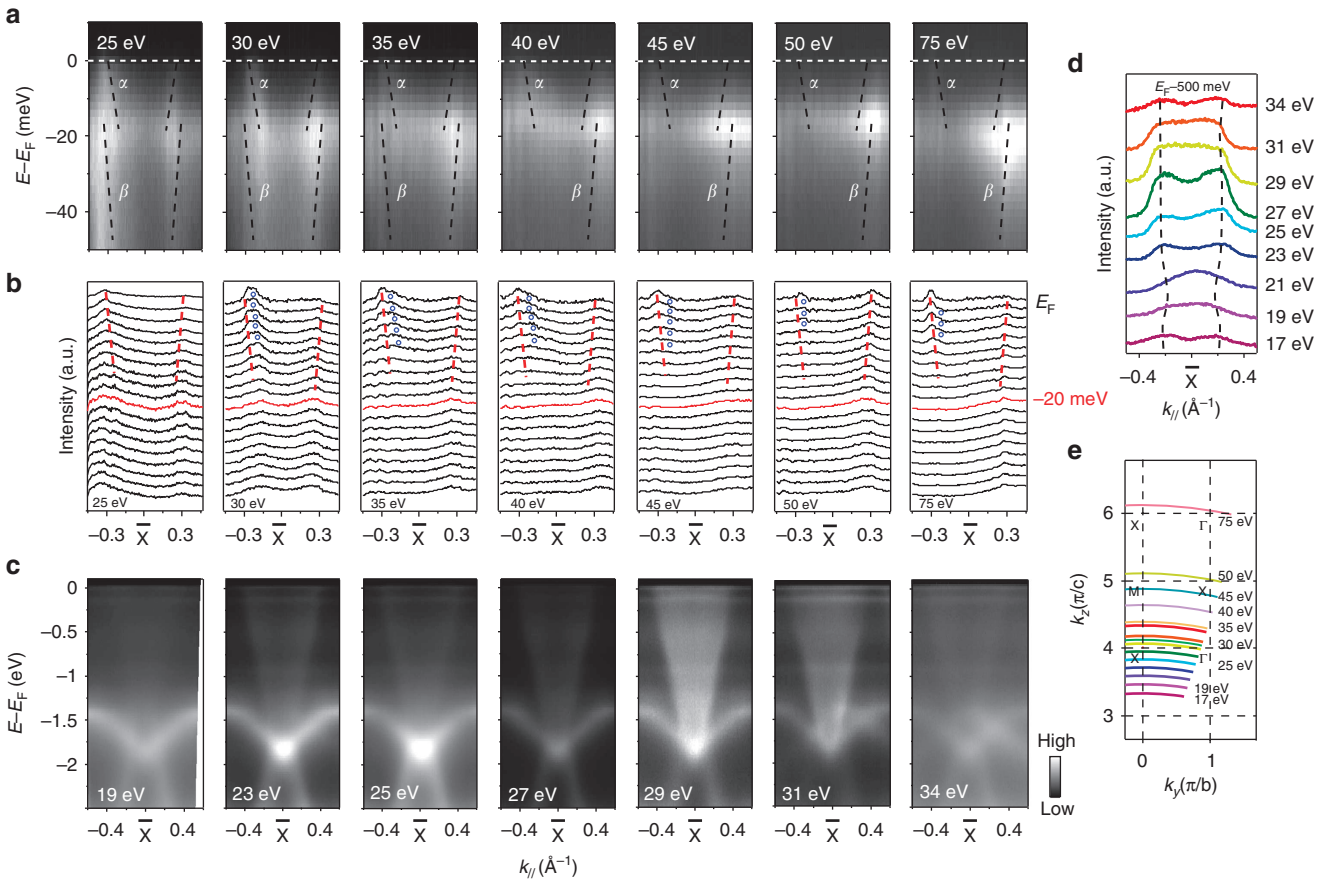

Figure 4 | Photon energy dependence of the in-gap state around $\overline{X}$. (**a**) Photon energy dependence of the photoemission intensity measured along cut #4 shown in Fig. 2a. The α and β band dispersions are indicated by the dashed lines. The bright regions correspond to the location where the 4*f* and 5*d* bands hybridize, which are particularly strong at some photon energies due to matrix element effects. Data were taken at 1 K at BESSY II. (**b**) The corresponding MDC plots of panel **a**. The red dashed lines are dispersions tracked from the MDC peak in the 25-eV data, and they are overlaid on data taken at other photon energies, indicating the lack of photon energy dependence. The blue circles refer to the shoulders in the MDCs that might be contributed by the bulk band. (**c**) The photoemission intensity measured along cut #1 in Fig. 2a for various photon energies. Data were taken at 7 K at Stanford Synchrotron Radiation Lightsource. (**d**) MDCs at -500 meV for data in panel **c**. (**e**) The sampled momentum cuts for various photon energies calculated with the inner potential 14 eV following ref. 10, indicating that the photon range that we used cover an extended Brillouin zone in k_z.

Many CD behaviours observed here resemble those of the non-trivial surface state found in Bi_2Se_3 before[25,26], which indicates that both α and γ bands are likely to be topologically non-trivial. However, we notice that the CD behaviour of the α band is much more complicated than that of Bi_2Se_3. For example, the CD for the left α pocket is much weaker than the others, and the upper and lower α pockets exhibit different CD behaviours from that of the right α pocket. Particularly, the CD for both upper and lower α pockets does not change sign across the Brillouin zone boundary in Fig. 5c,f. In addition to certain final-state effect[27], the complicated CD might in part be due to the coexistence of bulk and surface components in the α pocket. For example, if the bulk *5d* state and the surface state on the α pocket have different CD and their photoemission intensities vary differently with the emission angle and photon energy, one may expect asymmetric CD on left and right α pockets, and the photon energy-dependent CD amplitude shown in Fig. 5g. To fully understand these CD-ARPES data, such as the different functional forms of CD in the upper and right pockets, detailed density functional theory calculations of the OAM texture are required for future further studies, especially when there might be out-of-plane OAM component. Nevertheless, the pattern in our CD-ARPES data does suggest a non-trivial OAM texture (thus, also spin texture through spin-orbit coupling) for the α and γ bands, which is a necessary manifestation in photoemission if they are topologically non-trivial.

Temperature dependence of the electronic structure. If α and γ are topological surface states of a topological KI, they should vanish when the hybridization gap closes at high temperatures. Figure 6a presents temperature-dependent ARPES intensity measured across $\overline{X}$. α stays almost unchanged at $T < 80$ K, but its band velocity starts to increase above 80 K. Eventually, it appears that α and β merge into one highly dispersive band at 150 K, which fits the large-scale band dispersion shown in Fig. 2b. Therefore, α, β and δ could be the broken sections of the *5d* band induced by the *4f*–*5d* hybridization. However, one also sees that α goes straight through ϕ (Fig. 3c,d), which suggests that the α-Fermi surface probably contains contributions both from the not-fully gapped bulk *5d* band and from the topological surface state, although the latter disappears before ending at a Dirac point. This is also consistent with the conclusion that we draw from the photon energy dependence data.

The temperature evolution of the hybridization can be further demonstrated by the integrated EDCs of the images in Fig. 6a. After some processing described in the caption of Fig. 6, the resulting EDCs are presented in Fig. 6b. As temperature increases,

© 2013 Macmillan Publishers Limited. All rights reserved.

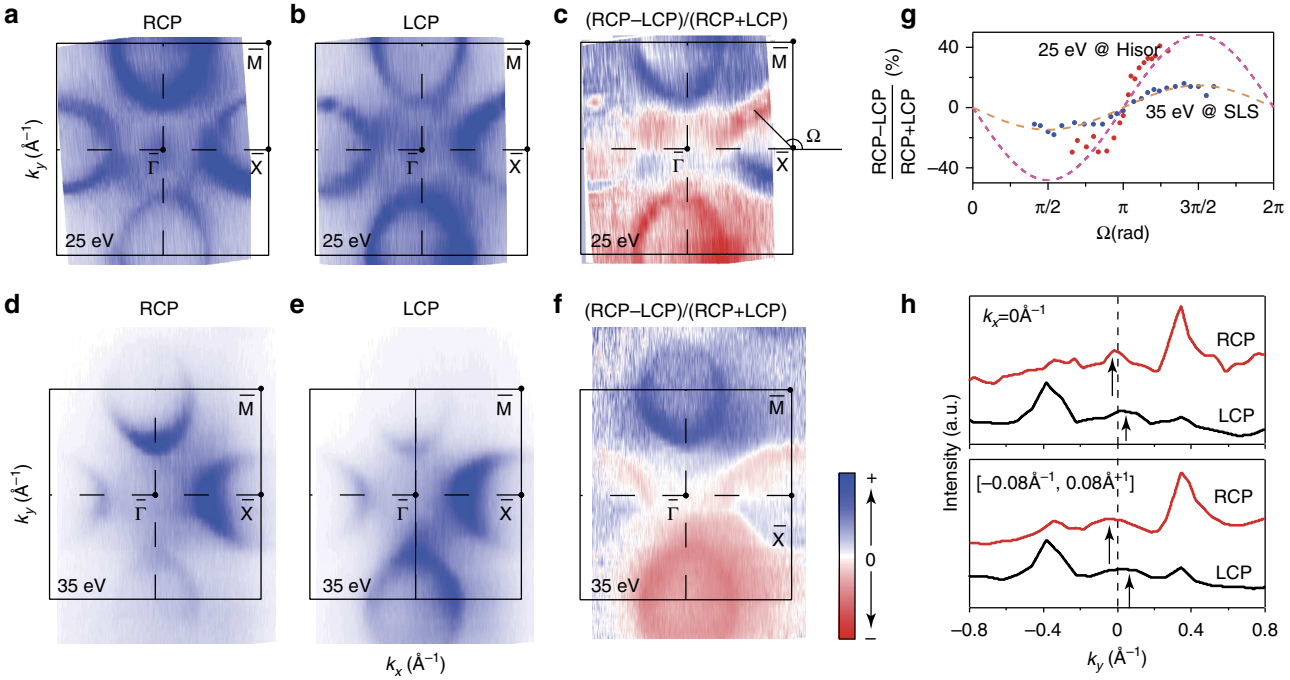

Figure 5 | CD of the surface states at $\overline{X}$ and $\overline{\Gamma}$. (**a**,**b**) Fermi surface maps of SmB_6 taken with right circularly polarized (RCP) and left circularly polarized (LCP) light, respectively. The intensity was integrated over a window of (-5 meV, $+5$ meV). The data were taken at 8 K with 25 eV photons at Hiroshima Synchrotron Radiation Center (HiSOR). (**c**) The differential map of the RCP and LCP photoemission intensities in panels **a** and **b** that are normalized to their sum intensity. (**d**–**f**) The same as in panels **a**–**c**, but for another SmB_{6-x} sample with a slight boron deficiency. The intensity was integrated over a window of (-10 meV, $+10$ meV) and the data were taken at 27 K with 35 eV photons at Swiss Light Source. Note the γ band is not so visible here, probably because of its negligible matrix element at this photon energy. (**g**) The CD values taken along the right pocket in panel **c** (red dots) and in panel **f** (blue dots), where the polar angle Ω is defined within panel **c** with respect to $\overline{X}$. The dashed curves are sine function fits of the experimental data. (**h**) Top: the two MDCs along k_y taken at E_F and $k_x = 0$ with RCP and LCP light, respectively, where the CD of the γ band are indicated by the arrows. Bottom: analogous to the top except that the data are integrated over a k_x window of (-0.08 Å^{-1}, 0.08 Å^{-1}) to cover the γ pocket. The data were taken at 8 K with 25 eV photons at HiSOR.

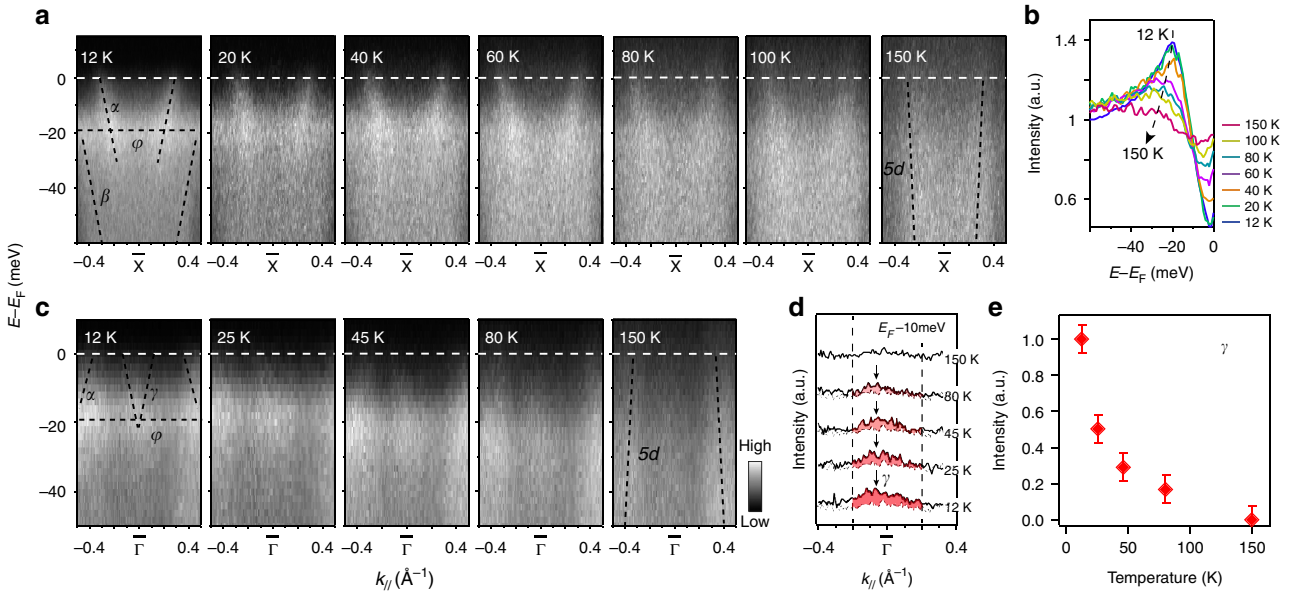

Figure 6 | Temperature dependence of the photoemission data of the surface state around $\overline{X}$. (**a**) Photoemission intensity of SmB_6 along cut #1 in Fig. 2a at 12, 20, 40, 60, 80, 100 and 150 K. (**b**) Temperature dependence of the angle-integrated spectra of panel **a**, the Fermi cutoff effects were removed by dividing the angle-integrated spectra by the energy-resolution convoluted Fermi–Dirac distribution functions at individual temperatures. (**c**) Photoemission intensity of SmB_6 along cut #2 in Fig. 2a at 12, 25, 45, 80 and 150 K. (**d**) Temperature dependence of the MDCs at 10 meV below E_F for data in panel **c**, and the shaded regions represent the difference from the 150-K data. (**e**) Area of the shaded region normalized by the 12-K area. The error bar is the relative uncertainty of the integrated photoelectron count. All data were taken with 21.2 eV photons.

© 2013 Macmillan Publishers Limited. All rights reserved.

the peak near -20 meV (derived from ϕ) is gradually suppressed, and the dip near E_F (a measure of the hybridization strength) is gradually filled. This indicates that the *4f* states become localized and completely lose coherence at $T \approx 150$ K. Consequently, they are decoupled with the *5d* bands and the hybridization disappears[28,29]. Similarly, in the photoemission intensity near $\overline{\Gamma}$ plotted in Fig. 6c, the γ band also vanishes with the hybridization gap at 150 K, which can be further visualized by the MDCs in Fig. 6d, and the integrated intensity in Fig. 6e as well. The thermal broadening effects from 12 to 80 K are not obvious in Fig. 6d; thus, the disappearance of the intensity at 150 K should be intrinsic. Therefore, the temperature dependencies of the surface states are consistent with the behaviours expected for a TKI.

Discussion

Since the (001) surface Brillouin zone contains one $\overline{\Gamma}$ and two $\overline{X}$ points on the zone boundary, we have two α bands enclosing two surface $\overline{X}$ points but only one γ band around $\overline{\Gamma}$. Regardless of whether or not α is a topologically trivial surface state, there will be totally an odd number of branches of surface states, which indicates that the whole system is topologically non-trivial. In fact, the basic electronic structure of these surface states qualitatively agrees with those topological surface states predicted in refs 16,17 remarkably well, although there are some complications in the CD that are still to be understood. In contrast, we note that unlike the case of weakly correlated systems, where theoretical calculations work quantitatively well for describing TIs[14,15], there are some quantitative differences between our data and the calculations of SmB_6. For example, the Fermi crossings of α and γ are different from the calculations, and the observed α Fermi surface has five to six times area of the calculated ones. The discrepancies might be partially because the chemical potentials used in theories are different from that in the real surface, and/or the actual cleaved surface is different from the ideal surface used in the calculations. Furthermore, these discrepancies also demonstrate that correlation might affect the topological surface states, since different calculations could vary somewhat depending on how the correlations were treated[16,17]. Finally, it is also intriguing to note that the Fermi momenta of the two surface states on the (101) surface are 0.0383 and 0.0955 $Å^{-1}$, respectively as found in a recent quantum oscillation measurements of SmB_6 (ref. 30), which are rather different from our measurements of the (001) surface (0.09 $Å^{-1}$ for the small pocket near $\overline{\Gamma}$ and 0.29 $Å^{-1}$ along the short axis of the large oval Fermi surface).

In summary, we present a direct observation of the in-gap surface states in SmB_6. The CD, and photon energy and temperature dependences of these in-gap states were systematically studied, which exhibit characteristic behaviours of a topological surface state for a KI, and thus support that SmB_6 is a possible TKI. Our findings lay the foundation for understanding the anomalous transport properties of SmB_6 and further exploration of the interplay between strong correlations and topological effects in TKI's in general.

Note added. After finishing this manuscript, we note that there are other three pieces of independent ARPES work on SmB_6 (refs 31–33). Two of them report similar results[31,32], except that our temperature dependence data agree with those reported in ref. 31, while ref. 32 suggests the surface states vanish at a much lower temperature of 30 K. The size of the α pocket measured here is similar to that reported in ref. 31 but much smaller than that reported in ref. 32. These discrepancies may be caused by different samples and requires further investigation. On the basis of data taken at 38 K, ref. 33 claims that the in-gap states around X must be bulk states. This partially agrees with our findings. However, the detailed data here taken at lower temperatures do indicate that the α band contains both surface and bulk components.

Methods

Sample synthesis. High-quality single crystals of SmB_6 were grown either with the arc-melting technique or the Al-flux method. The arc melting technique was conducted by establishing a temperature gradient in the slow cooling process. First, the metal Sm were cut into small pieces and mixed with the boron powder in the ratio of Sm:B = 1:6. The mixture was pressed into a pellet with the diameter of 1 cm and thickness of about 0.5 cm. Then the pellet was heated up in the water-cooled clean oven for arc melting. Welding was repeated for five times to ensure the sample uniformity. In the Al-flux method, a chunk of Sm (99.9%) together with the powders of Boron (99.99%) and Al (99.99%) were mixed with a ratio of 1:6:400. Then the mixture was loaded into an alumina crucible. The entire mixture was heated to 1,773 K and then maintained at 1,773 K for about 2 days before slowly cooling it down to 873 K at 5 K h^{-1}. During all the heating progress, the mixture was kept in the circumstance with flowing Argon gas. The samples with Al flux were soaked in dense NaOH solution, and then washed with dilute HNO_3 solution. Shiny crystals in the sizes of millimetre or sub-millimetre were obtained.

ARPES measurement. The samples were cleaved along the (001) plane and measured under ultra-high vacuum of 3×10^{-11} torr. The in-house ARPES measurements were performed with SPECS UVLS discharge lamp (21.2 eV He-Iα light). The synchrotron ARPES experiments were performed at the Beamline 5-4 of Stanford Synchrotron Radiation Lightsource and the one-cubed ARPES station of BESSY II. The CD experiments were performed at Beamline 9 A of Hiroshima Synchrotron Radiation Center and the Surface and Interface Spectroscopy (SIS) beamline of Swiss Light Source. All data were taken with Scienta electron analysers, the overall energy resolution was better than 7 meV and the angular resolution was 0.3°.

References

1. Aeppli, G. & Fisk, Z. Kondo insulators. *Comm. Condens. Matter Phys.* **16,** 155 (1992).
2. Riseborough, P. Heavy fermion semiconductors. *Adv. Phys.* **49,** 257–320 (2000).
3. Coleman, P. *Heavy Fermions: Electrons at the Edge of Magnetism, Handbook of Magnetism and Advanced Magnetic Materials,* Vol 1, 95–148 (Wiley, 2007).
4. Menth, A., Buehler, E. & Geballe, T. H. Magnetic and semiconducting properties of SmB_6. *Phys. Rev. Lett.* **22,** 295 (1969).
5. Allen, J. W., Batlogg, B. & Wachter, P. Large low-temperature Hall effect and resistivity in mixed-valent SmB_6. *Phys. Rev. B* **20,** 4807–4813 (1979).
6. Cooley, J. C., Aronson, M. C., Fisk, Z. & Canfield, P. C. SmB_6: Kondo insulator or exotic metal? *Phys. Rev. Lett.* **74,** 1629 (1995).
7. Nanba, T. *et al.* Gap state of SmB_6. *Physica B* **186–188,** 440–443 (1993).
8. Nyhus, P., Cooper, S. L., Fisk, Z. & Sarrao, J. Low-energy excitations of the correlation-gap insulator SmB_6: a light-scattering study. *Phys. Rev. B* **55,** 12488 (1997).
9. Alekseev, P. A. *et al.* Magnetic excitations in SmB_6 single crystals. *Physica B* **186–188,** 384–386 (1993).
10. Miyazaki, H. *et al.* Momentum-dependent hybridization gap and dispersive in-gap state of the Kondo semiconductor SmB_6. *Phys. Rev. B* **86,** 075105 (2012).
11. Curnoe, S. & Kikoin, K. A. Electron self-trapping in intermediate-valent SmB_6. *Phys. Rev. B* **61,** 15714 (2000).
12. Dzero, M. *et al.* Topological Kondo insulators. *Phys. Rev. Lett.* **104,** 106408 (2010).
13. Dzero, M. *et al.* Theory of topological Kondo insulators. *Phys. Rev. B* **85,** 045130 (2012).
14. Hasan, M. Z. & Kane, C. L. Colloquium: topological insulators. *Rev. Mod. Phys.* **82,** 3045 (2010).
15. Qi, X. L. & Zhang, S. C. Topological insulators and superconductors. *Rev. Mod. Phys.* **83,** 1057 (2011).
16. Takimoto, T. SmB_6: a promising candidate for a topological insulator. *J. Phys. Soc. Jpn* **80,** 123710 (2011).
17. Lu, F. *et al.* Correlated topological insulators with mixed valence. *Phys. Rev. Lett.* **110,** 096401 (2013).
18. Kim, D. J., Grant, T. & Fisk, Z. Limit cycle and anomalous capacitance in the Kondo insulator SmB_6. *Phys. Rev. Lett.* **109,** 096601 (2012).
19. Wolgast, S. *et al.* Low temperature surface conduction in the Kondo insulator SmB_6. Preprint at http://arxiv.org/abs/1211.5104 (2012).
20. Zhang, X. *et al.* Hybridization, inter-ion correlation, and surface states in the Kondo insulator SmB_6. *Phys. Rev. X* **3,** 011011 (2013).
21. Botimer, J. *et al.* Robust surface Hall effect and nonlocal transport in SmB_6: indication for an ideal topological insulator. Preprint at http://arxiv.org/abs/1211.6769 (2012).

© 2013 Macmillan Publishers Limited. All rights reserved.

22. Denlinger, J. D. *et al.* Advances in photoemission spectroscopy of f-electron materials. *Physica B* **281&282,** 716–722 (2000).
23. Massidda, S. *et al.* Electronic structure of divalent hexaborides. *Z. Phys. B* **102,** 83–89 (1997).
24. Ye, Z. R. *et al.* Orbital selective correlations between nesting/scattering/Lifshitz transition and the superconductivity in $AFe_{1-x}Co_xAs$ (A = Li, Na). Preprint at http://arxiv.org/abs/1303.0682 (2013).
25. Park, S. R. *et al.* Chiral orbital-angular momentum in the surface state of Bi_2Se_3. *Phys. Rev. Lett.* **108,** 046805 (2012).
26. Wang, Y. H. *et al.* Observation of a warped helical spin texture in Bi_2Se_3 from circular dichroism angle-resolved photoemission spectroscopy. *Phys. Rev. Lett.* **107,** 207602 (2011).
27. Scholz, M. R. *et al.* Reversal of the circular dichroism in angle-resolved photoemission from Bi_2Te_3. *Phys. Rev. Lett.* **110,** 216801 (2013).
28. Nozawa, S. *et al.* Ultrahigh-resolution and angle-resolved photoemission study of SmB_6. *J. Phys. Chem. Solid* **63,** 1223–1226 (2002).
29. Souma, S. *et al.* Direct observation of pseudogap of SmB_6 using ultrahigh—resolution photoemission spectroscopy. *Physica B* **312-313,** 329–330 (2002).
30. Li, G. *et al.* Quantum oscillations in Kondo Insulator SmB_6. Preprint at http://arxiv.org/abs/1306.5221 (2013).
31. Xu, N. *et al.* Surface and bulk electronic structure of the strongly correlated system SmB_6 and implications for a topological Kondo insulator. *Phys. Rev. B* **88,** 121102(R) (2013).
32. Neupane, M. *et al.* Surface electronic structure of the topological Kondo Insulator candidate correlated electron system SmB_6. *Nat. Commun* **4,** 2991 (2013).
33. Frantzeskakis, E. *et al.* Kondo hybridization and the origin of metallic states at the (001) surface of SmB_6. Preprint at http://arxiv.org/abs/1308.0151 (2013).

Acknowledgements

We are grateful for the discussions with Professor R.B. Tao and Professor G.M. Zhang, and the experimental support by Dr D.H. Lu, Dr Y. Zhang and Dr M. Hashimoto at Stanford Synchrotron Radiation Lightsource (SSRL), Dr E. Rienks at BESSY II, Dr M. Arita and Professor Shimada at Hiroshima Synchrotron Radiation Center, and Dr N. Plumb and Professor M. Shi at Swiss Light Source. This work is supported in part by the National Science Foundation of China and National Basic Research Program of China (973 Program) under the Grant numbers 2012CB921400, 2011CB921802, 2011CBA00100, 2012CB821403 and 2012CB21400. SSRL is operated by the US DOE, Office of Basic Energy Science, Divisions of Chemical Sciences and Material Sciences. This work is conducted within the collaborative network of National Center of Microstructures and Quantum Manipulation.

Author contributions

J.J., Z.R.Y., Z.S., S.Y.T., M.Xu, Q.Q.G., X.H.N., M.Xia and B.P.X. performed ARPES measurements. S.L. and Y.F.L. grew most of the samples and conducted sample characterization measurements, F. C. and X. H. C. grew the samples for the CD-ARPES measurement, J.J., T.Z. and D.L.F. analysed the ARPES data, T.Z., D.L.F., J.J., Z. S. and H.H.W wrote the paper. D.L.F. and H.H.W. are responsible for the infrastructure, project direction and planning.

Additional information

Competing financial interests: The authors declare no competing financial interests.

Reprints and permission information is available online at http://npg.nature.com/reprintsandpermissions/

How to cite this article: Jiang, J. *et al.* Observation of possible topological in-gap surface states in the Kondo insulator SmB_6 by photoemission. *Nat. Commun.* 4:3010 doi: 10.1038/ncomms4010 (2013).

This article is licensed under a Creative Commons Attribution 3.0 Unported Licence. To view a copy of this licence visit http://creativecommons.org/licenses/by/3.0/.

© 2013 Macmillan Publishers Limited. All rights reserved.

nature COMMUNICATIONS

ARTICLE

Received 10 Oct 2015 | Accepted 26 Jan 2016 | Published 8 Mar 2016

DOI: 10.1038/ncomms10840 OPEN

Anomalous correlation effects and unique phase diagram of electron-doped FeSe revealed by photoemission spectroscopy

C.H.P. Wen[1], H.C. Xu[1], C. Chen[1], Z.C. Huang[1], X. Lou[1], Y.J. Pu[1], Q. Song[1], B.P. Xie[1], Mahmoud Abdel-Hafiez[2,3], D.A. Chareev[4], A.N. Vasiliev[5], R. Peng[1] & D.L. Feng[1]

FeSe layer-based superconductors exhibit exotic and distinctive properties. The undoped FeSe shows nematicity and superconductivity, while the heavily electron-doped $K_xFe_{2-y}Se_2$ and single-layer FeSe/$SrTiO_3$ possess high superconducting transition temperatures that pose theoretical challenges. However, a comprehensive study on the doping dependence of an FeSe layer-based superconductor is still lacking due to the lack of a clean means of doping control. Through angle-resolved photoemission spectroscopy studies on K-dosed thick FeSe films and $FeSe_{0.93}S_{0.07}$ bulk crystals, here we reveal the internal connections between these two types of FeSe-based superconductors, and obtain superconductivity below $\sim$46 K in an FeSe layer under electron doping without interfacial effects. Moreover, we discover an exotic phase diagram of FeSe with electron doping, including a nematic phase, a superconducting dome, a correlation-driven insulating phase and a metallic phase. Such an anomalous phase diagram unveils the remarkable complexity, and highlights the importance of correlations in FeSe layer-based superconductors.

[1] State Key Laboratory of Surface Physics, Department of Physics and Advanced Materials Laboratory, Fudan University, Shanghai 200433, China. [2] Institute of Physics, Goethe University Frankfurt, 60438 Frankfurt, Germany. [3] Center for High Pressure Science and Technology Advanced Research, 1690 Cailun Road, Shanghai 201203, China. [4] Institute of Experimental Mineralogy, Russian Academy of Sciences, Chernogolovka, 119991 Moscow , Russia. [5] Low Temperature Physics and Superconductivity Department, M.V. Lomonosov Moscow State University, 119991 Moscow, Russia. Correspondence and requests for materials should be addressed to R.P. (email: pengrui@fudan.edu.cn) or to D.L.F. (email: dlfeng@fudan.edu.cn).

Carrier doping is a critical parameter that governs the electronic correlations and ground states in high-temperature superconductors. Extending a superconducting system to an unexplored doping regime often deepens our understanding of its mechanism. One example is the insights brought by the discovery of heavily electron-doped FeSe layer-based superconductors[1–9]. Compared with undoped FeSe, the enhanced superconductivity in heavily electron-doped FeSe superconductors without any hole Fermi surface[5–11] challenges the prevailing pairing picture based on the nesting between electron and hole Fermi surfaces. Moreover, unlike the moderate correlation strength in most iron pnictides, it is reported that the heavily electron-doped FeSe is strongly correlated and near a Mott insulating phase[12,13], suggesting that the underlying physics may be unified with the cuprate superconductors. To bridge the knowledge gap between these systems, it is crucial to figure out how the superconductivity and correlation behaviour evolve with doping by constructing an FeSe layer-based system with clean and systematic doping control.

Systematic control of the electron doping in a pure iron selenide superconductor is still lacking. Although heavy electron doping has been achieved in intercalated FeSe crystals such as $A_xFe_{2-y}Se_2$ (A = K, Rb, Cs and Tl/K)[1,2] and $(Li_{0.8}Fe_{0.2})$OHFeSe (ref. 3), the doping levels are discrete and fixed. Moreover, microscopic phase separation in $A_xFe_{2-y}Se_2$ (refs 12,14–20) complicates studies of the intrinsic superconductivity. In $(Li_{0.8}Fe_{0.2})$OHFeSe, the polar surface prevents the observation of intrinsic bulk electronic structure in surface sensitive angle-resolved photoemission spectroscopy (ARPES) measurements[11]. In single-layer FeSe films on $SrTiO_3$ or $BaTiO_3$, heavy electron doping is induced by charge transfer from the oxygen-deficient substrate[6], which is difficult to control reliably. It has been reported that post annealing in vacuum can vary the doping in single-layer FeSe films on $SrTiO_3$ substrates[7,21]; however, this approach could also vary the stoichiometry and morphology of the FeSe films[7,21,22], and also fails to induce superconductivity in the second FeSe layer[22]. Moreover, interfacial effects have been suggested to be crucial for the enhanced superconductivity[9,23], which further complicates the issue. Recently, by controlling the doping via K dosing, a superconducting dome has been observed in FeSe films of 3-uc (unit cell) thickness[24]. However, no superconductivity was found in 20-uc FeSe films down to 13 K at any doping[24], so the enhanced superconductivity in 3-uc FeSe/$SrTiO_3$ was attributed to certain interfacial effect[24].

Here we report systematic ARPES studies on the electron-doping-induced effects in both thick FeSe films up to 50 uc and $FeSe_{0.93}S_{0.07}$ bulk crystals via K dosing. With increased doping, the nematic order is suppressed, while the superconductivity is enhanced from a low superconducting transition temperature (T_c) FeSe system with both electron and hole Fermi surfaces to a high T_c (up to 46 K) heavily electron-doped FeSe system with electron Fermi surfaces only. Remarkably, the correlation strength of the system is enhanced with increased doping, opposite to what usually happens in iron pnictides, such as $NaFe_{1-x}Co_xAs$ and $LiFe_{1-x}Co_xAs$ (ref. 25). Consequently, there is a superconductor-to-insulator transition driven by the correlations. Finally, a metallic phase appears in the far overdoped regime. Our results provide the most comprehensive phase diagram of FeSe with electron doping in a clean system, demonstrating that it is exotic and distinct from those of other Fe-based superconductors. In addition to extending the phase diagram of electron-doped FeSe into two unexplored phases, our findings offer a foundation for the global understanding of the interplay among nematic order, superconductivity and electron correlations in the FeSe layer-based superconductors.

Results

Electron doping and enhanced superconductivity. Figure 1 shows the band structures of a 30-uc thick FeSe film before and after K dosing. Before K dosing, the band structure of the 30-uc FeSe film is consistent with those in previous reports on thick FeSe films[6,26] and bulk FeSe crystals[27–30]. The Fermi surfaces consist of hole pockets at Γ (Fig. 1a), contributed by the two hole-like bands crossing E_F around Γ (Fig. 1b,d). Around M, there is dumbbell-shaped spectral weight (Fig. 1a) contributed by the complex band structure, which is due to the splitting of bands with d_{xz} and d_{yz} orbital characters (Fig. 1c,e)[6,26], a hallmark of the orbital ordering or nematicity. After K dosing, which introduces electrons to FeSe, a circular electron pocket appears around M (Fig. 1f). The photoemission spectra show the superposition of two sets of band structures. One set of bands follow the band structure of undoped FeSe and show weaker spectral weight, as indicated by dashed curves in Fig. 1i,j. Considering the finite detection depth of our ARPES measurement[6], these bands are attributed to the interior FeSe layers that are undoped. The other set of bands with the prominent photoemission spectral weight comes from the topmost layer that is heavily electron doped. Around Γ, the two hole-like bands shift to higher binding energies and become flatter (solid curves in Fig. 1g,i). A simple electron-like band appears around M (solid curves in Fig. 1h,j), indicating that the nematic order is suppressed[6]. Considering that this electronic structure is similar to that in other heavily electron-doped iron chalcogenides, the electronic states near Fermi energy in K-dosed FeSe should as well be contributed by electrons with d_{xz}, d_{yz} and d_{xy} orbitals[31]. There is no band structure corresponding to an intermediate doping level, so we conclude that the electron doping induced by K dosing is confined to the topmost single-unit-cell layer of FeSe. Given the quasi-two-dimentional nature of such a single-unit-cell thick layer of FeSe, its band structure should barely disperse along the k_z direction. Therefore, the Fermi surface volume measured at this photon energy reflects the electron doping in the FeSe layer on the basis of Luttinger volume. The estimated carrier concentration is 0.098 electrons per Fe ($x = 0.098 \pm 0.005$). Intriguingly, the symmetrized energy distribution curves in Fig. 1k exhibit back bending after passing the Fermi momentum (k_F) without crossing the Fermi energy. The sharp coherence peaks and back-bending behaviour are hallmarks of Bogoliubov quasiparticles, which implies superconductivity in the K-dosed FeSe. The superconducting gap size is about 10 meV at 31 K, suggesting that the T_c in this layer is significantly enhanced from the bulk T_c of 8 K (ref. 32). The weak features from the undoped interior layers remain gapless around M (Fig. 1k), indicating that the superconductivity only exists in the doped topmost layer, without extending via proximity effect into the layers beneath. Our results are in contrast to the absence of superconductivity in 35-uc $Fe_{0.92}Co_{0.08}Se$ thick films[9]. Compared with $Fe_{0.92}Co_{0.08}Se$, the noticeably sharper lineshape of the momentum distribution curves (Supplementary Fig. 1) and the enhanced superconductivity in K-dosed FeSe suggest much weaker impurity scattering in FeSe doped by off-FeSe-plane K atoms than the in-FeSe-plane Co ions[25,33]. The lower T_c in Co-doped FeSe suggests the strong pair breaking effect of Co in heavily electron-doped FeSe.

Absence of interfacial effect. Figure 2 compares the superconducting gaps of K-dosed FeSe films with various thicknesses and that of K-dosed $FeSe_{0.93}S_{0.07}$ bulk crystals ($T_c = 9.7$ K without K dosing[34]). At an electron doping level around $x = 0.09$, back-bending dispersions and superconducting gaps are observed for all the K-dosed FeSe films with thicknesses varying from 4 uc to

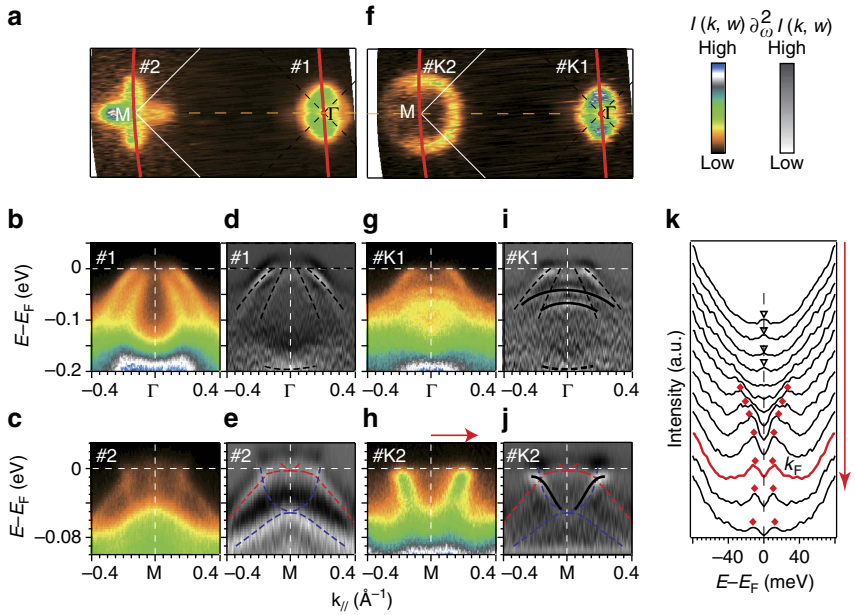

Figure 1 | Electronic structures before and after K dosing for a 30 uc FeSe film on $SrTiO_3$. (**a**) Photoemission intensity map at the Fermi energy (E_F) for a 30 uc FeSe film. The intensity was integrated over an energy window of (E_F-10 meV, E_F+10 meV). The red curves indicate the momentum locations of the cuts #1 and #2. (**b**,**d**) Photoemission intensity along cut #1 in **a** and the corresponding second derivative, respectively. (**c**,**e**) The same as **b**,**d** but along cut #2 in **a**. (**f**) Photoemission intensity map over an energy window of (E_F-10 meV, E_F+10 meV) for the 30 uc FeSe film with electron doping $x=0.098$ after K dosing. The red curves indicate the momentum locations of the cuts #K1 and #K2. (**g**,**i**) Photoemission intensity along cut #K1 in **f** and the corresponding second derivative, respectively. (**h**,**j**) The same as **g**,**i** but along cut #K2 in **f**. (**k**) Symmetrized energy distribution curves along the momenta indicated by the arrows in **h**. The data in **h**,**j** and **k** were taken at 31 K, the others at 70 K.

50 uc (Fig. 2a–e). Moreover, for K-dosed $FeSe_{0.93}S_{0.07}$ bulk crystals with no FeSe/oxide interface, a superconducting gap is also observed at 31 K (Fig. 2f). The gap size Δ is about 10 meV at 31 K for all the films and bulk $FeSe_{0.93}S_{0.07}$ (Fig. 2g). Comparing the temperature dependence of the gap size in the 30-uc and the 10-uc FeSe films as an example, the gaps are both 6 meV in size at 42 K (Fig. 2h), and close around 46 K (Fig. 2i,j). The temperature dependences of the gap sizes are summarized in Fig. 2k, in which all samples can be well fit by the same Bardeen–Cooper–Schrieffer formula with a T_c around 46 K. Therefore, for thick films or bulk material, the enhanced superconductivity here is intrinsic to the electron-doped FeSe, and is not dependent on the thickness or the FeSe/$SrTiO_3$ interface, which is distinct from the previous report on K-dosed FeSe (ref. 24).

Doping dependence. The evolution of the electronic structure with electron doping is further studied through ARPES on FeSe with systematically controlled K dosing. Figure 3a shows the spectra around Γ as a function of doping. For all the spectra at all doping levels, dispersions from the undoped interior FeSe layers are always visible, and do not depend on the doping at the surface. As the electron doping level x of the surface FeSe layer is increased from 0.033 to 0.127, the two hole-like bands gradually shift to higher binding energies (Fig. 3a,b). Simultaneously, these two bands become flat for x from 0.054 to 0.127, then become incoherent for $x=0.137$ and 0.158, and finally disappear for $x\sim0.189$ (Fig. 3a), indicating increasing correlation strength with higher electron doping. As shown in Fig. 3b, the two quasiparticle peaks at Γ devolve into incoherent spectral weight (pink shadow in Fig. 3b) when $x=0.137$ and 0.158, and totally disappear once x reaches 0.189. On further doping to $x\sim0.228$, there is an electron-like band around the zone center (Fig. 3a), with well-defined quasiparticle peaks and no gap at 31 K (Fig. 3b, Supplementary Fig. 2). The electron-like band gradually sinks to higher binding energies as x increases from 0.218 to 0.232, and disperses distinctly from the quantum well states of potassium (Fig. 3a, Supplementary Fig. 3). A recent scanning tunnelling spectroscopy study has shown an unoccupied electron band in single-layer FeSe/$SrTiO_3$ (ref. 35). The electron band observed in FeSe with $x\sim0.228$ could have the same origin, which is a partially occupied band of FeSe due to the heavy electron doping. These results suggest a metallic phase in the overdoped regime. The well-defined quasiparticle dispersion for $x\sim0.228$ suggests that the impurity scattering of K dosing is negligible, and the behaviour of the incoherent and diminishing spectral weight from $x=0.137$ to $x\sim0.189$ is intrinsic.

Around M, two electron-like bands are observed for the K-dosed FeSe with $x=0.033$ (Fig. 3c), which are illustrated by the solid curves in Fig. 3d. Compared with the undoped band structure in Fig. 1e, the upper band shifts downwards and the lower band remains at a fixed binding energy. Since the energy separation between them reflects the strength of the nematic order[26], the decreased energy separation with increasing doping indicates the weakening of nematicity. As the doping further increases, the two electron bands become degenerate at the Fermi energy for $x=0.087$ and remarkably becomes flatter as x increases from 0.087 to 0.158, indicating enhanced correlations for bands around M, consistent with the behaviour of the bands around Γ. Remarkably, for $x\sim0.189$, the bands from the topmost layer becomes incoherent and the corresponding spectral weight is depleted at the Fermi energy. The depletion of spectral weight at the Fermi energy for the K-dosed bands around both Γ and M indicates that FeSe becomes insulating in this regime. On further electron doping to $x\sim0.228$, K-dosed FeSe shows dispersive bands below the Fermi energy. The band around M might be due to some folding and hybridization effects if certain charge or spin order exists in the insulating regime and persists to the metallic

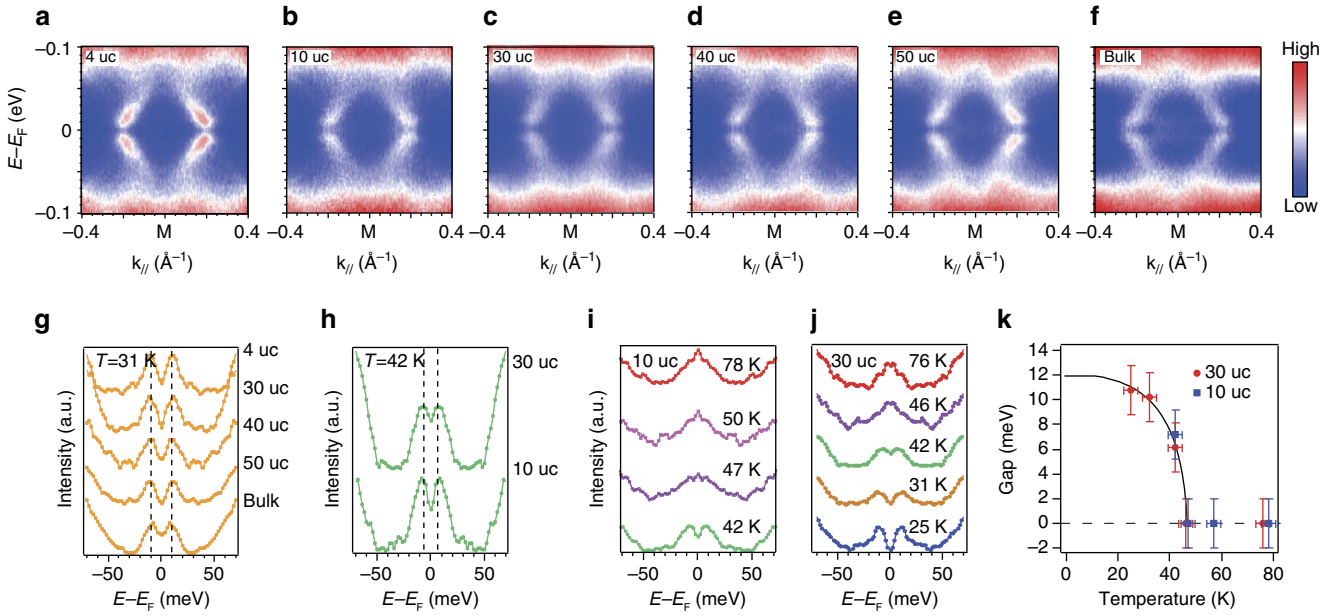

Figure 2 | Superconducting gaps in K-dosed FeSe films with varied thicknesses and that of K-dosed $FeSe_{0.93}S_{0.07}$ bulk crystals. (**a**–**f**) Symmetrized photoemission spectra of K-dosed FeSe films with thickness of 4 uc, 10 uc, 30 uc, 40 uc, 50 uc and K-dosed bulk $FeSe_{0.93}S_{0.07}$, respectively. The data for 10 uc were taken at 42 K, the others at 31 K. (**g**) Symmetrized energy distribution curves (EDCs) at the Fermi momenta for the FeSe films with different thicknesses and $FeSe_{0.93}S_{0.07}$ bulk crystal at 31 K after K dosing. (**h**) The symmetrized EDCs at the Fermi momenta for FeSe films with thicknesses of 10 uc and 30 uc at 42 K after K dosing. (**i**,**j**) Temperature dependences of the symmetrized EDCs at k_F for thicknesses of 10 uc and 30 uc, respectively. (**k**) Superconducting gap sizes as a function of temperatures from the data in **i**,**j**. The solid curve is the result of a Bardeen–Cooper–Schrieffer formula fit. The doping levels are 0.094 ± 0.005, 0.097 ± 0.005, 0.098 ± 0.005, 0.087 ± 0.005, 0.105 ± 0.005 and 0.115 ± 0.005 electrons per Fe for **a**–**f** respectively. Temperature error bars are due to measurement uncertainties. The error bars of the superconducting gaps are due to the s.d. of the fitting with a typical superconducting-state spectral function.

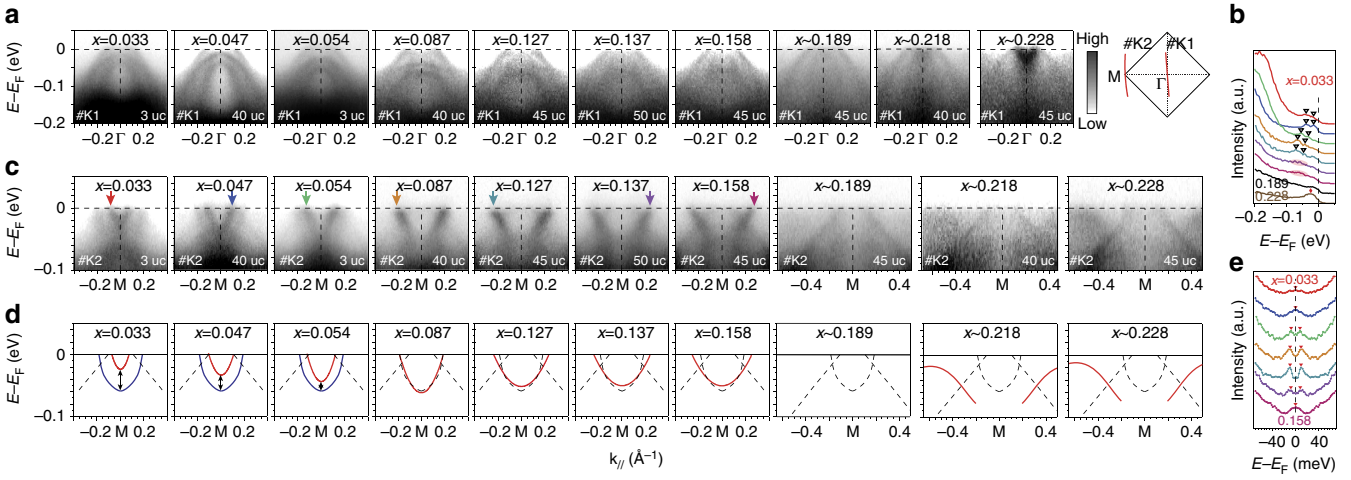

Figure 3 | Evolution of electronic structure and superconducting gap as a function of electron doping induced by K dosing. (**a**) Evolution of photoemission spectra along cut #K1 in the inset as a function of increasing electron doping. The inset shows the Brillouin zone and the red curves indicate the momentum location of the cuts #K1 and #K2. (**b**) Energy distribution curves (EDCs) at Γ with different dopings. Triangles mark the band tops for the two parabolic bands after K dosing. For $x = 0.137$ and $x = 0.158$, only diffuse spectral weight can be observed as indicated by the pink shadow. For $x \sim 0.189$, the spectral weight could not be resolved. At $x \sim 0.228$, there is a well-defined peak near the Fermi energy, which is the band bottom of the electron-like band. (**c**) Doping-dependent evolution of photoemission spectra along cut #K2. (**d**) Doping-dependent evolution of the dispersions around M extracted from **c**. The solid curves indicate the electron-like bands of the doped surface layer, which are determined by parabolic fits to the dispersions in **c**. The dashed curves indicate the dispersions from undoped interior layers. (**e**) Symmetrized EDCs showing the evolution of the superconducting gap as a function of doping. The momenta of spectra are indicated by the arrows in **c** with corresponding colours. The data in this figure were taken at 31 K, except those for $x = 0.033$ and $x = 0.054$, which were taken at 25 K. The doping levels are calculated based on the Luttinger volume, with an uncertainty of ± 0.005 electrons per Fe for $x \leq 0.158$ and ± 0.01 electrons per Fe for $x > 0.158$.

regime, which is a speculation and deserves further investigation. We emphasize that the data shown here were taken on four different samples with thicknesses of 3, 40, 45 and 50 uc (noted in Fig. 3a,c), and they have been reproduced in another six samples. The band dispersions evolve in the same manner, regardless of film thickness.

The symmetrized energy distribution curves in Fig. 3e give the doping dependence of the superconducting gap. The superconducting gap is observed at 25 K for the doping level 0.054, indicating a coexistance regime in which the superconductivity is enhanced while the nematicity is not fully suppressed. On the basis of empirical fitting of the superconducting gap[36], the gap size increases to ~9.7 meV at 31 K for films with $x = 0.087$, and is slightly enhanced to 11.3 meV from $x = 0.087$ to $x = 0.127$, and then decreases to 7.7 meV at $x = 0.137$, indicating an optimal doping around 0.127. The T_c increment for $x \leq 0.12$ in K-dosed FeSe is consistent with that in single-layer FeSe/$SrTiO_3$ (ref. 7). The gap closes for $x = 0.158$, suggesting that T_c falls below 31 K. The sample with x ~0.228 is not superconducting at 31 K (Supplementary Fig. 2).

Correlation effects and phase diagram. Figure 4a summarizes the effective mass of the electron band around M obtained from parabolic fits. The band mass increases monotonically in the doping range $x = 0.087$–0.158 for K-dosed FeSe, while those of $Rb_xFe_{2-y}Se_2$ and $K_xFe_{2-y}Se_2$ at the electron doping level of 0.2 (ref. 37) follow the same trend, suggesting enhanced correlation strength with increasing electron doping.

Figure 4b shows the phase diagram of K-dosed FeSe as a function of doping. Because of experimental constraints, the superconducting gaps of the undoped and underdoped FeSe could not be determined, when the T_c is <25 K. However, it is known that the superconductivity coexists with nematic order in undoped FeSe crystal at low temperatures[27,29,30]. Our results extend the coexistence regime to $x \sim 0.054$, where T_c even reaches >25 K. By summarizing the superconducting gap size at 31 K, and the T_c determined by the gap-closing temperature (Supplementary Fig. 4), we obtain a superconducting dome with enhanced superconductivity near the nematic phase. The maximum T_c is ~46 K, which is significantly enhanced compared with that in undoped FeSe. More intriguingly, an insulating phase eventually emerges, following a continuous increase of the effective mass with doping, suggesting that the insulating phase is driven by strong correlations. Further enhancement of the electron doping tunes the insulating state into a metallic phase with the Fermi crossings only around Γ, which has not previously been explored.

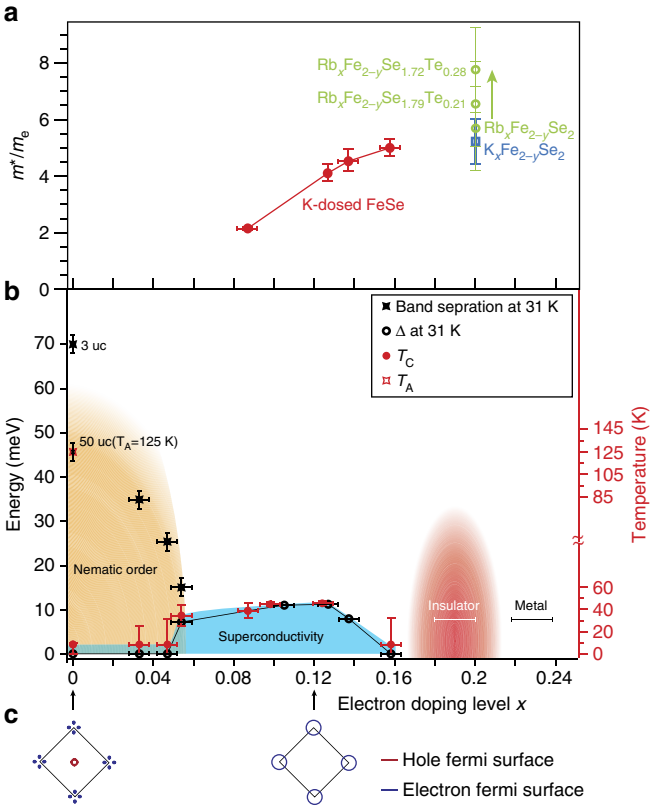

Figure 4 | Phase diagram of FeSe as a function of electron doping. (**a**) Effective mass of the electron band at M as a function of doping; m_e is the mass of free electrons. The data points of K-dosed FeSe were obtained by the parabolic fits, and the error bars of the effective mass are due to the s.d. of the fitting process. The data points of $Rb_xFe_{2-y}Se_2$ and $K_xFe_{2-y}Se_2$ were from ref. 37. (**b**) Phase diagram of electron-doped FeSe, and the summary of the nematic band splitting, superconducting gap size and the T_c as a function of doping. The nematic band splitting was determined by the energy difference between band bottoms at M, while the undoped value is from ref. 6. For dopings without a superconducting gap at 31 K, the values of T_c were set at the T_c of bulk FeSe, 8 K. Otherwise, the values of T_c were determined by the superconducting gap-closing temperature. The gap sizes at 31 K were obtained through empirical fitting of the symmetrized energy distribution curves to a typical superconducting-state spectral function, and their error bars are due to the s.d. of the fitting process. The uncertainty in the electron doping is ±0.005 electrons per Fe for $x \leq 0.158$ and is ±0.01 electrons per Fe at higher dopings. Temperature error bars are due to measurement uncertainties. The energy error bars of the band splitting are due to the finite width of the spectra. Color gradients illustrate the uncertainty in the domain boundaries. (**c**) Different Fermi surface topologies of undoped FeSe and heavily electron-doped FeSe.

Discussion

The phase diagram of the K-dosed FeSe has some of the essential ingredients of the canonical phase diagram of the iron-based superconductors. For example, the superconductivity is enhanced when the nematic order is suppressed, suggesting that the competition between nematicity and superconductivity likely plays an important role on the enhanced superconductivity[38]. The superconductivity is suppressed at higher dopings. Besides these essential ingredients, however, from an electronic structure perspective, the phase diagram is rather exotic and exhibits the following unique features.

First, superconductivity with a maximum T_c of 46 K is achieved in K-dosed FeSe for an optimal doping $x \sim 0.12$. The T_c in K-dosed FeSe is higher than the optimal T_c of 8 K in FeSe bulk crystals at ambient pressure[32], that of 20 K in FeSe nanoparticles[39], and that of 37 K in FeSe bulk crystals under high external pressure[40]. Indeed, it approaches the highest T_c in all heavily electron-doped FeSe-based bulk crystals, which is 48 K in $A_xFe_{2-y}Se_2$ under high pressure[41]. The high T_c in optimally K-dosed FeSe provides insight in understanding the origin of the high T_c in single-layer FeSe/$SrTiO_3$, considering that they are both a single-unit-cell layer of FeSe having an electron doping $x \sim 0.12$ (refs 6,7). On the basis of the pairing temperature measured by ARPES, the electron doping alone in an FeSe layer can enhance the T_c to 46 K, which is lower than the T_c of 65 K in single-layer FeSe/$SrTiO_3$ determined in the same way[6,7]. Moreover, if considering the 109 K T_c found in the recent *in situ* transport measurements on single-layer FeSe/$SrTiO_3$ (ref. 42), the interfacial effects beyond carrier doping could enhance T_c by >60 K.

Second, in the overdoped regime, most cuprates and iron-based superconductors become more Fermi liquid like as the correlation strength decreases[25]. Remarkably, in K-dosed FeSe, the correlation strength is enhanced with increasing electron doping, which is qualitatively different from the behaviour in iron arsenides. Such an enhancement of electron correlation strength with increased doping is quite anomalous, considering that the

correlation strength usually decrease when doped away from $3d^5$ for Fe-based superconductors[43–45]. For example, the bandwidths of $NaFe_{1-x}Co_xAs$ and $LiFe_{1-x}Co_xAs$ increase with electron doping[25]. Besides, iron-based superconductors are generally considered to be moderately correlated materials with a metallic parent phase. However, FeSe layer-based superconductors are evidently in the vicinity of insulating phases. For example, non-stoichiometric FeSe with the chemical formula Fe_4Se_5 and $\sqrt{5}\times\sqrt{5}$ Fe vacancy order has been suggested to be a Mott insulator[46], and while (Li,Fe)OHFeSe can be tuned into an insulating phase by enhancing the electron doping through liquid gating[47]. Here we have observed a superconductor-to-insulator transition in heavily electron-doped FeSe by K dosing. More importantly, the evolution to the insulating phase in K-dosed FeSe is characterized by the increasing effective mass and diminishing spectral weight of the coherent bands. Similar behaviour is observed through the metal-to-insulator transition of NiS_xSe_{2-x} (ref. 48), which is considered to be a prototypical bandwidth-controlled Mott transition[49]. In the Brinkman-Rice picture, the quasiparticles become heavier until eventually their effective masses diverge in the insulating phase. Recently, such an enhancement of effective mass accompanied by a transition to an insulating phase has been observed in $Rb_xFe_{2-y}Se_2$ under chemical pressure[37], which has the similar electron doping as the insulating phase in K-dosed FeSe (Fig. 4). Although a larger mass is observed before entering the insulating state for $Rb_xFe_{2-y}Se_2$ than that for K-dosed FeSe, these electron-doped iron chalcogenides with $x\sim$ 0.2 probably share a similar correlation-driven superconductor-to-insulator transition route. We can speculate that there is likely certain magnetic and/or charge order in this insulating phase, which will need further investigation. Before entering the insulating phase, electron correlation is strengthened with higher K dosing, thus the spin susceptibility should be enhanced. Therefore, one possibility is that the spin susceptibility may diverge on approaching the insulating phase from lower dopings, and eventually an antiferromagnetic order may ultimately set in the insulating phase.

Third, an insulator to metal transition occurs on the far overdoped side. In this metallic phase, the Fermi surface consists of only a small electron pocket around Γ, while the bands near M sink below the Fermi energy. This Fermi surface topology is distinct from those of all other heavily electron-doped Fe-based superconductors, which consist of electron pockets near M. Although superconductivity is not observed at 31 K for this metallic phase, it remains to be explored at lower temperatures or at higher dopings.

Finally, this unique phase diagram connects two types of Fe-based superconductors with different Fermi surface topologies and different pairing symmetries. The Fermi surface of undoped FeSe consists of hole pockets at Γ and electron pockets around M (refs 6,27–30), while the superconducting paring symmetry is most likely s± type with sign reversal between the hole and electron pockets (Fig. 4c), as evidenced by previous experiments[50]. On the other hand, the Fermi surface of electron-doped FeSe consists of only electron pockets, and the superconducting pairing symmetry is proposed to be different from the usual s± type[51–58], and has been suggested to be plain s-wave pairing without any sign change for FeSe/$SrTiO_3$ from recent STM studies[59].

To summarize, we have obtained enhanced superconductivity in thick FeSe films and $FeSe_{0.93}S_{0.07}$ bulk crystals by K dosing, indicating that the T_c can reach ~46 K in a single-unit-cell layer FeSe by electron doping without any interfacial effect. K-dosed FeSe serves as a clean FeSe layer-based superconductor with well-controlled electron doping and weak impurity scattering. The different T_c in K-dosed FeSe and Co-doped FeSe suggests strong pair breaking of Co in heavily electron-doped FeSe. More importantly, we discover a systematic evolution of electronic correlations, and establish the extraordinary phase diagram of FeSe upon electron doping. A correlation-driven insulating phase and a metallic phase are uncovered at high doping levels. Our findings offer FeSe films as a prototypical system for understanding the interplay between different phases, such as the evolution between different pairing symmetries, the superconductor-to-insulator transition, and the coexistence of nematic order and superconductivity.

Methods

Growth of FeSe films and single crystals. The thick FeSe films were grown on TiO_2-terminated Nb:$SrTiO_3$ (001) substrates. FeSe films were co-deposited with the Se flux twenty times greater than the Fe flux, while the substrates were kept at 370 °C, and then post annealed at 410 °C in vacuum for 2.5 h and directly transferred into the ARPES chamber. The single crystals of $FeSe_{0.93}S_{0.07}$ ($T_c = 9.7$ K) were grown using the flux method[34,60].

ARPES measurements. ARPES data were taken under ultrahigh vacuum of 1.5×10^{-11} mbar, with a discharge lamp (21.2 eV He-Iα light) and a Scienta R4000 electron analyzer. The energy resolution is 7 meV and the angular resolution is 0.3°. The sample growth/cleaving, K deposition and ARPES measurements were all conducted *in situ*.

K-dosing experiments. Electron doping is induced by depositing K atoms with a commercial SAES alkali dispenser; the sample temperature was kept between 30–50 K when depositing K atoms. This low temperature reduces the mobility of the deposited atoms, and thus the K atoms simply transfer electrons to FeSe without affecting the stoichiometry of the FeSe surface. The doping levels <0.158 were determined by ARPES based on the Luttinger volume of Fermi surfaces. Correlating the estimated electron doping from the Luttinger volume with the K coverage calculated from deposition time and the flux of K measured by quartz crystal microbalance, we obtain a relationship between the two parameters, which we modelled by exponential function. The function was used to estimate the doping levels of K-dosed FeSe with $x>0.158$. The uncertainty in the electron doping for $x\leq0.158$ is ±0.005 electrons per Fe, which is estimated by the combination of the momentum resolution of ARPES measurements and the uncertainty in determining the size of the electron pockets. The uncertainty in the electron doping for $x>0.158$ is estimated as ±0.01 electrons per Fe, from the combination of momentum resolution, the experimental uncertainty in determining the K coverage, and the uncertainty in the extrapolation required. We found doping levels >0.24 hard to achieve by K dosing.

References

1. Guo, J. G. *et al.* Superconductivity in the iron selenide $K_xFe_2Se_2$ ($0\leq x\leq1.0$). *Phys. Rev. B* **82,** 180520(R) (2010).
2. Ying, T. P. *et al.* Observation of superconductivity at 30~46 K in $A_xFe_2Se_2$ (A = Li, Na, Ba, Sr, Ca, Yb, and Eu). *Sci. Rep.* **2,** 426 (2012).
3. Lu, X. F. *et al.* Coexistence of superconductivity and antiferromagnetism in $(Li_{0.8}Fe_{0.2})$OHFeSe. *Nat. Mater.* **14,** 325–329 (2015).
4. Wang, Q. Y. *et al.* Interface-Induced High-Temperature Superconductivity in Single Unit-Cell FeSe Films on $SrTiO_3$. *Chin. Phys. Lett.* **29,** 037402 (2012).
5. Liu, D. F. *et al.* Electronic origin of high-temperature superconductivity in single-layer FeSe superconductor. *Nat. Commun.* **3,** 931 (2012).
6. Tan, S. Y. *et al.* Interface-induced superconductivity and strain-dependent spin density waves in FeSe/$SrTiO_3$ thin films. *Nat. Mater.* **12,** 634–640 (2013).
7. He, S. *et al.* Phase diagram and electronic indication of high-temperature superconductivity at 65 K in single-layer FeSe films. *Nat. Mater.* **12,** 605–610 (2013).
8. Peng, R. *et al.* Measurement of an Enhanced Superconducting Phase and a Pronounced Anisotropy of the Energy Gap of a Strained FeSe Single Layer in FeSe/Nb:$SrTiO_3$/$KTaO_3$ Heterostructures Using Photoemission Spectroscopy. *Phys. Rev. Lett.* **112,** 107001 (2014).
9. Peng, R. *et al.* Tuning the band structure and superconductivity in single-layer FeSe by interface engineering. *Nat. Commun.* **5,** 5044 (2014).
10. Zhang, Y. *et al.* Nodeless superconducting gap in $A_xFe_2Se_2$ (A = K,Cs) revealed by angle-resolved photoemission spectroscopy. *Nat. Mater.* **10,** 273–277 (2011).
11. Niu, X. H. *et al.* Surface electronic structure and isotropic superconducting gap in$(Li_{0.8}Fe_{0.2})$OHFeSe. *Phys. Rev. B* **92,** 060504 (2015).
12. Chen, F. *et al.* Electronic Identification of the Parental Phases and Mesoscopic Phase Separation of $K_xFe_{2-y}Se_2$ Superconductors. *Phys. Rev. X* **1,** 021020 (2011).

13. Yi, M. *et al.* Observation of Temperature-Induced Crossover to an Orbital-Selective Mott Phase in $AxFe_2Se_2$ (A = K, Rb) Superconductors. *Phys. Rev. Lett.* **110,** 067003 (2013).
14. Fang, M. H. *et al.* Fe-based superconductivity with $T_c = 31$ K bordering an antiferromagnetic insulator in (Tl, K) Fe_xSe_2. *Europhys. Lett.* **94,** 27009 (2011).
15. Wang, H. D. *et al.* Superconductivity at 32 K and anisotropy in $Tl_{0.58}Rb_{0.42}Fe_{1.72}Se_2$ crystals. *Europhys. Lett.* **93,** 47004 (2011).
16. Zhao, J. H. *et al.* Neutron-Diffraction Measurements of an Antiferromagnetic Semiconducting Phase in the Vicinity of the High-Temperature Superconducting State of $K_xFe_{2-y}Se_2$. *Phys. Rev. Lett.* **109,** 267003 (2012).
17. Wang, Z. *et al.* Microstructure and ordering of iron vacancies in the superconductor system $K_yFe_xSe_2$ as seen via transmission electron microscopy. *Phys. Rev. B* **83,** 140505 (R) (2011).
18. Berlijn, T. *et al.* Effective doping and suppression of Fermi surface reconstruction via Fe vacancy disorder in $K_xFe_{2-y}Se_2$. *Phys. Rev. Lett.* **109,** 147003 (2012).
19. Wang, C. H. *et al.* Disordered Fe vacancies and superconductivity in potassium-intercalated iron selenide $K_{2-x}Fe_{4+y}Se_5$. *Europhys. Lett.* **111,** 27004 (2015).
20. Ricci, A. *et al.* Direct observation of nanoscale interface phase in the superconducting chalcogenide $K_xFe_{2-y}Se_2$ with intrinsic phase separation. *Phys. Rev. B* **91,** 020503 (2015).
21. He, J. *et al.* Electronic evidence of an insulator-superconductor crossover in single-layer FeSe/$SrTiO_3$ films. *Proc. Natl Acad. Sci. USA* **111,** 18501–18506 (2014).
22. Liu, X. *et al.* Dichotomy of the electronic structure and superconductivity between single-layer and double-layer FeSe/$SrTiO_3$ films. *Nat. Commun.* **5,** 5047 (2014).
23. Lee, J. J. *et al.* Interfacial mode coupling as the origin of the enhancement of T_c in FeSe films on $SrTiO_3$. *Nature* **515,** 245–248 (2014).
24. Miyata, Y. *et al.* High-temperature superconductivity in potassium-coated multilayer FeSe thin films. *Nat. Mater.* **14,** 775–779 (2015).
25. Ye, Z. R. *et al.* Extraordinary doping effects on quasiparticle scattering and bandwidth in iron-based superconductors. *Phys. Rev. X* **4,** 031041 (2014).
26. Zhang, Y. *et al.* Distinctive momentum dependence of the band reconstruction in the nematic state of FeSe thin film. Preprint at http://arxiv.org/abs/1503.01556 (2015).
27. Nakayama, K. *et al.* Reconstruction of band structure induced by electronic nematicity in an FeSe superconductor. *Phys. Rev. Lett.* **113,** 237001 (2014).
28. Maletz, J. *et al.* Unusual band renormalization in the simplest iron-based superconductor $FeSe_{1-x}$. *Phys. Rev. B* **89,** 220506(R) (2014).
29. Watson, M. D. *et al.* Emergence of the nematic electronic state in FeSe. *Phys. Rev. B* **91,** 155106 (2015).
30. Zhang, P. *et al.* Observation of two distinct d_{xz}/d_{yz} band splittings in FeSe. *Phys. Rev. B* **91,** 214503 (2015).
31. Chen, F. *et al.* The orbital characters of low-energy electronic structure in iron-chalcogenide superconductor $K_xFe_{2-y}Se_2$. *Chin. Sci. Bull.* **57,** 3829–3835 (2012).
32. Hsu, F. C. *et al.* Superconductivity in the PbO-type structure alpha-FeSe. *Proc. Natl Acad. Sci. USA* **105,** 14262–14264 (2008).
33. Urata, T. *et al.* Argument on superconductivity pairing mechanism from cobalt impurity doping in FeSe: spin ($s\pm$) or orbital (s_{++}) fluctuation. Preprint at http://arxiv.org/abs/1508.04605v1 (2015).
34. Abdel-Hafiez, M. *et al.* Superconducting properties of sulfur-doped iron selenide. *Phys. Rev. B* **91,** 165109 (2015).
35. Huang, D. *et al.* Revealing the empty-state electronic structure of single-unit-cell FeSe/$SrTiO_3$. *Phys. Rev. Lett.* **115,** 017002 (2015).
36. Zhang, Y. *et al.* Nodal superconducting-gap structure in ferropnictide superconductor $BaFe_2(As_{0.7}P_{0.3})_2$. *Nat. Phys.* **8,** 371–375 (2012).
37. Niu, X. H. *et al.* Identification of prototypical Brinkman-Rice Mott physics in a class of iron chalcogenides superconductors. Preprint at http://arxiv.org/abs/1506.04018 (2015).
38. Glasbrenner, J. K. *et al.* Effect of magnetic frustration on nematicity and superconductivity in iron chalcogenides. *Nat. Phys.* **11,** 953–958 (2015).
39. Chang, C.-C. *et al.* Superconductivity in PbO-type tetragonal FeSe nanoparticles. *Solid State Commun.* **152,** 649–652 (2012).
40. Medvedev, S. *et al.* Electronic and magnetic phase diagram of beta-$Fe_{1.01}Se$ with superconductivity at 36.7 K under pressure. *Nat. Mater.* **8,** 630–633 (2009).
41. Sun, L. *et al.* Re-emerging superconductivity at 48 kelvin in iron chalcogenides. *Nature* **483,** 67–69 (2012).
42. Ge, J. F. *et al.* Superconductivity above 100 K in single-layer FeSe films on doped $SrTiO_3$. *Nat. Mater.* **14,** 285–289 (2015).
43. de Medici, L. *et al.* Selective Mott physics as a key to iron superconductors. *Phys. Rev. Lett.* **112,** 177001 (2014).
44. Georges, A. *et al.* Strong correlations from Hund's coupling. *Annu. Rev. Condens. Matter Phys.* **4,** 137–178 (2013).
45. Nakajima, M. *et al.* Strong electronic correlations in iron pnictides: comparison of optical spectra for $BaFe_2As_2$-related compounds. *J. Phys. Soc. Jpn* **83,** 104703 (2014).
46. Chen, T. K. *et al.* Fe-vacancy order and superconductivity in tetragonal beta-$Fe_{1-x}Se$. *Proc. Natl Acad. Sci. USA* **111,** 63–68 (2014).
47. Lei, B. *et al.* Gate-tuned superconductor-insulator transition in (Li,Fe)OHFeSe. Preprint at http://arxiv.org/abs/1503.02457v1 (2015).
48. Xu, H. C. *et al.* Direct observation of the bandwidth control mott transition in the nis2-xsex multiband system. *Phys. Rev. Lett.* **112,** 087603 (2014).
49. Imada, M. *et al.* Metal-insulator transitions. *Rev. Mod. Phys.* **70,** 1039 (1998).
50. Hanaguri, T. *et al.* Unconventional s-wave superconductivity in Fe(Se,Te). *Science* **328,** 474–476 (2010).
51. Fang, C. *et al.* Robustness of s-wave pairing in electron-overdoped $A_{1-y}Fe_{2-x}Se_2$ (A = K, Cs). *Phys. Rev. X* **1,** 011009 (2011).
52. Zhou, Y. *et al.* Theory for superconductivity in (Tl,K)Fe_xSe_2 as a doped Mott insulator. *Europhys. Lett.* **95,** 17003 (2011).
53. Yang, F. *et al.* Fermiology, orbital order, orbital fluctuations, and Cooper pairing in iron-based superconductors. *Phys. Rev. B* **88,** 100504 (2013).
54. Maier, T. A. *et al.* d-wave pairing from spin fluctuations in the $K_xFe_{2-y}Se_2$ superconductors. *Phys. Rev. B* **83,** 100515 (2011).
55. Mazin, I. I. *et al.* Symmetry analysis of possible superconducting states in $K_xFe_ySe_2$ superconductors. *Phys. Rev. B* **84,** 024529 (2011).
56. Yin, Z. P. *et al.* Spin dynamics and orbital-antiphase pairing symmetry in iron-based superconductors. *Nat. Phys.* **10,** 845–850 (2014).
57. Hu, J. P. *et al.* Iron-based superconductors as odd-parity superconductors. *Phys. Rev. X* **3,** 031004 (2013).
58. Hirschfeld, P. J. *et al.* Gap symmetry and structure of Fe-based superconductors. *Rep. Prog. Phys.* **74,** 124508 (2011).
59. Fan, Q. *et al.* Plain s-wave superconductivity in single-layer FeSe on $SrTiO_3$ probed by scanning tunneling microscopy. *Nat. Phys.* **11,** 946–952 (2015).
60. Chareev, D. *et al.* Single crystal growth and characterization of tetragonal $FeSe_{1-x}$ superconductors. *Cryst.Eng.Comm.* **15,** 1989–1993 (2013).

Acknowledgements

We gratefully acknowledge Professor J.P. Hu, Professor D.H. Lee and Dr Darren Peets for helpful discussions. This work is supported in part by the National Science Foundation of China and the National Basic Research Program of China (973 Program) under the grant No. 2012CB921402, and Science and Technology Commission of Shanghai Municipality under the grant No. 15ZR1402900. M.A. acknowledges funding by DFG in the project MO 3014/1-1.

Author contributions

C.H.P.W. and C.C. grew the films, M.A., D.A.C. and A.N.V. grew the single crystals. C.H.P.W., H.C.X., C.C., and R.P. performed ARPES measurements. C.H.P.W., R.P. and D.L.F. Analysed the ARPES data. R.P., H.C.X. and D.L.F. wrote the paper. R.P. and D.L.F. are responsible for the infrastructure, project direction and planning. All authors have discussed the results and the interpretation.

Additional information

Supplementary Information accompanies this paper at http://www.nature.com/naturecommunications

Competing financial interests: The authors declare no competing financial interests.

Reprints and permission information is available online at http://npg.nature.com/reprintsandpermissions/

How to cite this article: Wen, C. H. P. *et al.* Anomalous correlation effects and unique phase diagram of electron-doped FeSe revealed by photoemission spectroscopy. *Nat. Commun.* 7:10840 doi: 10.1038/ncomms10840 (2016).

This work is licensed under a Creative Commons Attribution 4.0 International License. The images or other third party material in this article are included in the article's Creative Commons license, unless indicated otherwise in the credit line; if the material is not included under the Creative Commons license, users will need to obtain permission from the license holder to reproduce the material. To view a copy of this license, visit http://creativecommons.org/licenses/by/4.0/